UNCLASSIFIED

AD NUMBER

AD525354

CLASSIFICATION CHANGES

TO: unclassified

FROM: confidential

LIMITATION CHANGES

TO:

Approved for public release, distribution
unlimited

FROM:

Distribution controlled. All requests to:
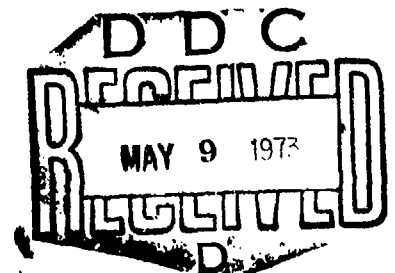Office of Naval Research, Code 421,
Arlington, VA

AUTHORITY

OCA; 31 Dec 1981 IAW document markings;
ONR ltr dtd 7 Oct 1998

THIS PAGE IS UNCLASSIFIED

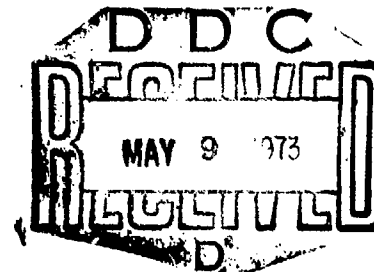SECRET

DDC

MAY 9 1973

RECEIVED

DDC CONTROL
NO. 31007

NORTHROP

Research and Technology Center

SECRET

SECRET

SEMIANNUAL TECHNICAL REPORT
HIGH POWER CO LASER (U)

March 1973

NATIONAL SECURITY INFORMATION
UNAUTHORIZED DISCLOSURE SUBJECT
TO CRIMINAL SANCTIONS

DDC
RECEIVED
MAY 9 1973

Prepared by

Northrop Research and Technology Center
Laser Technology Laboratories

Contract N00014-72-C-0043

Sponsored by
ADVANCED RESEARCH PROJECTS AGENCY
ARPA ORDER NO. 1807

Monitored by
OFFICE OF NAVAL RESEARCH
CODE 421
ARLINGTON, VA. 22217
N00014-72-C-0043

CLASSIFIED BY DD-254 Nov 72
SUBJECT TO GENERAL DECLASSIFICATION
SCHEDULE OF EXECUTIVE ORDER 11652
AUTOMATICALLY DOWNGRADED AT TWO YEAR
INTERVALS
DECLASSIFIED ON DECEMBER 31, 1981

NORTHROP CORPORATION
Northrop Research and Technology Center
Laser Technology Laboratories
3401 West Broadway
Hawthorne, California 90250

DDC CONTROL
NO. 31007

CNP-2643
Copy 93

SECRET

UNCLASSIFIED

PROGRAM IDENTIFICATION (U)

ARPA Order No.:	1807
Program Code No.:	3E90
Name of Contractor:	Northrop Corporation
Effective Date of Contract:	1 August 1971 - 31 July 1973
Amount of Contract:	$ 2, 825, 833. 00
Contract No.:	N00014-72- C-0043
Program Manager:	Dr. G. Hasserjian (213) 675-4611, Ext. 4861
Project Scientist:	Dr. M. M. Mann (213) 675-4611, Ext. 2821
Scientific Officer:	Director, Physics Program Physical Sciences Division Office of Naval Research Department of Navy 800 North Quincy Arlington, Virginia 22217

UNCLASSIFIED

UNCLASSIFIED

SEMIANNUAL TECHNICAL REPORT
HIGH POWER CO LASER (U)

TABLE OF CONTENTS (U)

UNCLASSIFIED

1.0 SUMMARY

(S) The purpose of this program is to develop, on an approximately 2-3 year time scale, a 1 - 2 MW average power, repetitively pulsed diffraction-limited CO laser operating at an electrical efficiency of 50% or more. The work covered in this contract involves the design of intermediate power CO laser devices, the development of the required CO laser technology, and the construction of an intermediate power CO laser device.

(U) This program encompasses, on a best effort basis, the following major tasks:

(U) 1. The development of both steady state and transient kinetic models in order that realistic theoretical predictions of high energy device characteristics can be made.

(U) 2. Measurements of basic parameters of the CO laser at low pressures including: gain, saturation intensity, rates of vibrational cross-relaxation between CO molecules, transfer rates of CO and N_2, discharge characteristics, and spectral characteristics.

(U) 3. Measurements and characterization of a high pressure E-beam excited pulsed laser to experimentally determine transient operating parameters for high energy extraction.

(U) 4. The design and construction of a 500 J/pulse diffraction-limited CO laser oscillator.

(U) 6. The development of line selection techniques for controlling the oscillator spectral output.

(U)   Improvements have been made in the three-laser experimental techniques during this quarter, and comparisons of the data obtained from observation of transient gain relaxation have supported the Jeffers-Kelley (JK) VV rate theory used in the present kinetic model. Furthermore, comparisons of our analysis with raw experimental data reported by Wittig and Smith (WS) for gain relaxation in a pulsed system show that the JK VV rates can give good agreement, and suggests that the WS interpretation of the observed time constants as rates for $(v, 0 \rightarrow v-1, 1)$ collisions may be incorrect. A variety of data is presented and discussed in Section 2.0.

(U)   Several modifications have been made in the design of the gas flow system that have resulted in significant improvements in medium homogeneity. Optical interferometric studies have also been carried out, and results are given in Section 3.0.

(U)   Work related to line selection has consisted of low pressure measurements in a longitudinal discharge laser, as well as high pressure experiments on the E-beam device. Furthermore, work has continued on attempts to obtain reliable experimental data and a theoretical model for atmospheric transmission. Measurements of absorption versus water vapor pressure have been continued, but are limited to CO spectral lines with high loss due to the short path lengths involved in the experimental setup. Results of our data have been compared (for one CO line) with recent work of Long, and there still remains a discrepancy in the experimental values. Furthermore, additional improvements in the theoretical model for water vapor absorption are necessary to give agreement with experiments. Uncertainties about line shape, as well as the functional dependence of line "width" on temperature and gas constituents, have not yet been adequately resolved. The line selection and water vapor absorption data are discussed in Section 4.0.

(U)   In Section 5.0, the parametric dependence of thermal blooming and the effects of atmospheric turbulence are discussed. Sample calculations are presented which indicate that at shorter wavelengths, less laser power is required to obtain a given target intensity.

(U)   Theoretical studies have been undertaken using the Prony method to investigate the effects of radial phase or reflectivity variations on the modes of an unstable resonator. These calculations have shown, as theory predicts, that tapering the reflectivity at the edges of mirrors can have desirable effects on the resulting modes, due to the elimination of diffracted waves from the edges. This technique can reduce extreme intensity variations that would cause undesirable mirror loading, and can give smoother phase variations that would produce narrower beam divergence. Furthermore, mode discrimination is improved, which is desirable for attaining single mode operation. These results are discussed in Section 6.0.

(U)   The E-gun development effort and test results of the area cathode E-gun are reported in Section 7.0.

2.0   V-V RATE MEASUREMENTS

(U)   It was reported in the third quarterly report that kinetic modeling using the same V-V rate matrix did not fit accurately both the transient and the steady state gain measurements. In order to resolve the inconsistency, several improvements in the experimental methods were carried out. First, a more accurate method was employed to measure the CO partial pressures. This gave a much better agreement with transient gain relaxation data which was reported in the fourth quarterly report. The discrepancy observed in steady state data is believed to originate from variations in optical broadening cross sections in the higher v levels.

(U)   Further improvements in the transient gain measurements were carried out in the last quarter. Previously, a preamplifier bandwidth of 1 kHz was used because of excessive noise in the system. But the low bandwidth distorted the shape of the transient gain curve. Such a distortion is not desirable for the simple reason that the validity of the V-V rate matrix is determined by comparing the shapes of the experimental curve with those predicted by the modeling, rather than by measuring individual rates; this procedure is necessary since all the CO vibrational levels are coupled together with widely varying populations and probability of interaction.

(U)   Therefore, for the experiments reported here, a much larger preamplifier bandwidth of 300 kHz was used. Measurement of the transient gain with this wide bandwidth was possible only after several improvements were made in the optical and mechanical systems to eliminate the sources of noise.

(U)   The transient gain variation of the 9-8 P(10) CO laser line was then measured for three different CO partial pressures in the presence of a

4

saturating pulse in the 8-7 P(10) line. The results are presented in Figures 2.1, 2.2 and 2.3. The data points, with circles shown on the experimental curves, are obtained by theoretical modeling using the same rate matrix. The excellent agreement between the theoretical model and experimental data is evident from these figures.

(U) Recently Wittig and Smith reported that the V-V rates at low temperatures may actually be an order of magnitude higher than predicted by the Jeffers and Kelley theory. In order to verify their contention, kinetic modeling was done with ten times higher V-V rates. The results shown in curve b in Figure 2.4 indicate that the higher V-V rates could not be fitted to the experimentally observed curve. For that matter, a ten times smaller V-V rate could not be fitted either, as shown by curve c in Figure 2.4. Therefore, the Jeffers and Kelley rate matrix which is being used in our modeling still gives the most satisfactory agreement.

(U) We believe that although the experimental data of Wittig and Smith are correct, their explanation of the data is inaccurate. Their prediction of higher V-V rates is a result of the incorrect assumption that the populations of the higher v levels are insignificant, so that the relaxation of the levels is affected only by collisions with $v = 0$.

(U) In our experiments, we first mapped out the vibrational populations by small signal gain measurements and used these populations for modeling. Following this procedure we obtained an excellent agreement between the theory and experiment. But if we neglect the population of the higher v levels in our analysis and interpret the observed time constant of relaxation as the collision rate with $v = 0$, we also get a VV rate ten times higher, as did Wittig and Smith. This is most likely not a coincidence. From the vibrational temperatures reported by Wittig and Smith, it is evident that they do indeed have a significant population at the higher v levels.
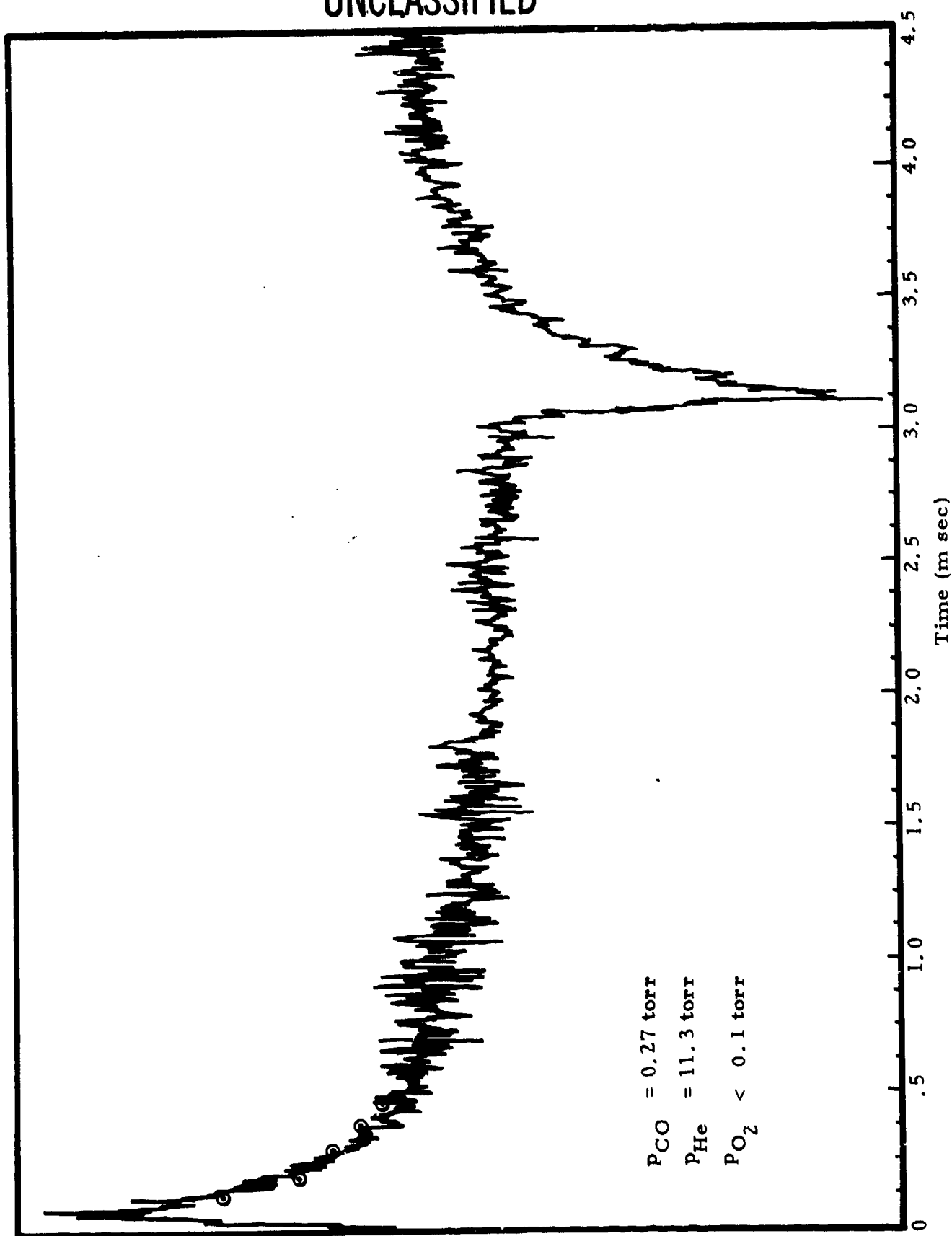
5
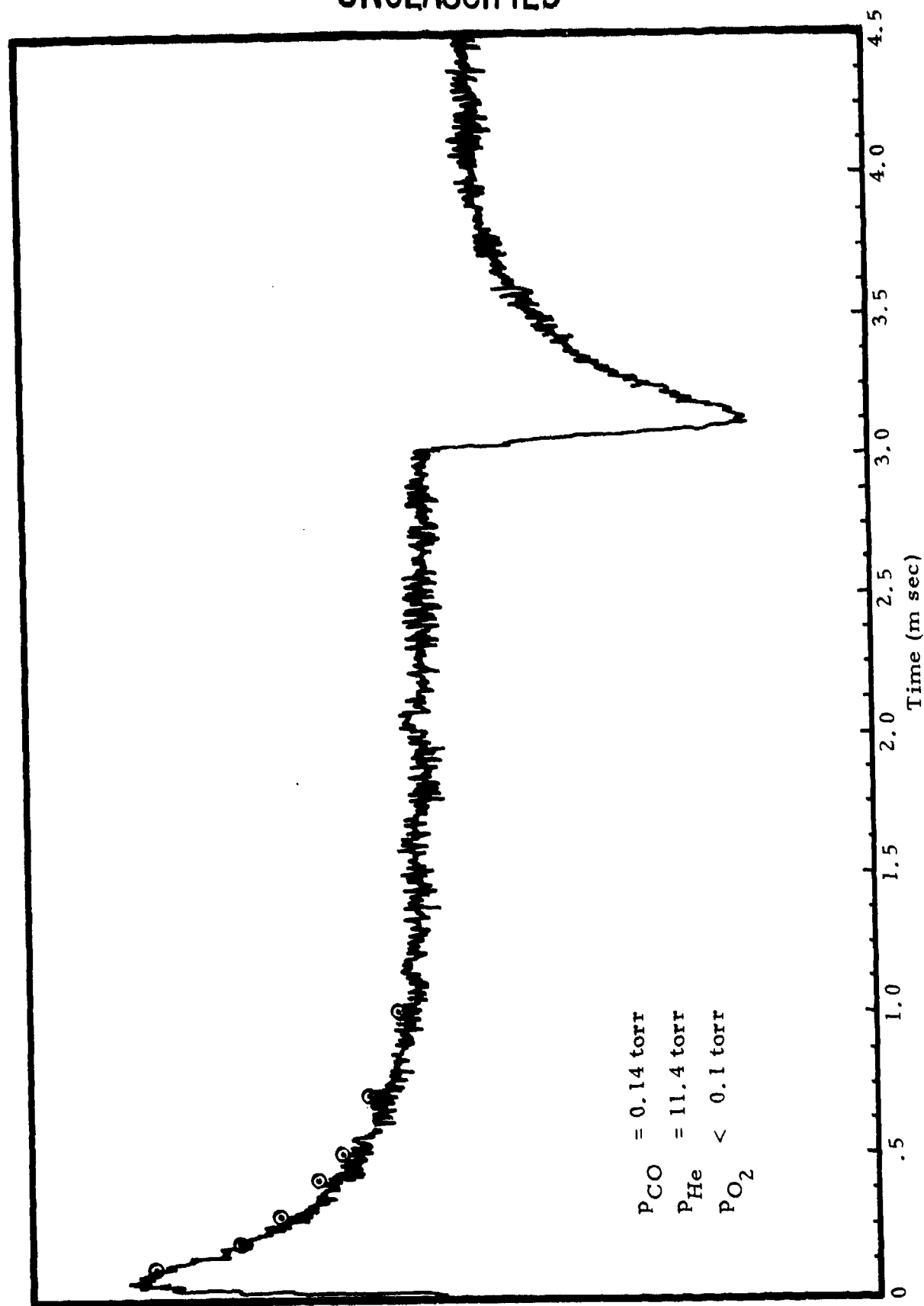
(U) Figure 2.1 Transient Gain Variation of 9-8 P(10) CO Line in Presence of a Saturating Pulse in 8-7 P(10) Line. The Circled Data Points are the Results of Kinetic Modeling. (U)

P_{CO} = 0.14 torr

P_{He} = 11.4 torr

P_{O_2} < 0.1 torr

Time (m sec)

6

(U) Figure 2.2 Transient Gain Variation of 9-8 P(10) CC Line in Presence of a Saturative Pulse in 8-8 P(10) Line. The Circled Data Points are the Results of Kinetic Modeling. (U)
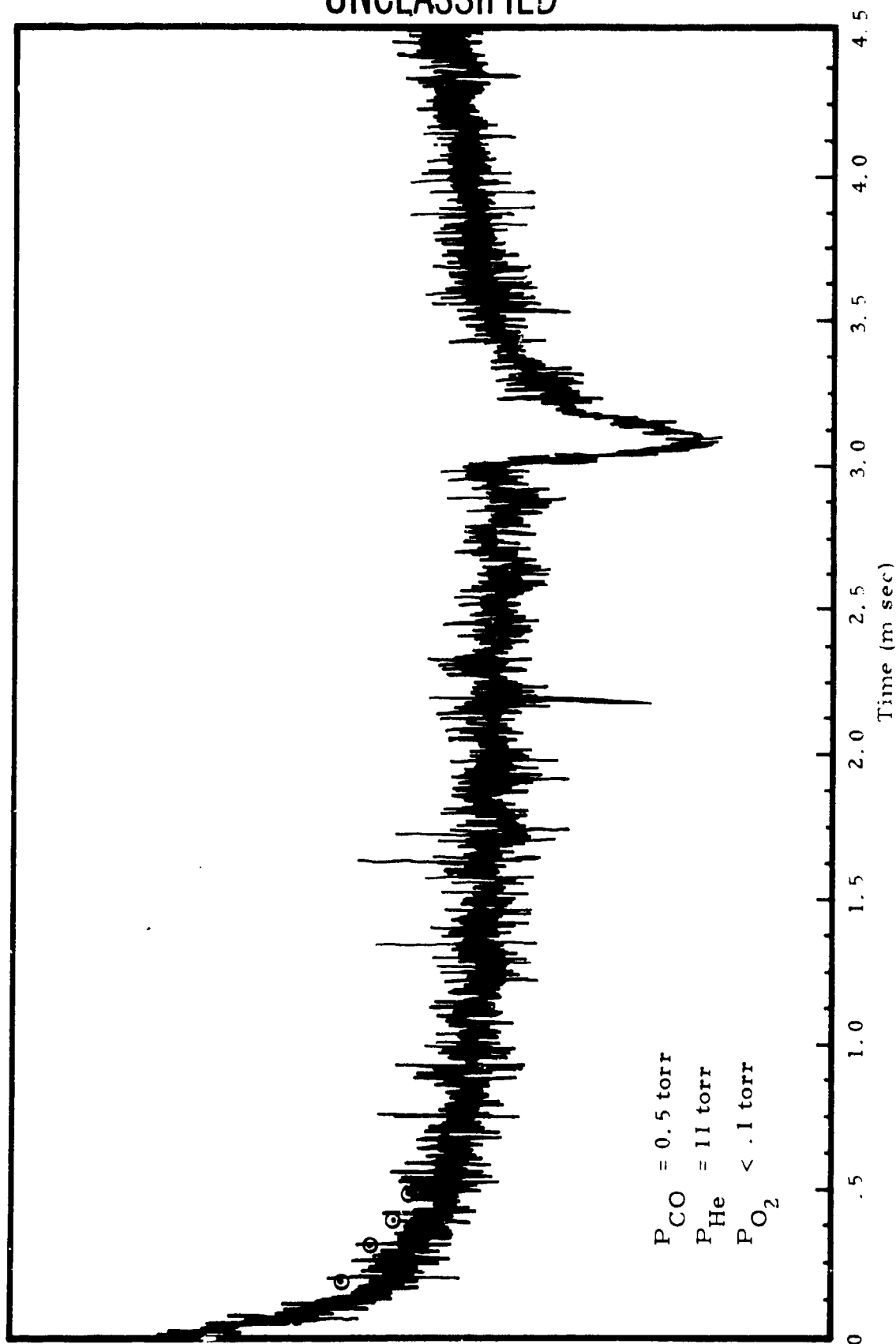
P_{CO} = 0.27 torr

P_{He} = 11.3 torr

P_{O_2} < 0.1 torr

Time (m sec)

P_{CO} = 0.5 torr

P_{He} = 11 torr

P_{O_2} < .1 torr
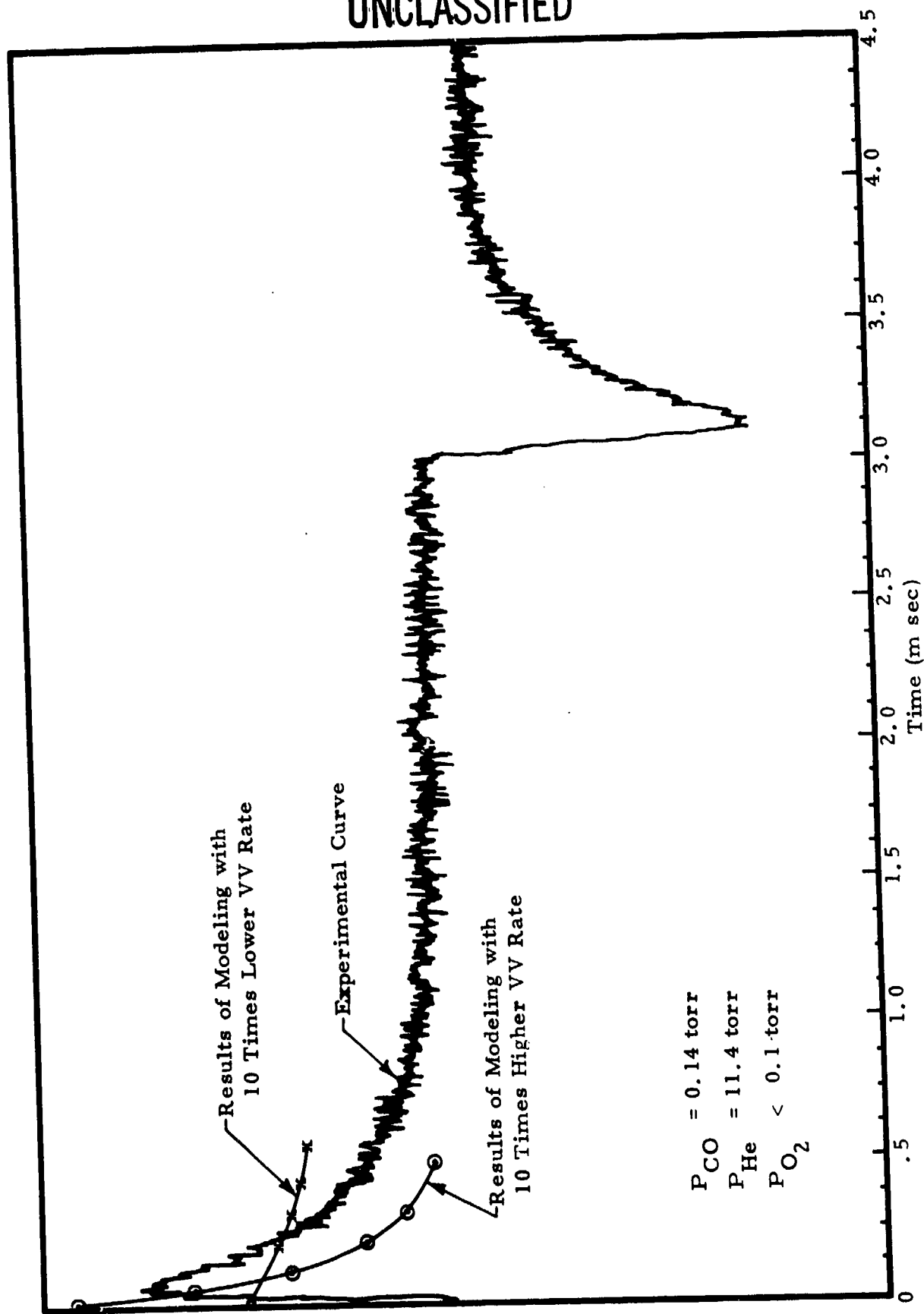
(U) Figure 2-3 Transient Gain Variation of 9-8 P(10) CO Line in Presence of a Saturating Pulse in 8-7 P(10) Line. The Circled Data Points are the Results of Kinetic Modeling. (U)

8

(U) Figure 2. 4 Transient Gain Variation of 9–8 P(10) CO Line in Presence of a Saturating Pulse in 8–7 P(10) Line (U)

P_{CO} = 0.14 torr
P_{He} = 11.4 torr
P_{O_2} < 0.1 torr

Results of Modeling with 10 Times Lower VV Rate

Experimental Curve

Results of Modeling with 10 Times Higher VV Rate

Time (m sec)

9

(U)   In order to lend further support to our contention, we carried out kinetic modeling for the experimental conditions reported by Wittig and Smith. It was not surprising that we were able to fit their transient gain data quite accurately to the Jeffers and Kelley matrix; these results are shown in Figure 2.5. Therefore, the Jeffers and Kelley VV rate matrix, which we have used to explain a variety of experimental data satisfactorily, still gives the best available rates.
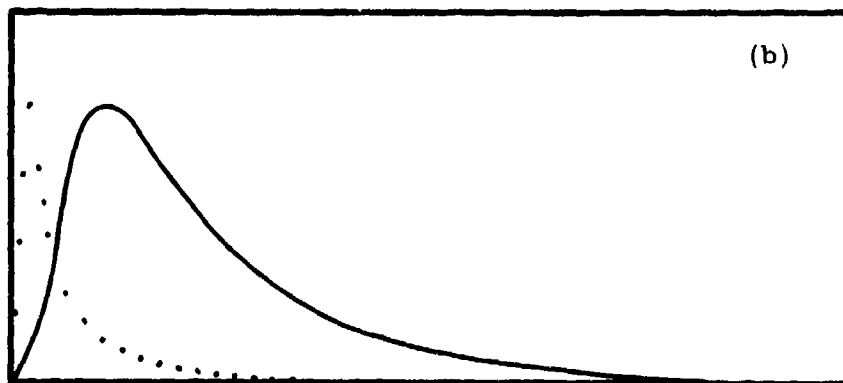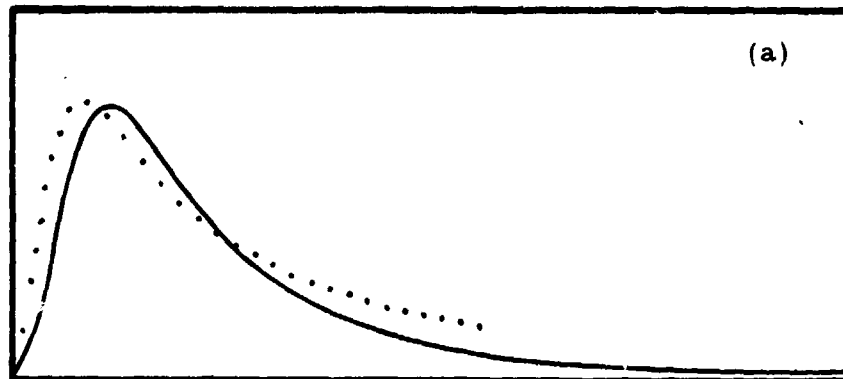
(U) Figure 2.5 Solid curves show experimental data of Wittig and Smith for gain relaxation of $6 \rightarrow 5$ P(8) line. Dotted curves correspond to kinetic model simulation with ~40 mJ input using (a) JK theory, and (b) ten times JK theory. (U)

3.0   LASER PLENUM MEDIUM QUALITY CONTROL

(U)   The CO laser has an inherently difficult medium homogeneity problem due to the high density of the lasing gas before discharge. This high density results from the requirement that the gas be close to liquid nitrogen temperature and from the fact that argon is commonly used as the major diluent. The LN_2 temperature requirement makes the gas approximately 3.5 times more dense than it would be at room temperature. Use of argon as a diluent instead of He or N_2, further increases the medium density. Therefore, to restrict the variations in refractive index to acceptable amounts, very small percentage changes in gas temperature or pressure can be tolerated.

(U)   The cryogenic temperature of the lasing mixture causes a further problem in that a large temperature difference exists between the gas and most of the other components of the laser system. Thus, heat leaks into the gas cause variations in gas temperature and corresponding changes in medium refractive index.

(U)   An indication of the magnitude of the problem is shown in Figure 3.1. A one meter cavity filled with nitrogen at atmospheric pressure and $77.4^{\circ}K$ is assumed. Small temperature variations are assumed to exist in the cavity. These temperature variations cause the cavity to look like either: (a) an optical wedge; (b) a plano-convex lens; or (c) a grating. The magnitude of the temperature variations which will cause $\lambda/20$ wavefront distortion are listed at the right hand side of the figure. As can be seen, depending on the type of nonuniformity, total temperature variation of only ~ 0.01 to $0.02^{\circ}K$ can be allowed for $\lambda/20$ performance at these cavity conditions.
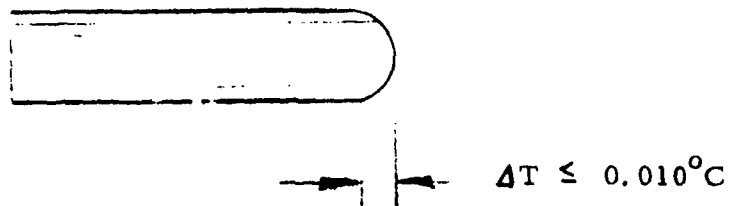
3.1   (U) <u>Sources of Passive Medium Inhomogeneities</u>.   Because of the practical problems of maintaining both the lasing cavity and the E-gun
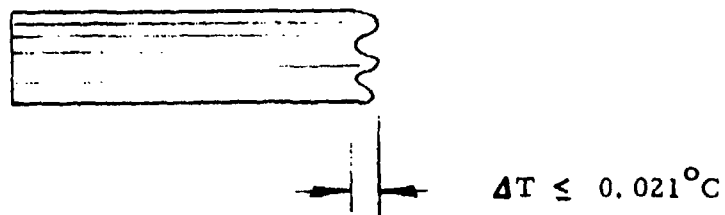
● WEDGE DISTORTION

$\Delta T \leq 0.017^{\circ}C$
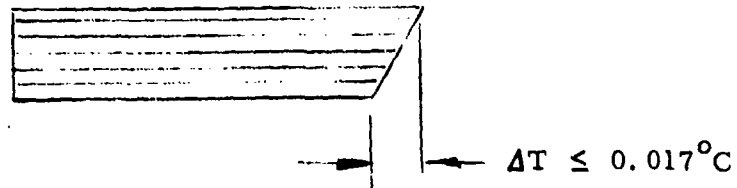
● CONVEX DISTORTION

$\Delta T \leq 0.010^{\circ}C$

● RANDOM DISTORTION

$\Delta T \leq 0.021^{\circ}C$

(U) Figure 3.1   Allowable Temperature Errors in a One Meter
Cavity for $\lambda/20$ Wave Front Distortion. GN_2
at $77.4^{\circ}K$ and One Atmosphere Pressure. (U)

foil/cathode combination at liquid nitrogen temperatures within the required accuracies indicated in Figure 3. 1, a flowing rather than a static cavity was used. Flow velocities were kept high enough to either remove or reduce unwanted thermal boundary layers. The particular scheme chosen used a porous anode, with gas flow toward the cathode. Figure 3.2 shows the flow concept and the various anticipated sources of temperature errors associated with it.

(U)   Operation of the cavity is as follows: Precooled laser gas is brought into the anode. Inside the anode there is a small, boiler type heat exchanger which provides final thermal conditioning of the lasing gas. After exiting the internal heat exchanger in the anode, the lasing gas flows out through a porous screen in the top surface of the anode. The gas flows upward between dielectric sidewalls toward the E-gun, and, after passing through the cathode screen, it impacts on the E-gun foil and flows sideways to a suction manifold. Velocities are kept sufficiently low that dynamic pressure causes a negligible effect on fluid density. Medium density changes are caused solely by temperature errors and by improper mixing of constituent laser gases (for example, argon and CO).

(U)   Major sources of temperature errors in the cavity are: (a) thermal boundary layers on the sidewalls; (b) a thermal boundary layer on the cathode screen; (c) a thermal boundary layer on the E-gun foil and foil mount; (d) a thermal boundary layer on the cavity window; and (e) temperature variations in the gas as it exits the anode screen.

(U)   The thermal boundary layer on the cathode screen was analyzed as if the cathode were a porous wall with suction. Cathode temperature
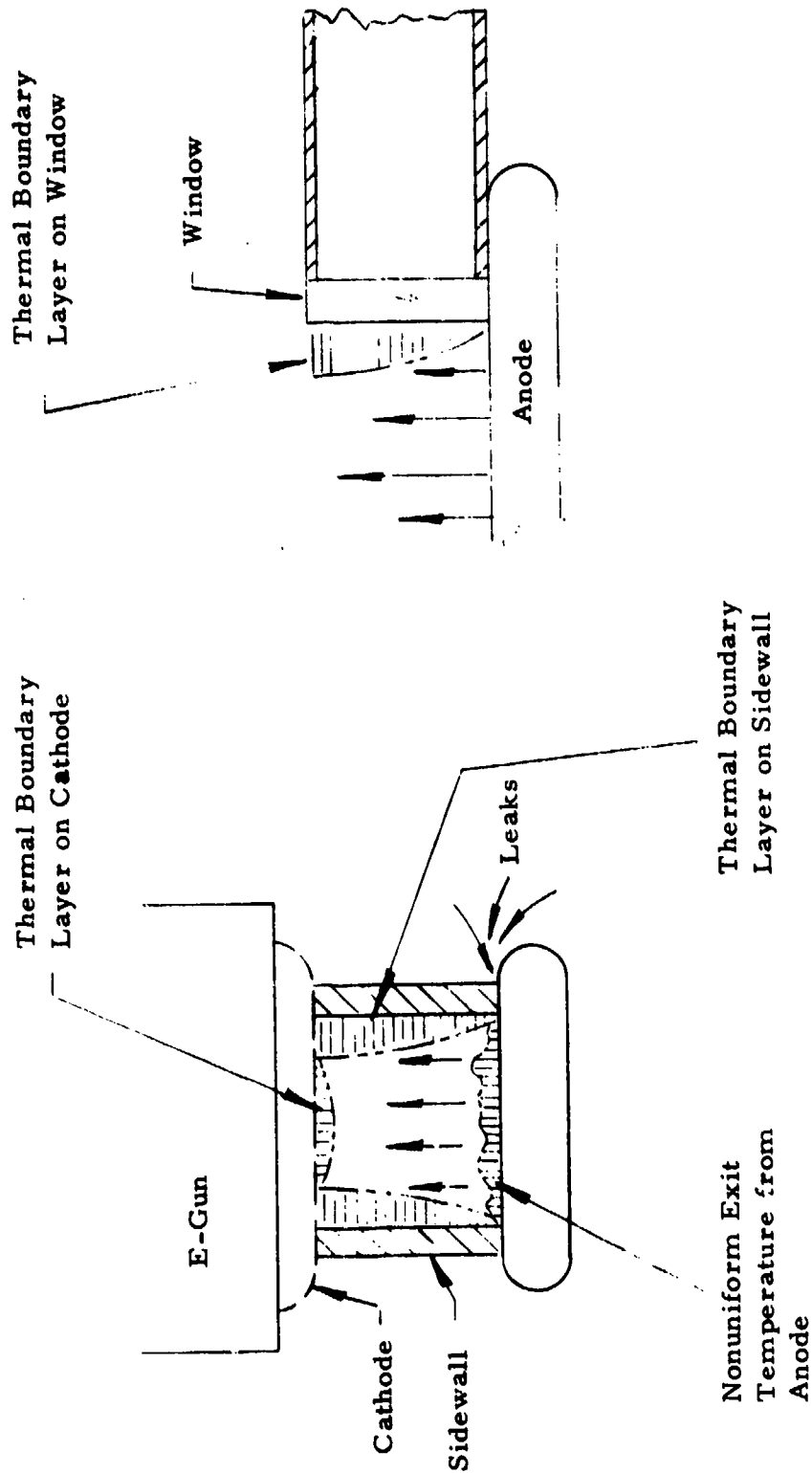
(U) Figure 3.2 Sources of Tempered Nonuniformities in a Flowing Laser Cavity. Flow Parallel to E-Beam. (U)

15

was assumed to be 300°K. Variation of gas density and gas thermal conductivity as a function of temperature was taken into account. Results indicated that a gas velocity of only ~0.8 cm/sec would reduce the temperature rise to within 0.01°C at approximately 0.2 cm distance from the cathode. The primary requirement on cavity velocity was the minimization of thermal boundary layers on the side walls and windows.

(U) Capabilities of the existing flow system and a desire to conserve laser gas dictated a maximum laser gas consumption of about 12 gm/sec. For pure nitrogen at atmospheric pressure and 77.4°K, this results in a gas velocity on the order of 5.4 cm/sec. At this gas velocity, uncooled walls at 300°K will cause an unacceptably large and hot boundary layer. Medium inhomogeneity and a tendency for arc breakdown of the laser gas result. Two methods were tried in an attempt to reduce both the thickness and the temperatures of this boundary layer. The first consisted of cooling the sidewalls directly by a liquid nitrogen bath and the windows indirectly by conduction to the adjacent sidewalls. Unfortunately, malfunctioning of a cryogenic valve severely damaged the side-walls so that they were no longer liquid tight.

(U) The second approach for reduction of the sidewall thermal boundary layer consisted of thermal isolation of the part of the sidewall in contact with the laser gas. A small amount of laser gas was allowed to flow up the back side of the sidewall to further enhance its thermal isolation. The windows were thermally isolated by a vacuum support tube. The concept is shown in Figure 3.3. This approach requires the gas to flow for a period of time before lasing experiments so that the sidewalls have a chance to cool to approximately gas temperature.

16
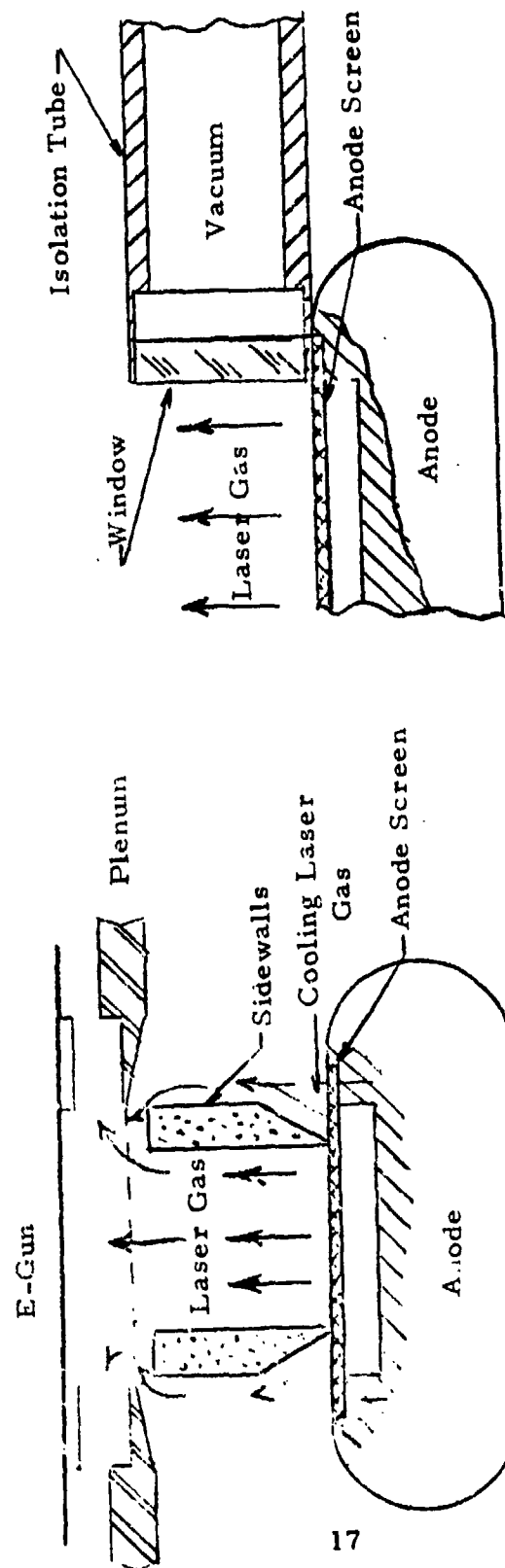
b. Vacuum (Thermal) Isolation of Cavity Windows

a. Thermal Isolation of Sidewalls

(U) Figure 3.3   Illustration of Sidewall and Window Thermal Isolation Techniques. (U)

17

3.2 (U) <u>Experimental Medium Homogeneity Improvement.</u> As a result of severe medium inhomogeneities observed in earlier testing, a systematic program was initiated to investigate and eliminate their sources. A combination of approaches was used in the diagnosis including analysis of temperature errors, flow visualization, and optical probes. Flow visualization included both steam injection into the cryogenic laser gas, and smoke injection into room temperature air which was used in place of the cryogenic laser gas. Optical probing included both an unexpanded He-Ne beam projected along the cavity's optical axis in a shadowgraph mode and a He-Ne Schlieren setup.

(U) The initial character of the medium was extreme optical turbulence. Room temperature flow visualization of the medium indicated major leaks between the anode and the LN_2 cooled sidewall and between the anode screen and the anode proper. After these leaks were corrected, flow visualization revealed that the flow was not exiting normal to the anode screen. The actual angle of exit was closer to 80-85 degrees from the normal. The combination of leaks between the anode and its porous screen and this large departure angle cav ed a combination of vertical spouts accompanied by sidewall return currents (Figure 3.4-a) and a longitudinal vortex (Figure 3.4-b). Much of the gas sent towards the E-gun foil was returned to the cavity with a temperature closer to $300^{\circ}K$ than the desired $77.4\,^{\circ}K$. Temperature fluctuations were severe.

(U) The leaks between the anode, its screen, and the sidewall structure were eliminated by careful attention to assembly and sealing of the components. The source of the large flow angle appeared to result from the construction of the sintered anode screen. The screen consisted of two layers of stainless steel, dutch weave screen wire. The two layers had been sintered together at right angles to form a reasonably rigid

18
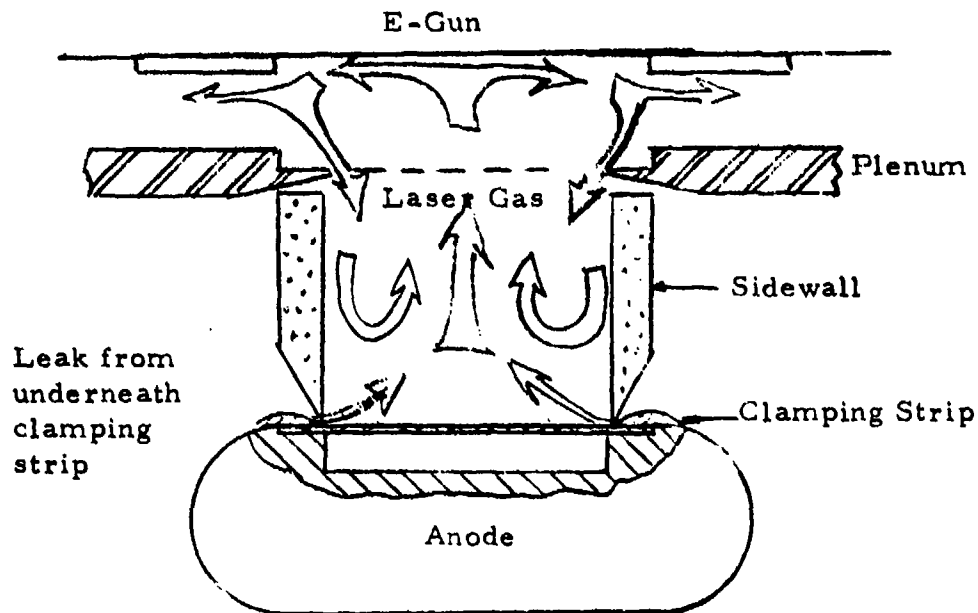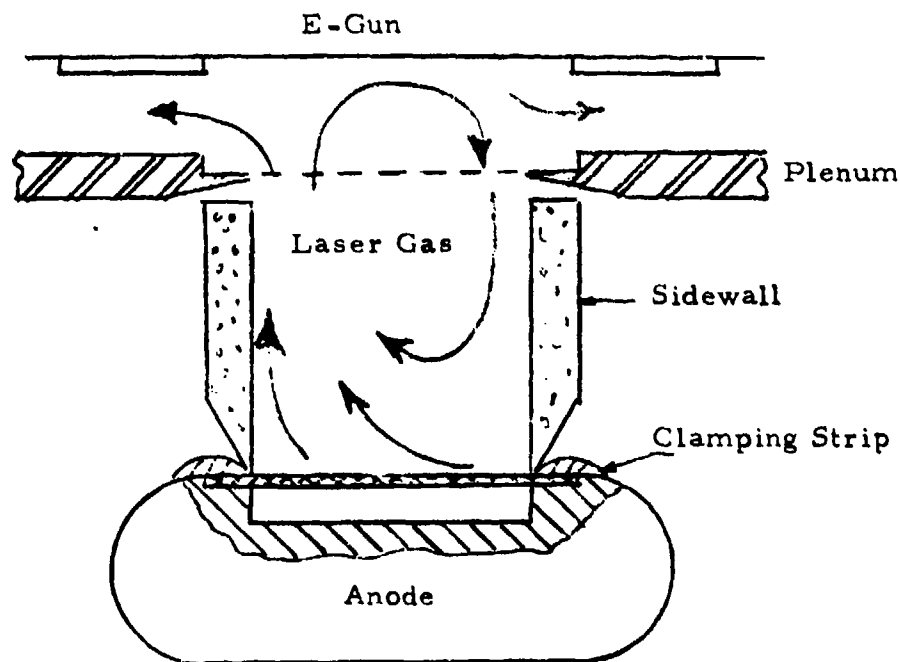
a. Leaks

b. Large Departure Angle

(U) Figure 3.4 Illustration of Flow Anomalies Caused by Leaks
Under Anode Screen Clamping Strip and by a
Large Flow Departure Angle from the Anode Screen.(U)

19

structure. The original permeability of this sintered assembly had been too high and the manufacturer had reduced it by passing the screen wire through large calendering rolls. The calendering operation pushes the fine warp wires sideways on the heavier shute wires. The net result, over a large area of screen wire, is to effectively form a large bank of sideward pointing nozzles. The aiming is strong and the flow, as mentioned previously, exits at an angle of ~80-85 degrees from the normal. This behavior is apparently a characteristic of sintered, calendered screen wire since several samples were purchased, both of varying permeability and of varying material (stainless and aluminum) and the same result was noted.

(U)   Square mesh screen wire did not exhibit this behavior due to the higher degree of interlocking between warp and shute wires, the fact that both warp and shute wires are identical, and the two dimensional isotropic nature of the weave. Unfortunately, it cannot be uniformly calendered down to the low permeability required by the laser anode.

(U)   The approach taken was to add four layers of 50 mesh screen wire on top of the sintered screen wire and to hold the 50 mesh wire in place with a final piece of 20 mesh wire. The arrangement is shown schematically in Figure 3. 5. When all secondary leaks associated with the clamping strips had been eliminated, the flow exiting the anode was 100% laminar, exited within one or two degrees of normal, and was attached, with laminar boundary layers, to both sidewalls and to both windows.

(U)   A second source of optical scintillation was noted. This source was a fine aerosol cloud in the cavity. The aerosol cloud apparently resulted from local condensation of the nitrogen gas as it flowed through the anode screen. Since the screen was maintained close to LN_2
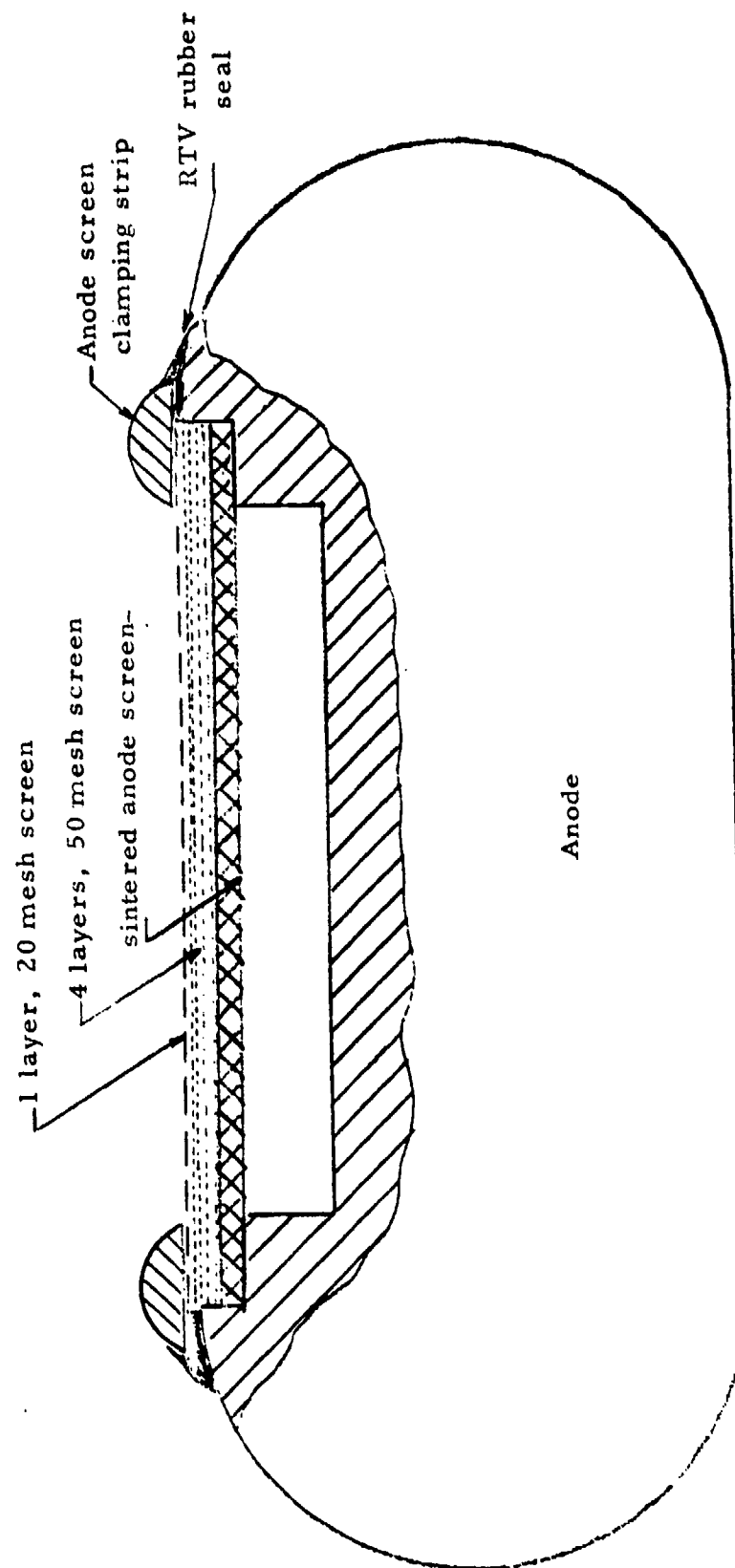
(U) Figure 3.5 Illustration of Flow Straightening Modification to Anode. (U)

21

temperature by conduction, and since it had a finite pressure drop, such condensation was reasonable to expect. The problem was eliminated by raising the vent pressure of the anode heat exchanger.

(U)   Following correction of these flow anomolies, a final series of experiments were conducted on the laser cavity using cryogenic gaseous nitrogen and argon. These gases effectively represented the CO-A mix used in actual laser shots. Medium quality using GN_2 was quite good at atmospheric pressure and flow rate of 12 gm/sec. At lower cavity pressures, best medium quality was obtained at lower flow rates. Apparently, heat transfer between the anode screen and the laser gas was not sufficient at the higher flow rates to effect the required final thermal smoothing. Best overall results were obtained at cavity pressures ranging from 150 to 250 torr with a gas flow rate of ~4 gm/sec. No streamers, boundary layers, or optical scintillation could be observed with either a shadowgraph or Schlieren probe of the medium. Measured gas temperature during all tests was ~91 $^{\circ}$K. Actual gas temperature was probably less due to thermal conduction along the thermocouple wires heating the junction above gas temperature.

(U)   Argon was also used with similar results. When a mixture of argon and nitrogen was used, however, appreciable optical scintillation was noted. This scintillation was ascribed to imperfect mixing of the two gases. Corrective action consisted of modifying the vortex mixer with a series of packed bead beds. Following this modification, tests showed no scintillation when both gases were run.

3.3   (U) Optical Investigations. With the completion of the design modification of the flow scheme for the laser plenum discussed in the previous

section, an experimental determination of the optical quality of the medium utilizing this scheme was undertaken. The interferometric setup used for this investigation is shown in Figure 3.6; it is basically a Michelson type interferometer with the flow region included in one leg. Figure 3.7 shows a cross-sectional view of the device including the region covered by the interferometer beam.

(U)   Figure 3.8 illustrates the basic interferogram of the system. This figure represents a plenum pressure of 506 torr at ambient temperature; and low rate of flow (0.8g/sec). The interferogram is literally unchanged when the gas flow is eliminated and the plenum is either evacuated or at ambient pressure.

(U)   Figure 3.9 illustrates an interferogram for flowing nitrogen at cryogenic temperature. The vertical fringes are due to Fresnel edge diffraction. As the laser is cooled to cryogenic temperatures, thermal contraction causes the Microy fences shown in Figure 3.7 to move toward the optical axis of the system. The interferometer beam passing through the laser plenum is thus vignetted and a diffraction pattern is formed. Since the Microy fences are not directly cooled they are warmer than the flowing cryogenic gas. The refractive index change caused by the thermal gradient from the warm fence to the cold gas results in a cylindrical lens effect giving focusing in the horizontal plane. This focusing which occurs during the two passes through the medium causes the narrowing of the pattern visible in the figure. The horizontal fringes of the interferogram indicate the optical quality of the flowing gas. The uniformity of these fringes verifies the lack of turbulence and inhomogeneities in the gas. The superb optical quality exhibited by the interferogram using 6328Å radiation would be even better at the operating laser wavelength of 5μm.
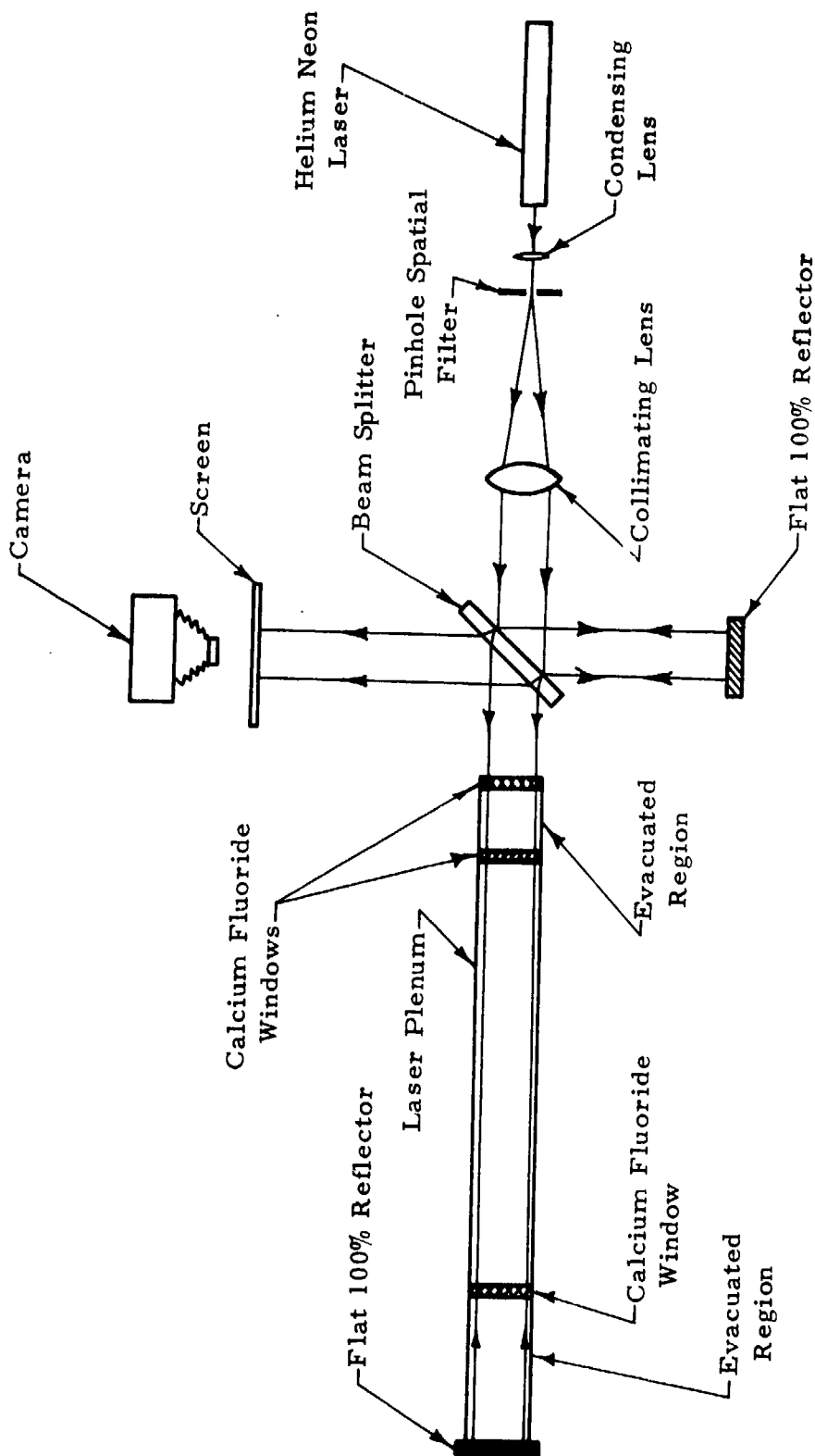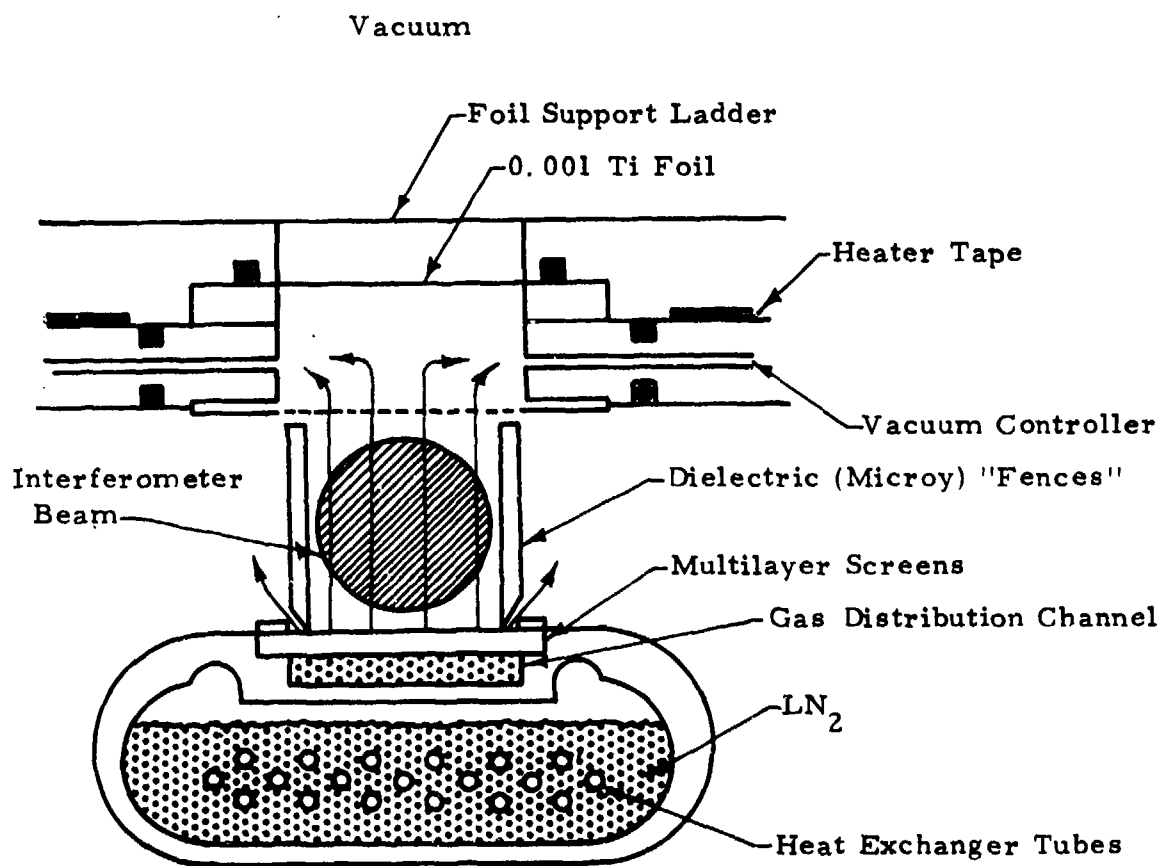
(U) Figure 3.6 Interferometric Setup for Determination of the Optical Quality of a Flowing Cryogenic Carbon Monoxide Laser (U)
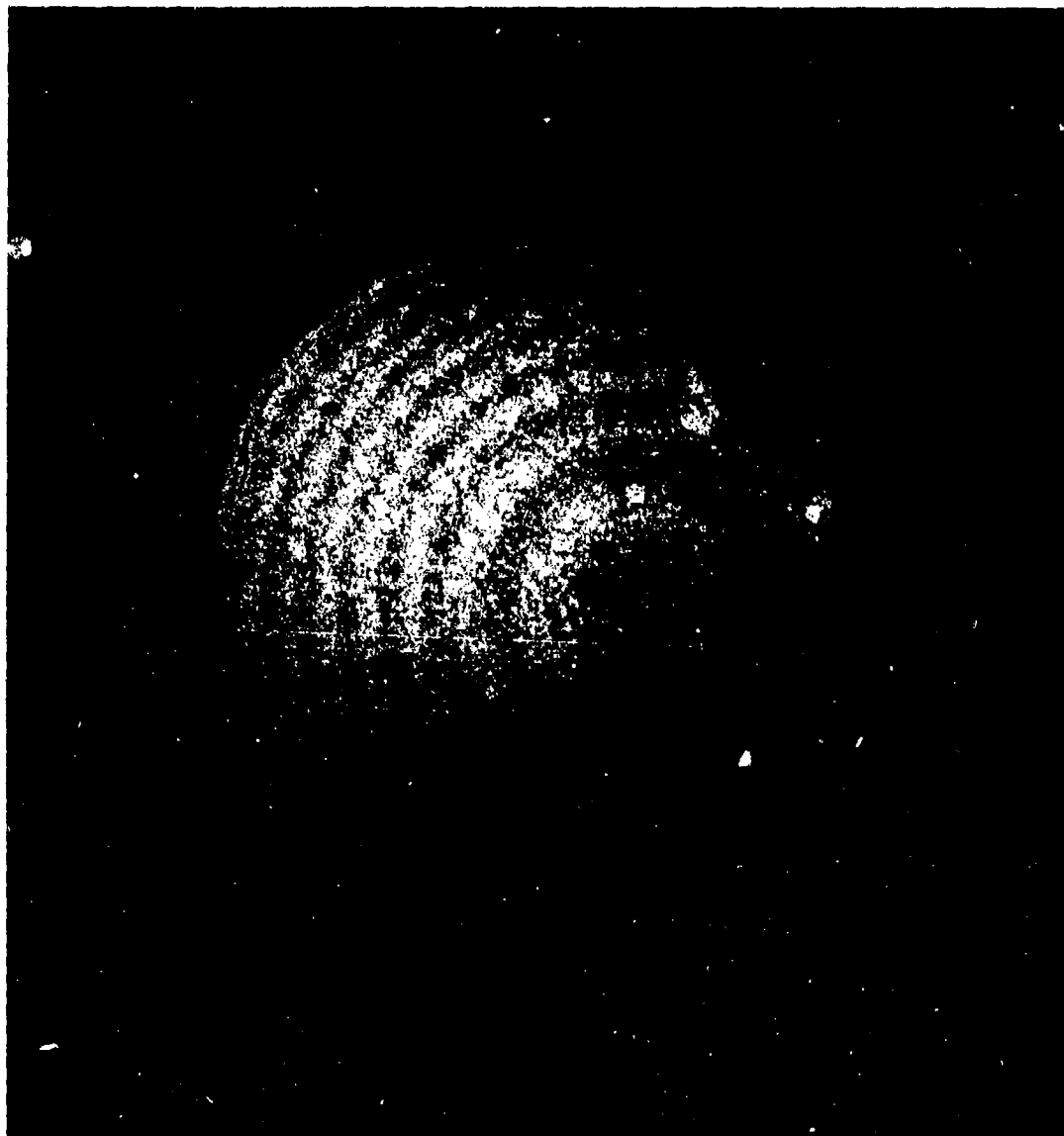
Vacuum

Foil Support Ladder

0.001 Ti Foil

Heater Tape

Vacuum Controller

Interferometer
Beam

Dielectric (Microy) "Fences"

Multilayer Screens

Gas Distribution Channel

LN$_2$

Heat Exchanger Tubes

(U) Figure 3.7 Schematic Cross Section of No. 1 Device (U)

25

(U) Figure 3.8   Interferogram (6328Å) of Flowing Carbon Monoxide Laser System. $P(N_2) = 506$ torr, $\dot{m}(N_2) = 0.8 g/sec$, $T = 296^\circ K$. (U)
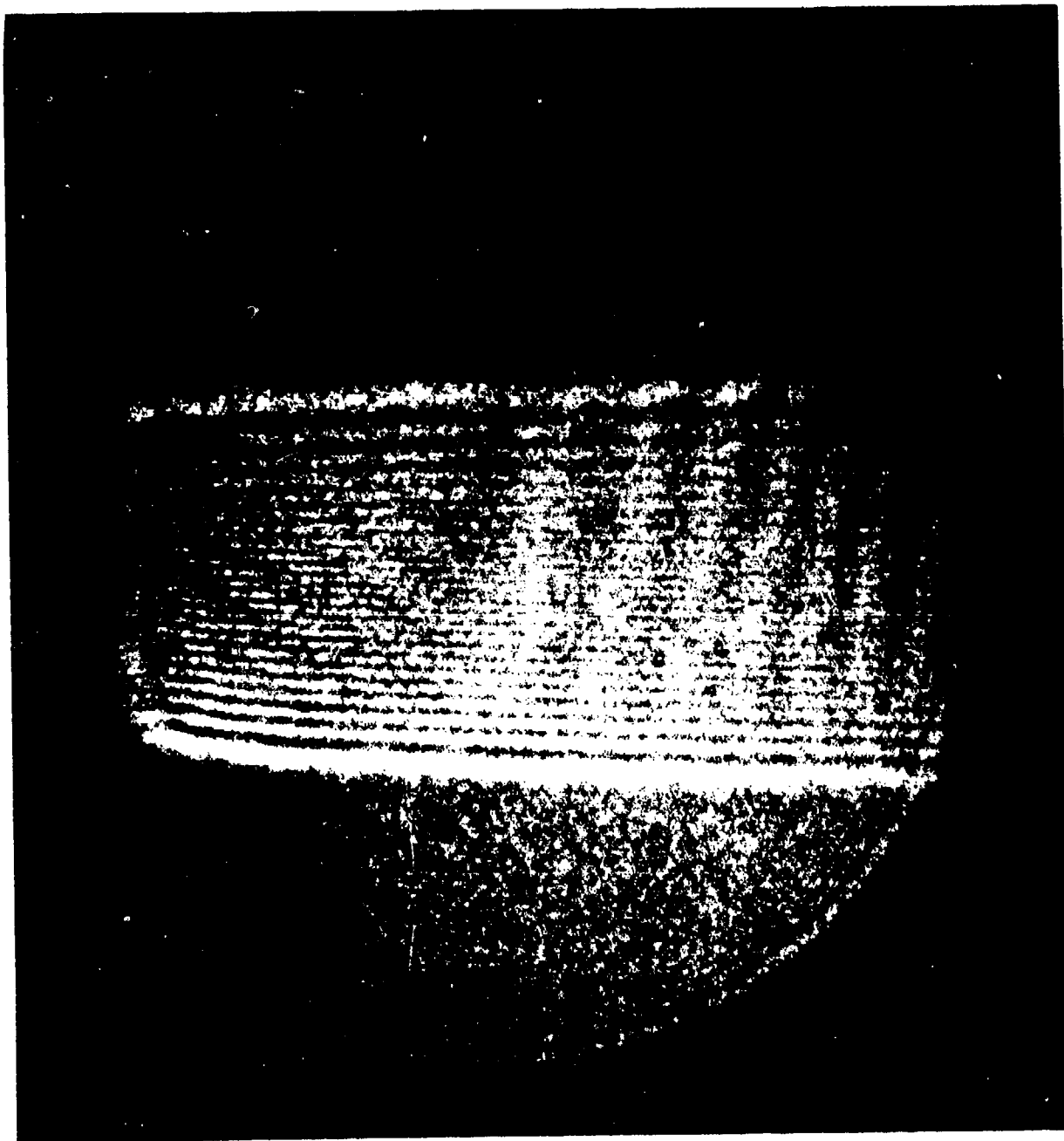
(U) Figure 3.9   Interferogram (6328 Å) of Flowing Cryogenic Carbon Monoxide Laser System. $P(N_2) = 107$ torr, $\dot{m}(N_2) = 2.71$ g/sec, $T \approx 80°K$. (U)

27

(U)   Figure 3. 10 shows an interferogram for essentially the same flow
rate as for Figure 3. 9 except for a slightly higher plenum pressure. With
the higher pressure the flow of the cryogenic gas is insufficient to provide
for a uniform temperature to the top of the plenum and thus a thermal
gradient occurs in the vertical plane. The focusing resulting from this
lensing effect causes the downward displacement visible in the figure.
The horizontal fringes still present confirm the optical homogeneity of
the medium. Figure 3. 11 shows a further displacement due to the in-
creased pressure at the same flow rate. Figure 3. 12 represents an even
higher pressure and the resulting distortion. Figure 3. 13 shows a
slightly higher pressure at the same flow rate; in this case the mirror
of the plenum leg of the interferometer has been adjusted to center the
pattern. The closely spaced horizontal fringes in this figure are a
result of the thermal gradient described previously and occurring because
of the adjustment of the rear mirror.

(U)   Figure 3. 14 shows the interferogram for essentially the same
plenum pressure as for the case of Figure 3. 9 but for a flow rate almost
twice the initial rate. Note that the pattern is wider than that of Figure 3. 9,
indicating a smaller temperature gradient between the gas and the Microy
fences, i. e., the fences are closer in temperature to that of the cryogenic
gas. The horizontal fringes again indicate the optical quality of the medium.

(U)   Figure 3. 15 gives the interferogram for approximately the same
plenum pressure as for Figure 3. 12 but with a higher flow rate. Note
the improvement in the pattern.

(U)   Figure 3. 16 shows the results for a mixed gas condition. The
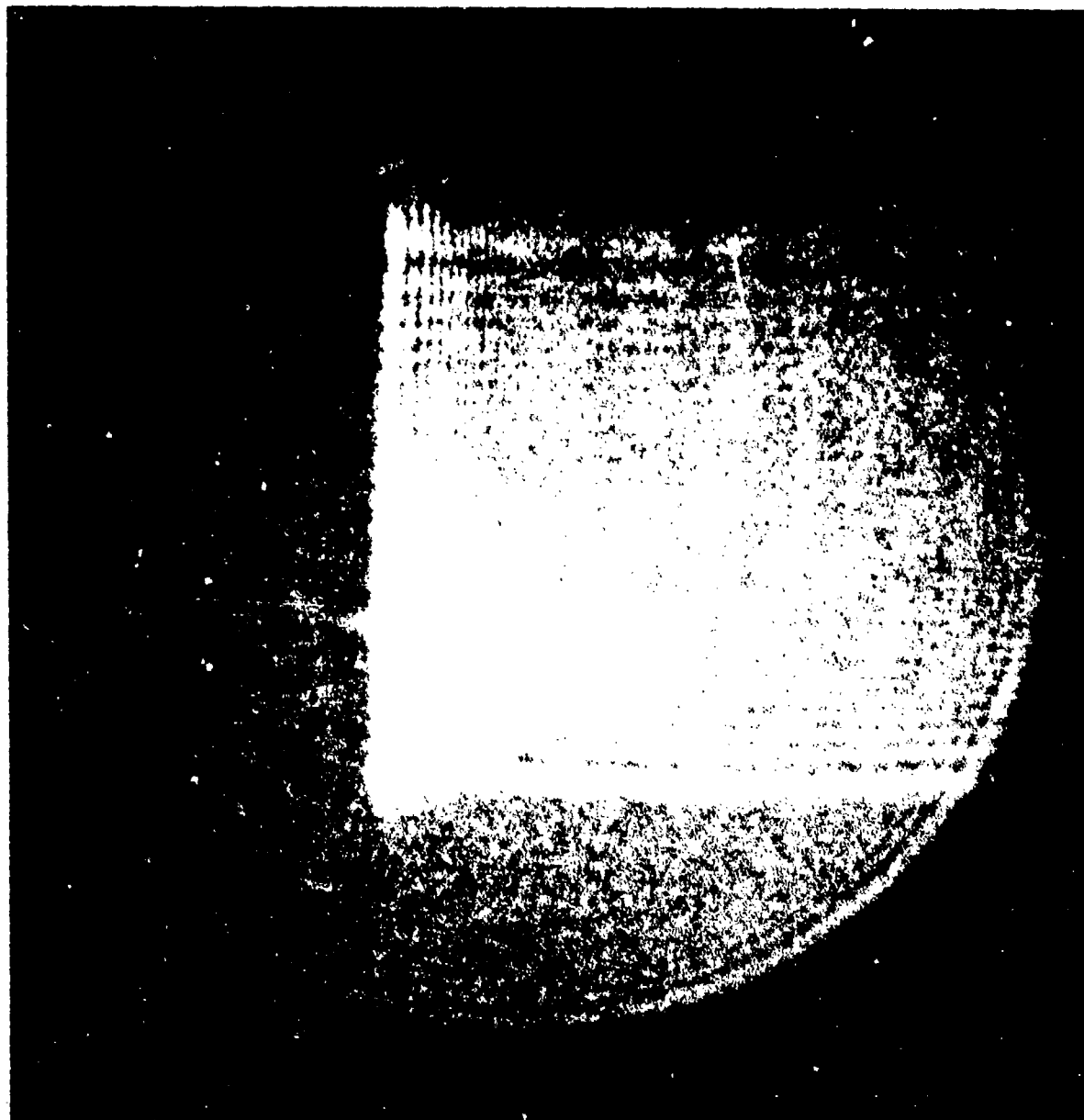total pressure is high as is the total flow rate for the argon-nitrogen

28
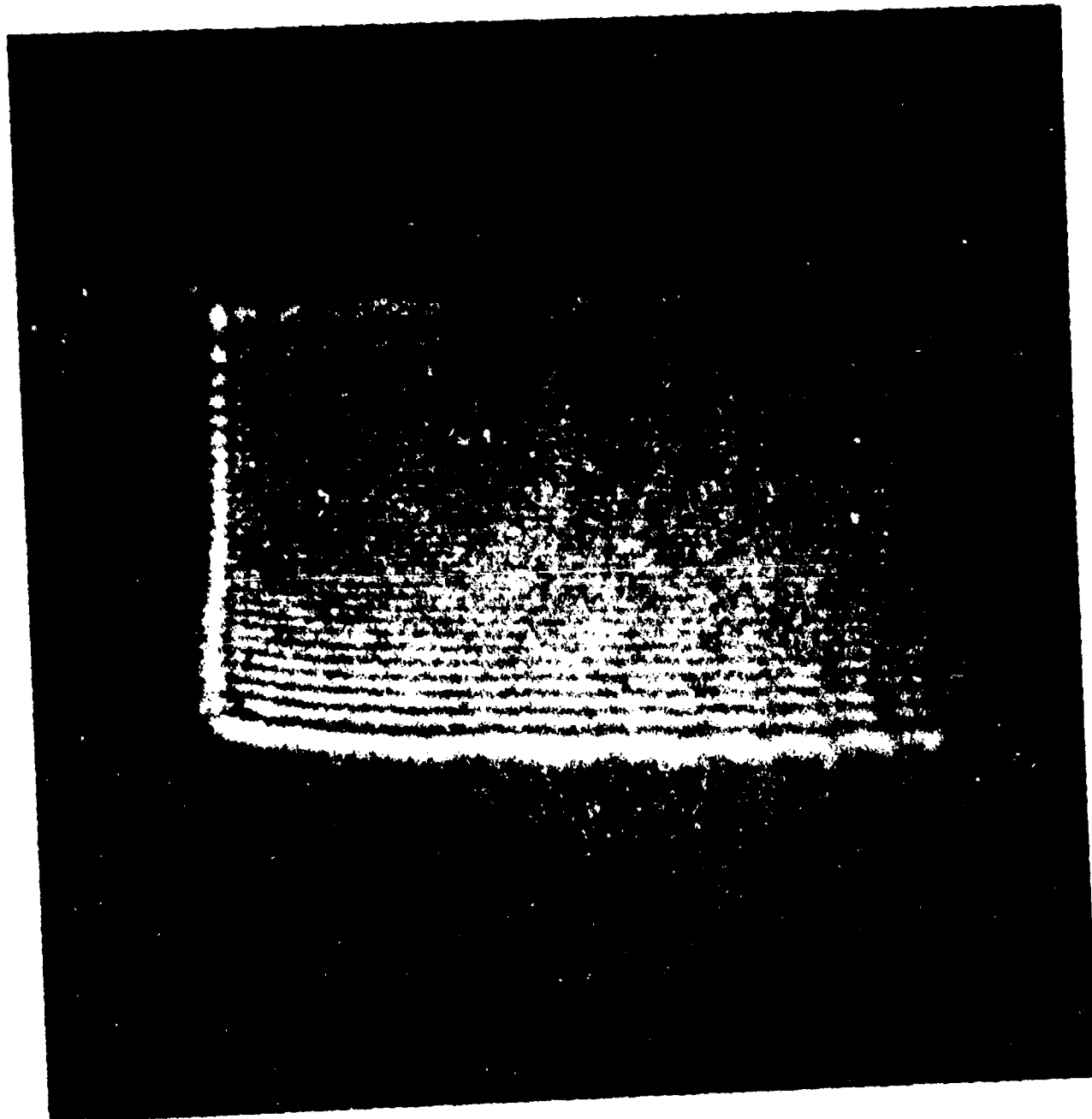
(U) Figure 3.10   Interferogram (6328Å) of Flowing Cryogenic Carbon Monoxide Laser System. $P(N_2) = 150$ torr, $m(N_2) = 2.79$ g/sec, $T \approx 80^{\circ}K$. (U)
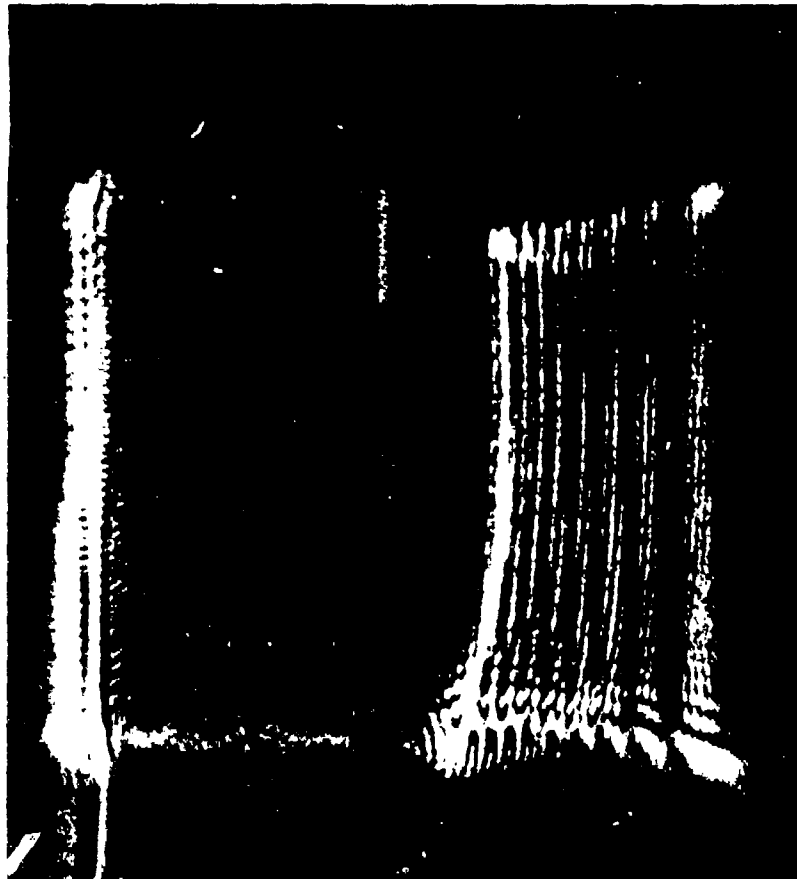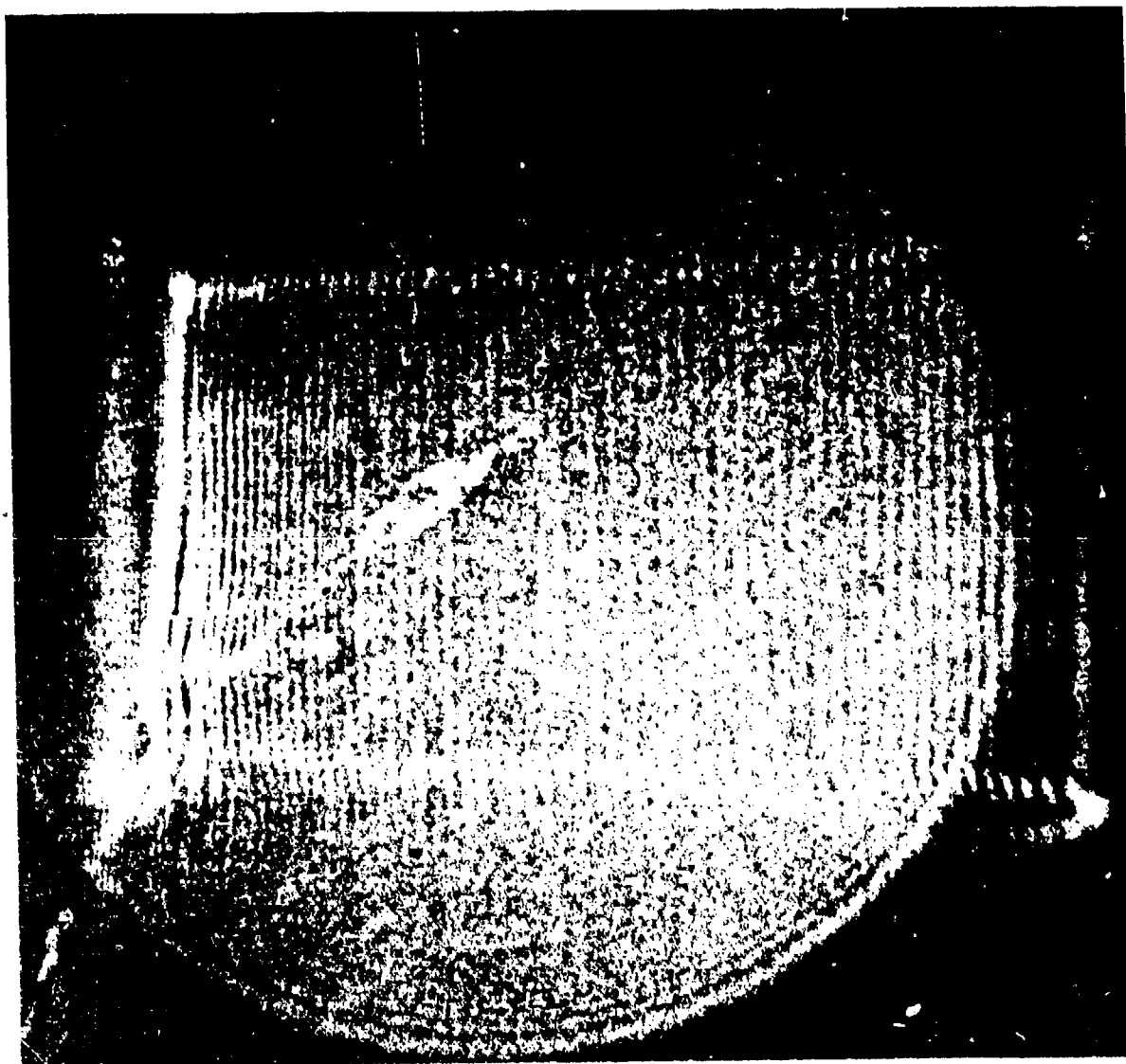
(U) Figure 3.11   Interferogram (6328Å) of Flowing Cryogenic Carbon Monoxide Laser System. $P(N_2) = 200$ torr, $\dot{m}(N_2) = 2.79$ g/sec, $T \approx 80°K$.   (U)

30

(U) Figure 3.12   Interferogram (6328Å) of Flowing Cryogenic Carbon Monoxide Laser System. $P(N_2) = 370$ torr, $\dot{m}(N_2) = 2.79$ g/sec, $T \approx 80°K$. (U)

31
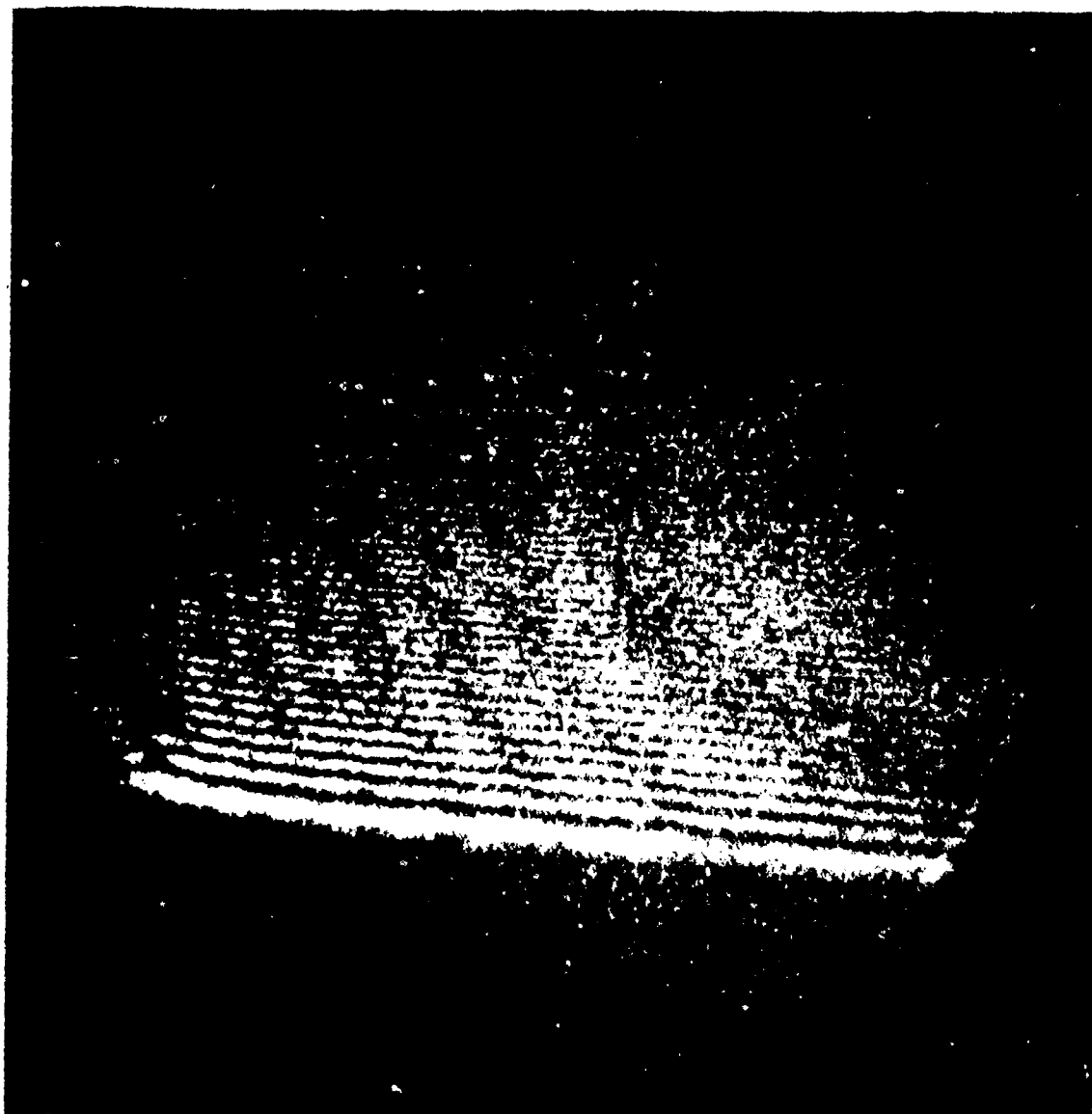
(U) Figure 3.13   Interferogram (6328A) of Flowing Cryogenic Carbon Monoxide Laser System. $P(N_2) = 400$ torr, $\dot{m}(N_2) = 2.79$ g/sec, $T \approx 80°K$. (U)

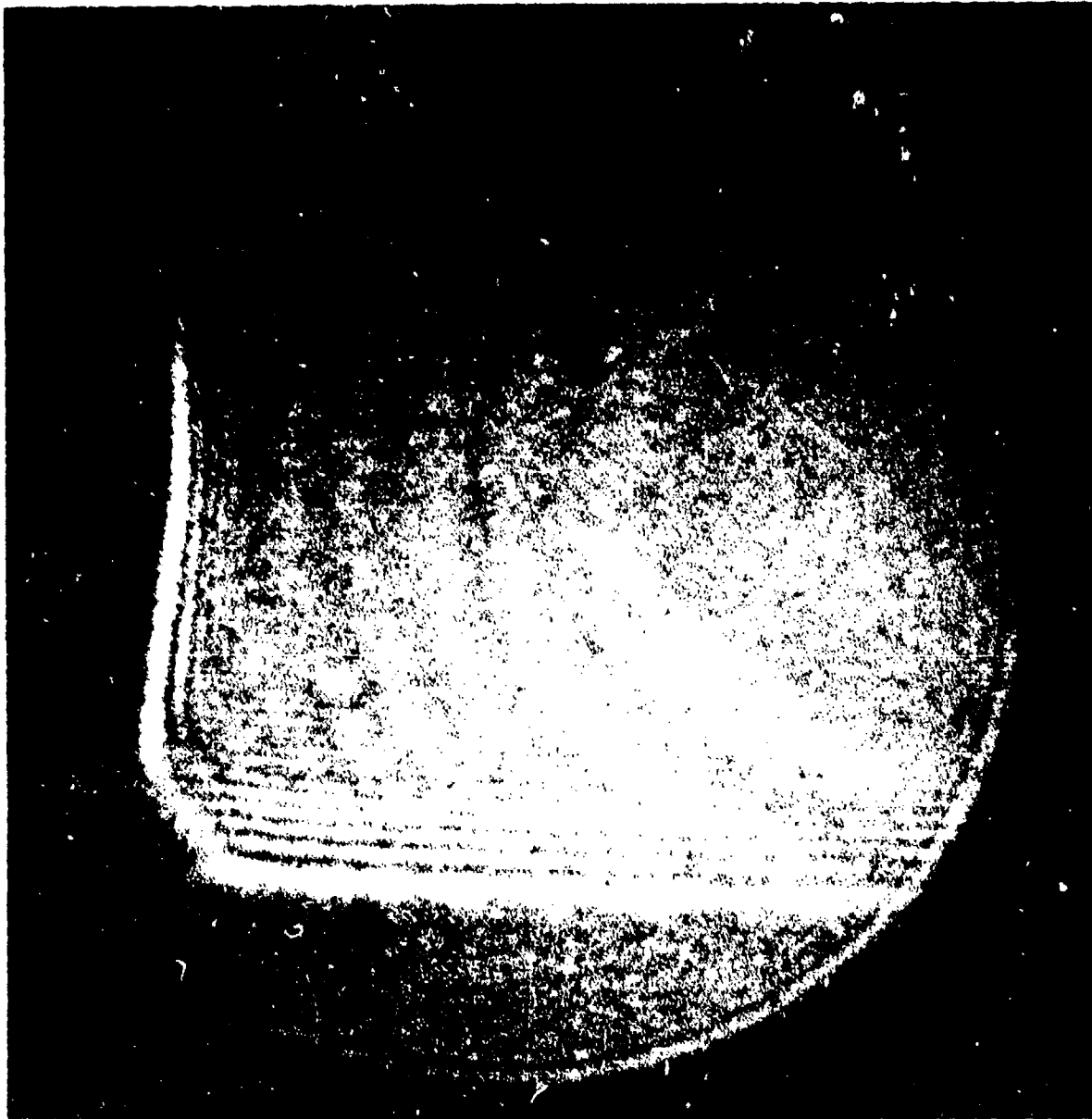(U) Figure 3.14 Interferogram (6328Å) of Flowing Cryogenic Carbon Monoxide Laser System. $P(N_2) = 100$ torr, $\dot{m}(N_2) = 4.66$ g/sec, $T \approx 80°$K. (U)
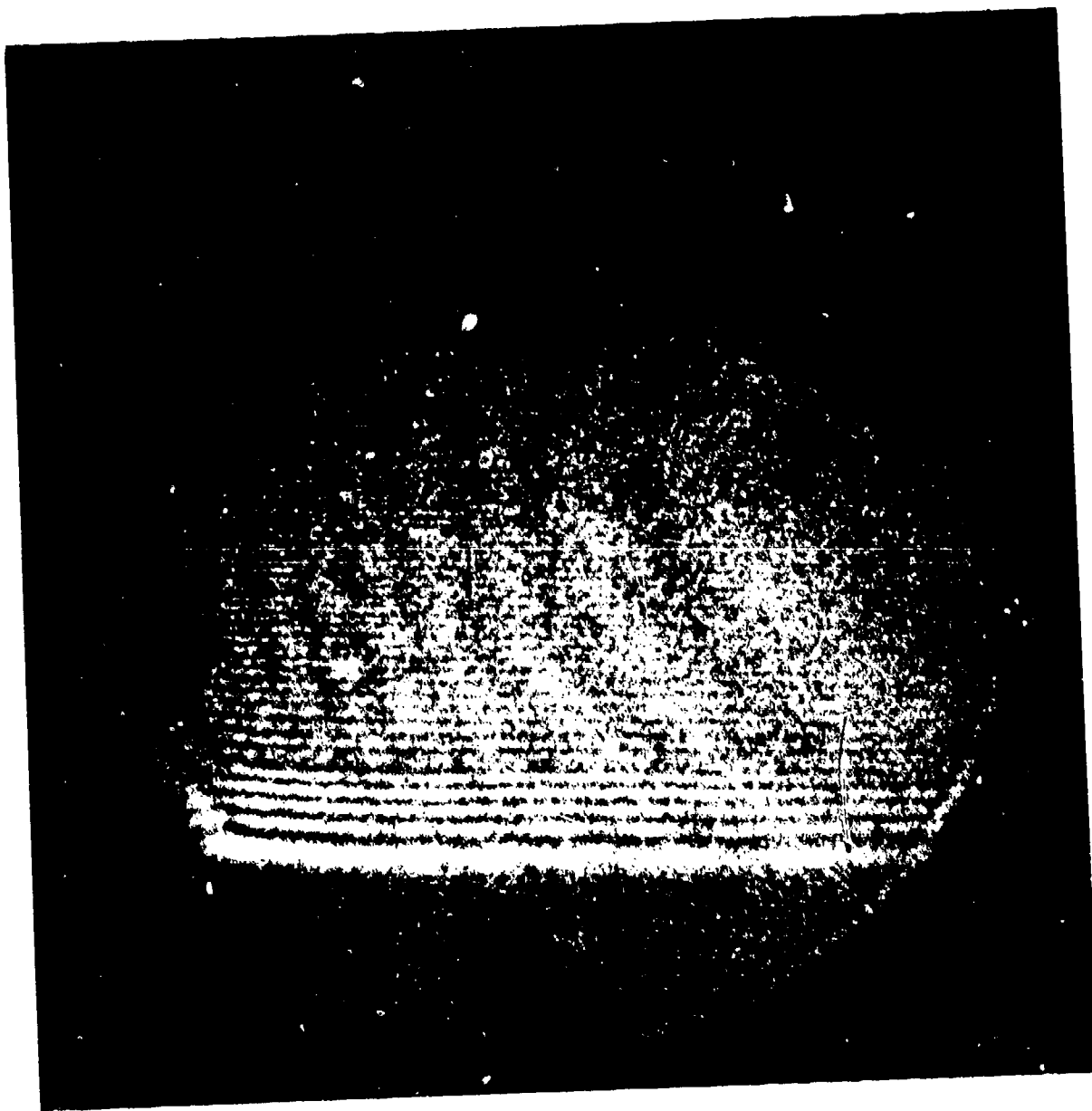
(U) Figure 3.15   Interferogram (6328Å) of Flowing Cryogenic Carbon Monoxide Laser System. $P(N_2) = 380$ torr, $\dot{m}(N_2) = 4.22$ g/sec, $T \approx 80°K$.   (U)

34

(U) Figure 3.16   Interferogram (6328Å) of Flowing Cryogenic Carbon Monoxide Laser System. $P(N_2) = 380$ torr, $P(Ar) = 165$ torr, $\dot{m}(N_2) = 2.92$ g/sec, $\dot{m}(Ar) = 5.43$ g/sec $T \approx 80°K.$ (U)

35

cryogenic mixture. The horizontal fringes show the superb optical quality of this combined gas flow system.

(U)   The results of this experiment demonstrate the achievement of a near-diffraction limited optically uniform medium consisting of cryogenic flowing gas using the scheme described in the previous section. It is also evident from these experiments that to properly utilize this flow scheme, the flow rate must be increased as the total plenum pressure is increased.
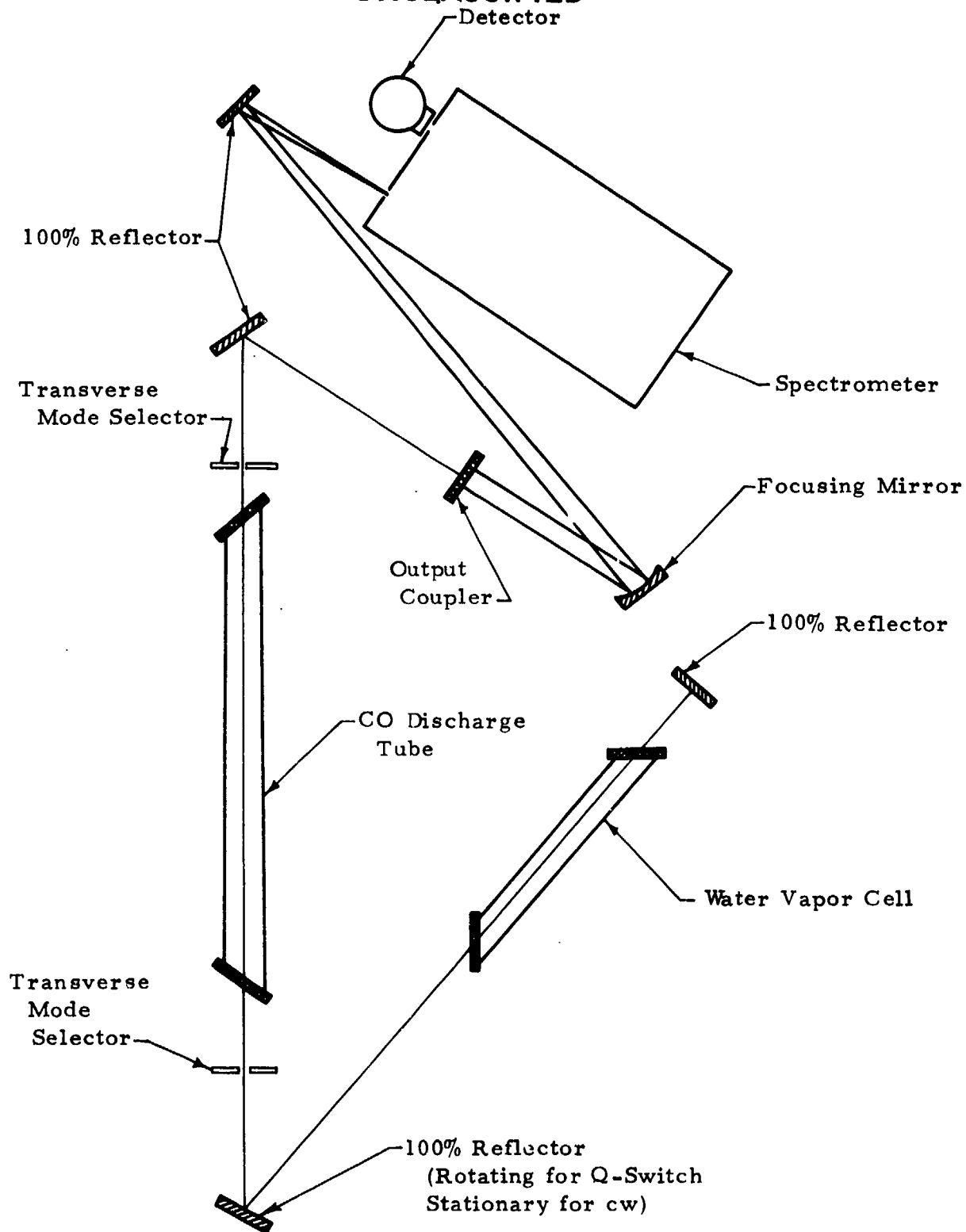
4.0   LINE SELECTION

4.1   Line Selection Experiments

4.1.1   (U) <u>Low Pressure Longitudinal Discharge Device.</u>   During this period of investigation experiments were performed using the configuration shown in Figure 4.1 to verify the water vapor cell spectral line selection technique with a low pressure-longitudinal discharge carbon monoxide laser. This setup is basically that used for the monochromatic loss measurements for water vapor described elsewhere.[1-4]   The construction of the vapor cell was detailed in an earlier report.[2]   For these experiments the cell temperature was maintained at $150^{\circ}C$, while the water vapor content was varied from 0 to 700 torr.   No additive broadening gases were used during this set of experiments.   The consequences of adding nitrogen or carbon dioxide on the absorption losses of the individual CO laser lines were discussed in the aforementioned report.[2]   The effect of the line selection technique on both Q-switched and cw operation was investigated.   As seen in Figure 4.1 the output of the laser is focused into a 1.0m, f/8.7 Czerny Turner mounting (Jarrell-Ash Model No. 78-466) spectrometer.   The mirror system for collecting and focusing the output beam had the same f-number as the spectrometer.   A liquid nitrogen cooled In:Sb detector (Cryogenics Associates) was used at the output of the spectrometer.   The output of the detector was processed using a boxcar integrator (PAR Model 160) and the spectra were recorded using a strip chart recorder (Hewlett Packard 7101B).   For signal processing purposes, the output for the cw configuration was modulated with a mechanical chopper.

(U)   The output spectrum of the Q-switched oscillator with no water vapor in the cell is shown in Figure 4.2.   Note that in order to generate the low vibrational band lines, the partial pressure of CO required is very low.   In addition, the discharge current is low compared to the normal 10 mA level. The low vibrational bands (6-5 and below) are desired because of the high atmospheric transmittance predicted for some of their rotational lines.   The
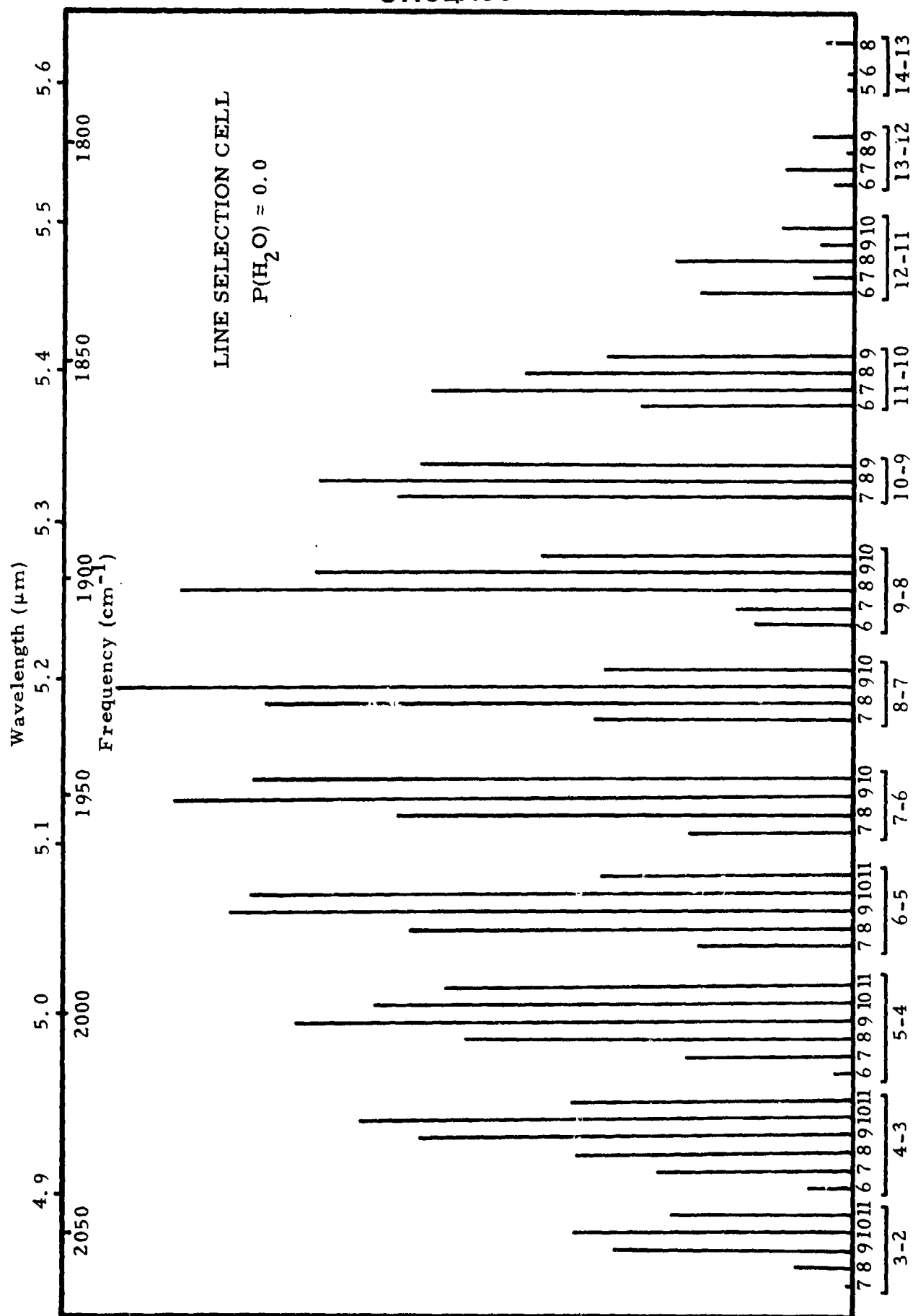
(U)Figure 4.1. Spectral Line Selection Configuration
for Low Pressure Longitudinal Discharge CO Laser (U)

38

(U) Figure 4.2. Output Spectra of Low Pressure Longitudinal Discharge, Repetitively Q-Switched (40 pps) CO Laser. $P_T = 7.0$ torr, $P(CO) = 0.06$, $P(N_2) = 0.99$, $P(O_2) = 0.004$, $P(He) = 5.94$. $I = 2.0$ ma. (U)

rotational cross relaxation of the medium is slow relative to the Q-switched pulse width because of the low operating pressure; this fact, as well as the increased gain per line with Q-switched operation explains why more than just one or two rotational lines oscillate in a particular vibrational band.

(U)   Figure 4.3 illustrates the effect of 400 torr of water vapor on the spectral output of the Q-switched laser. Only the net gain of the device can be changed by the water vapor since only loss is being added. The peak of the gain profile for the vibrational bands is seen to shift towards the lower bands since less loss is being added to these bands. Even the slight additional loss for the 3-2 band is too much to sustain oscillation on these lines. The effect of the absorption loss on the other bands is dramatic; many of the rotational lines have been eliminated, demonstrating that different losses have been added for each line. Figure 4.4 shows the results with 700 torr of water vapor, where oscillation has been limited to only the rotational lines with lowest loss in each band. These lines also have the highest pre-dicted atmospheric transmittance for each band. These results are very encouraging considering the slow rotational cross relaxation and high gain Q-switching effects.

(U)   Figure 4.5 illustrates the spectral output for cw operation of the laser. The gain is not sufficient to provide for oscillation of the 3-2 lines in the configuration of this experiment. Even though rotational cross relaxation is slow for the low operating pressures of this device, equilibrium can occur because of the continuous nature of the oscillation. Thus only one or two rotational lines are evident in this mode of operation. The percentage value shown above each line gives its fraction of the total output power. These numbers are obtained from the integrated output of the chart recorder. The parenthetical value above each line is its predicted atmospheric attenuation e-folding distance. Figure 4.6 shows the output spectra resulting from the addition of the water vapor cell containing 400 torr of water. Oscillation is

40

LINE SELECTION CELL

$P(H_2O) = 400$ torr @ $150^{\circ}C$
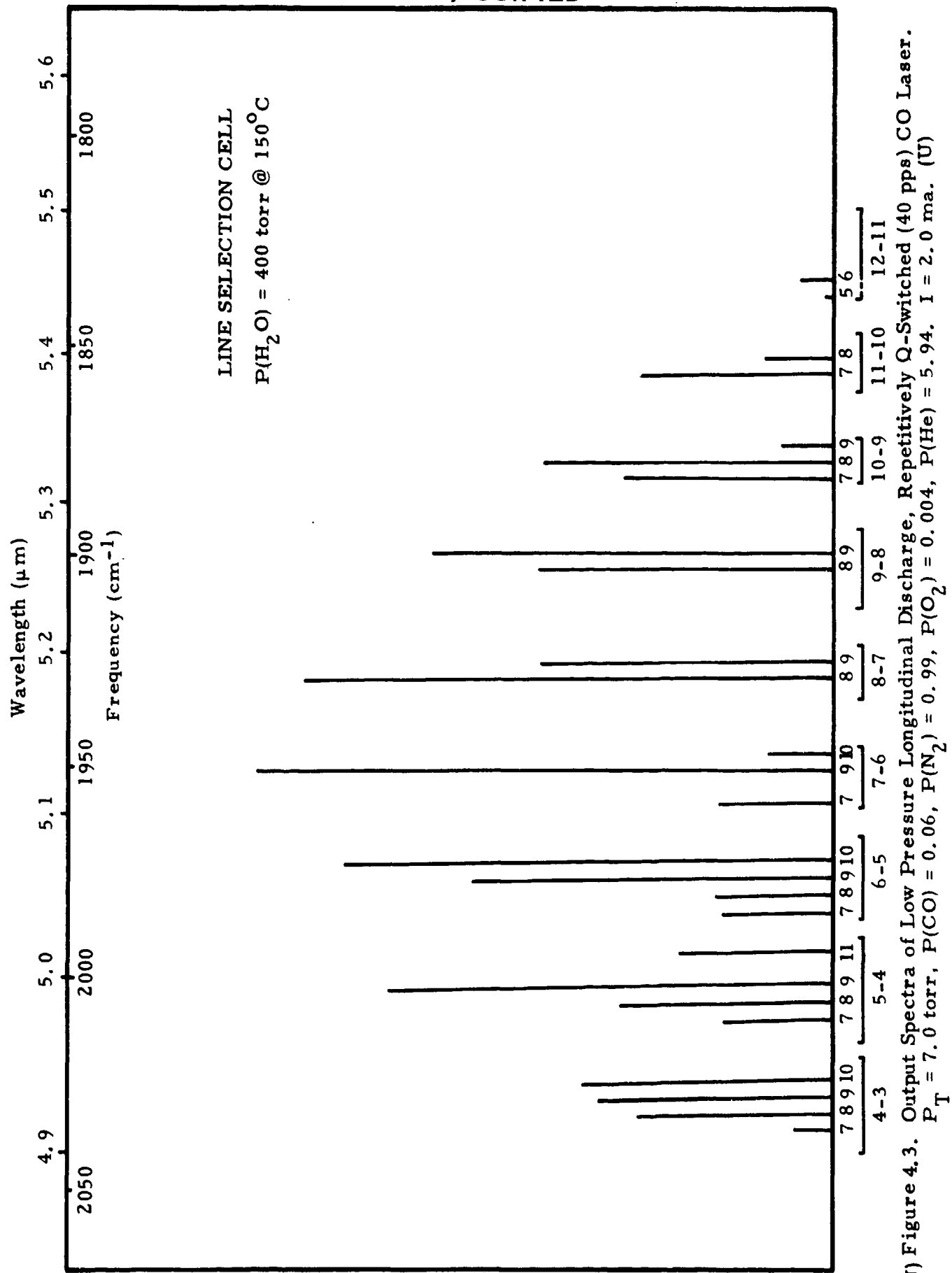
(U) Figure 4.3. Output Spectra of Low Pressure Longitudinal Discharge, Repetitively Q-Switched (40 pps) CO Laser. $P_T = 7.0$ torr, $P(CO) = 0.06$, $P(N_2) = 0.99$, $P(O_2) = 0.004$, $P(He) = 5.94$. $I = 2.0$ ma. (U)
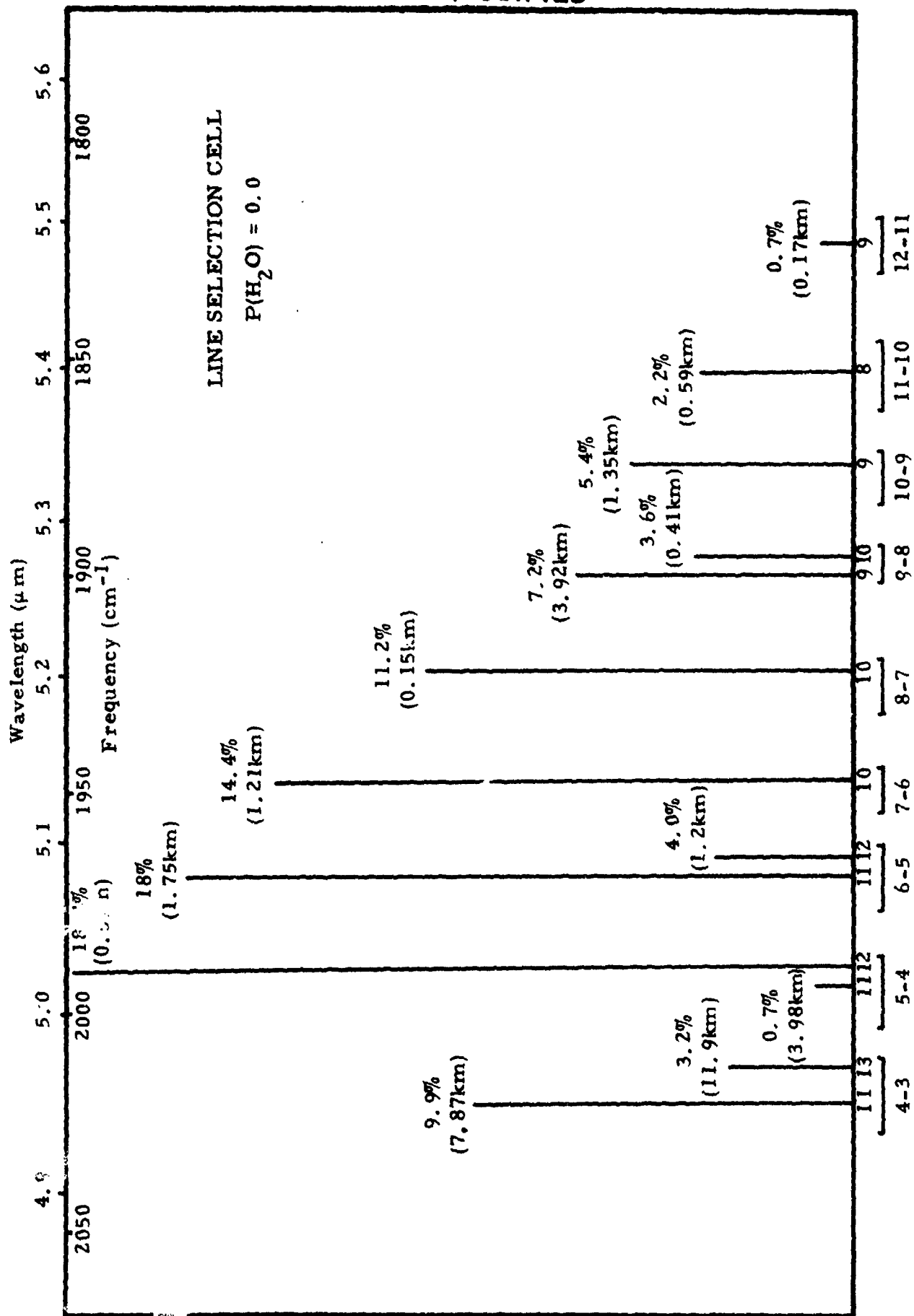
LINE SELECTION CELL

$P(H_2O) = 700$ torr @ $150^{\circ}C$
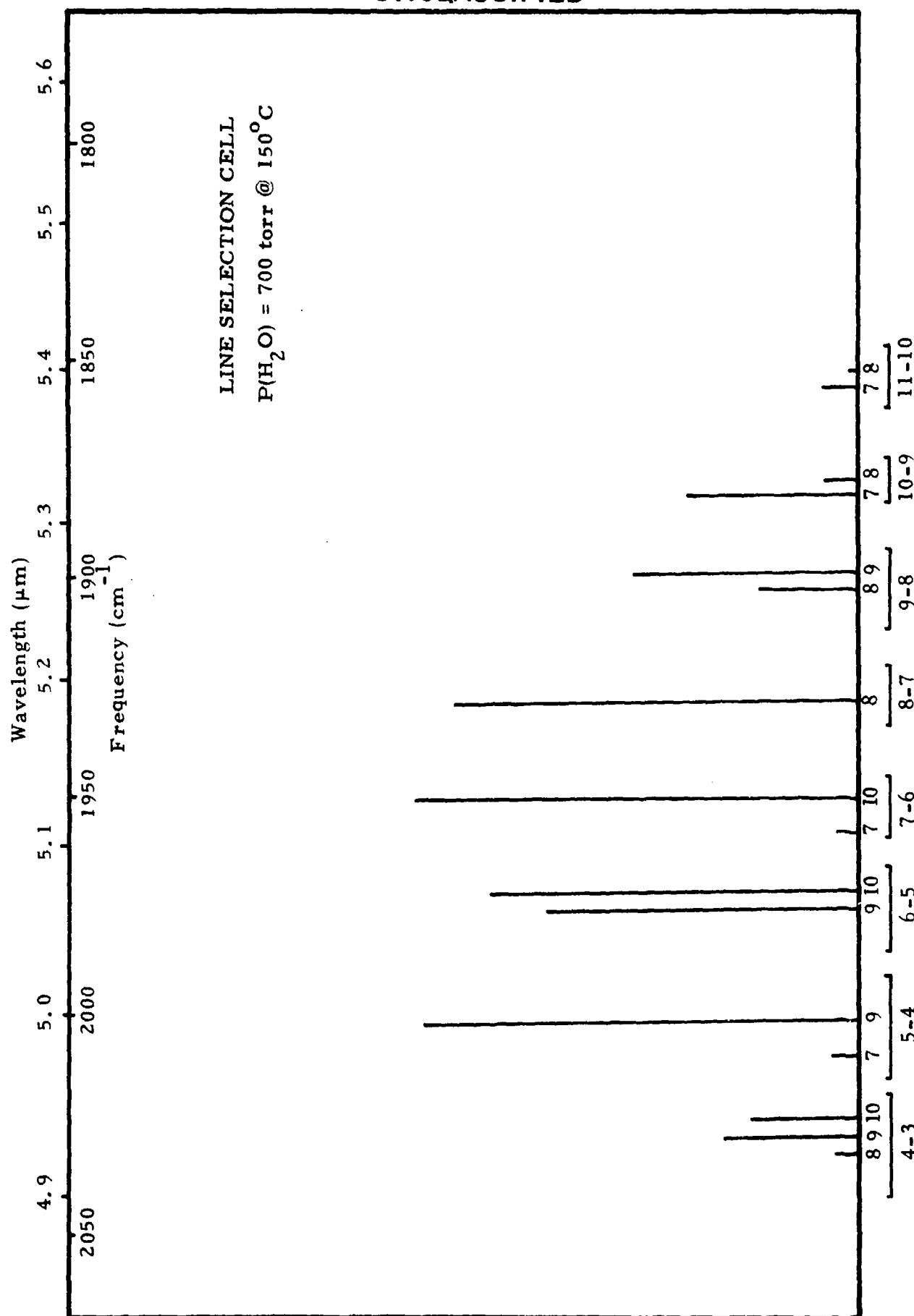
(U) Figure 4.4. Output Spectra of Low Pressure Longitudinal Discharge, Repetitively Q-Switched (40 pps) CO Laser. $P_T = 7.0$ torr, $P(CO) = 0.06$, $P(N_2) = 0.99$, $P(O_2) = 0.004$, $P(He) = 5.94$. $I = 2.0$ ma. (U)

(U) Figure 4.5. Output Spectra of Low Pressure Longitudinal Discharge cw CO Laser.

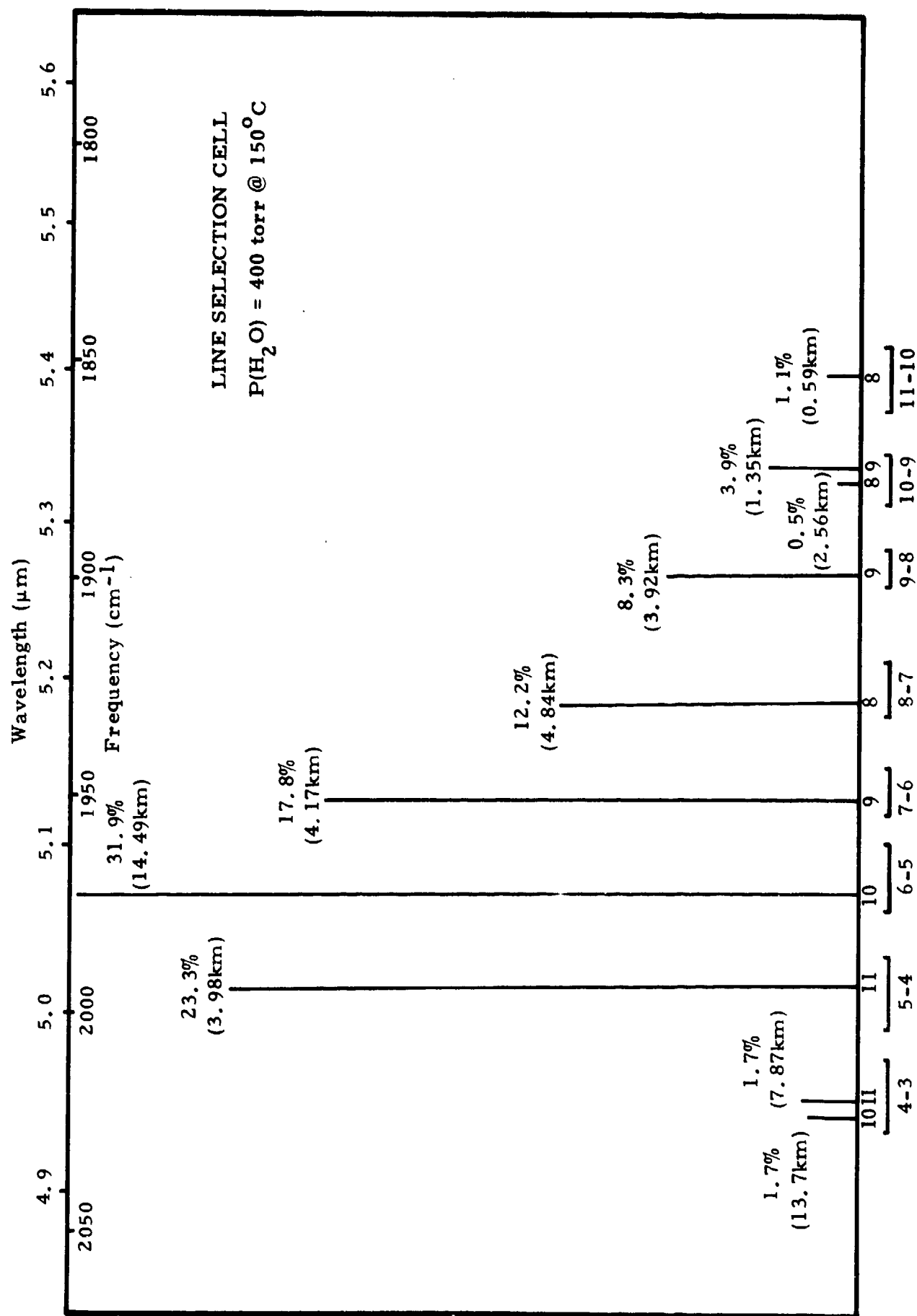P_T = 5.85 torr, P(CO) = 0.08, P(N_2) = 1.40, P(O_2) = 0.006, P(He) = 4.37, I = 2.0 ma. Output Power = 350 mw. (U)

(U) Figure 4.6. Output Spectra of Low Pressure Longitudinal Discharge cw CO Laser.

P_T = 5.85 torr, P(CO) = 0.08, P(N$_2$) = 1.40, P(O$_2$) = 0.006, P(He) = 4.37, I = 2.0 ma. Output Power - 240 mw. (U)

tending to shift from the rotational lines of Figure 4.5 to those lines having the highest atmospheric transmittance. The tendency is also towards one rotational line per vibrational band. Figure 4.7 shows the output spectra with 700 torr of water vapor. Only one rotational line is oscillating in each vibrational band. Note that 63% of the output power is contained in the high transmission lines in the 6-5 band and lower. Not only has the water vapor initiated rotational line selection, it has also provided for vibrational line selection by prohibiting oscillation on the high vibrational bands. The output power dropped from 350 mW without water vapor in the cell to 150 mW with 700 torr of water vapor. If the gain of the laser could be peaked in the lower vibrational bands, the efficiency using line selection would be greatly improved.

(U)   Additional data was taken in both the Q-switched and cw configurations for various amounts of water vapor in the cell. These results will be presented in a subsequent report.

4.1.2 (U) <u>High Pressure E-Beam Device</u>. During this period the spectral line selection of an E-beam CO laser was demonstrated. The configuration for the experiment is shown in Figure 4.8. The water vapor cell used was the same device as discussed in Section 4.1.1. The output energy was focused into the spectrometer (Optical Engineering CO Spectrum Analyzer). The fluorescent screen of the spectrometer and resulting spectra of the laser pulse is recorded photographically.

(U)   The results of these experiments are shown in Figure 4.9. The vertical lines illustrate only spectral location and not intensity. The value above each line represents the predicted atmospheric e-folding distance. The pertinent parameters of the laser are listed in the figure. The output consists of a single pulse with a temporal width of approximately 100 μsec. The spectra at the top of the figure is for the output with no water vapor in the cell. The addition of 400 torr of water vapor results in the spectra in the center of
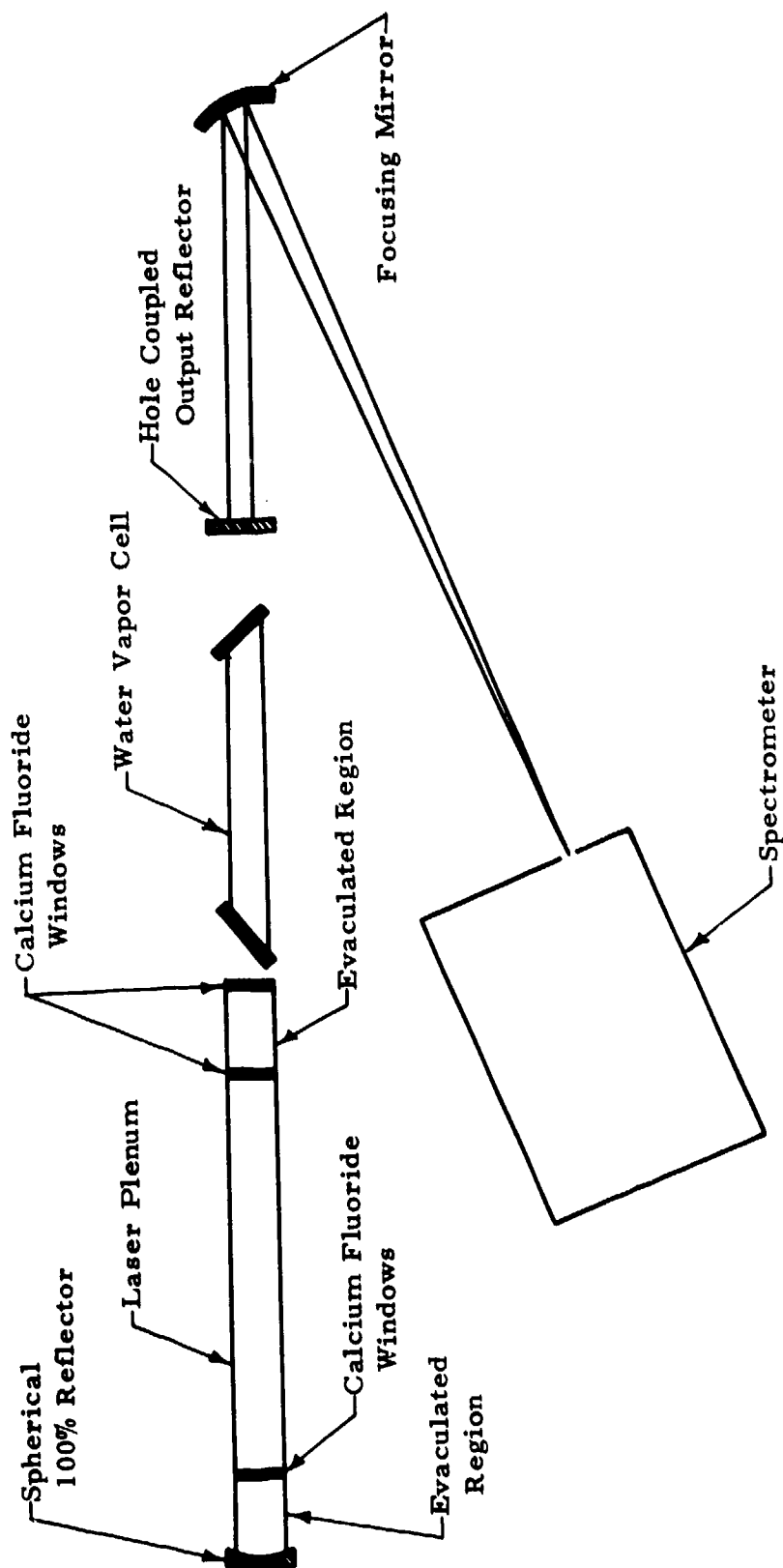
45
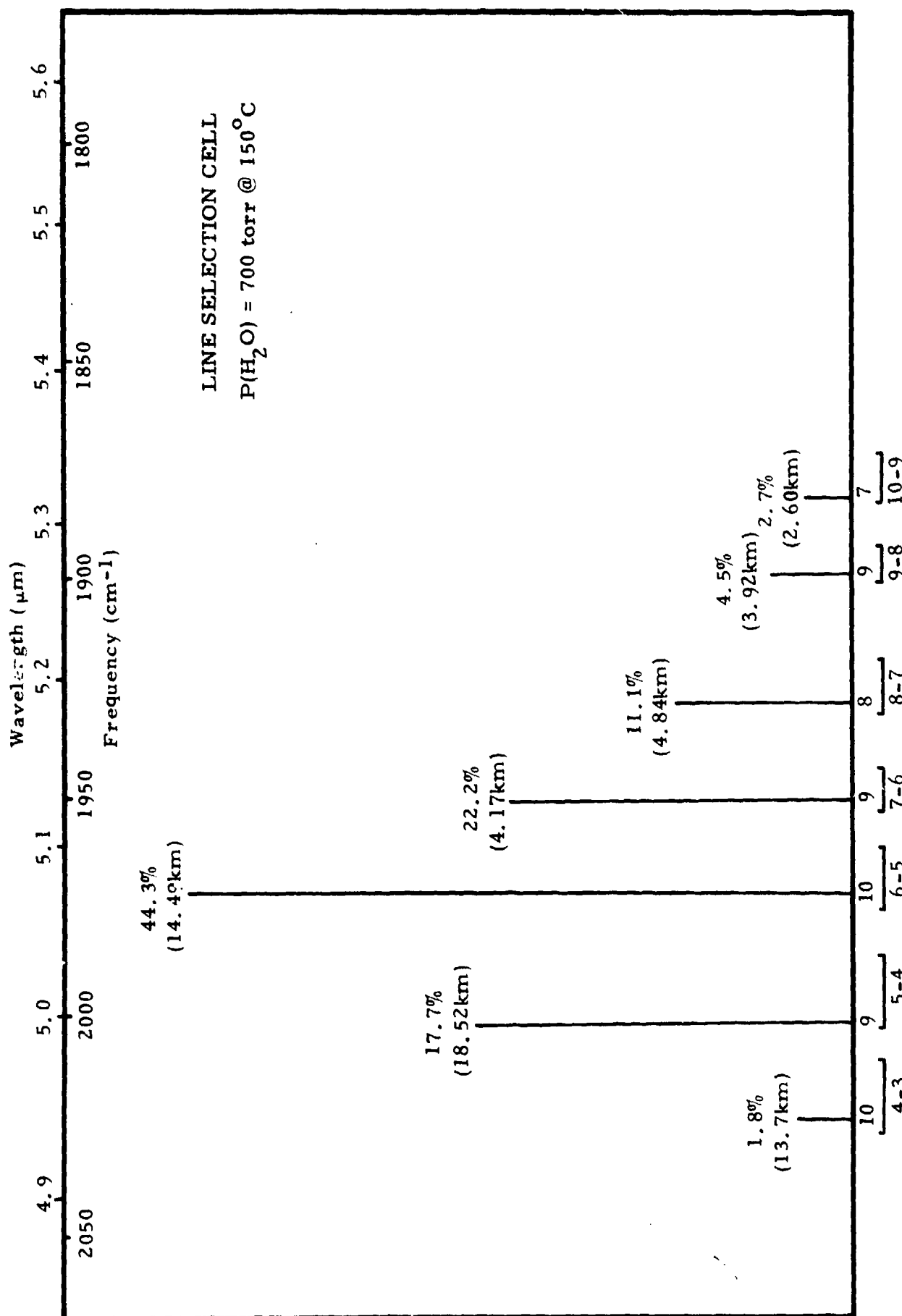
(U) Figure 4.7. Output Spectra of Low Pressure Longitudinal Discharge cw CO Laser.
P_T = 5.85 torr, P(CO) = 0.08, P(N$_2$) = 1.40, P(O$_2$) = 0.006, P(He) = 4.37, I = 2.0 ma. Output Power = 150 mw. (U)

(U) Figure 4.8. Spectral Line Selection Configuration for No. 1 Device (U)

47

(U) Figure 4.9. Line Selection Performance of E-Beam CO Laser
$P_T = 100$ torr   CO:N$_2$ = 1:5   T = 79°K   Pump Rate = 1.4 kw/cc (U)

48

Figure 4.9. Similar to the cw operation of the low pressure longitudinal discharge laser described in Section 4.1.2, the oscillation tends to shift to rotational lines having the least loss. The spectral results for 700 torr of water vapor are illustrated in the bottom figure. Only one rotational line is present for each vibrational band. These lines have higher predicted atmospheric transmittance than the lines with no line selection. In addition a certain amount of vibrational line selection has occurred.

(U)   The configuration of this particular E-beam laser does not have the optimum cross sectional aspect ratio to provide the required electrical pumping to limit oscillation to only the lower vibrational bands. As discussed previously, these low vibrational bands contain the rotational lines having the highest predicted atmospheric transmission. With the proper pumping configuration, the efficiency of the laser is predicted to be affected minimally by the line selection device.

(U)   The line selection device used in these experiments has a 1.0 inch diameter clear aperture and thus only a small section of the active medium could be utilized due to vignetting. A 6.0 inch clear aperture vapor cell is currently under construction for future experiments.

4.2   Atmospheric Transmittance

4.2.1   (U) Atmospheric Attenuation Measurements. Until the recent White cell measurements of Long,[5] the only experimental CO laser results available were the high water vapor pressure data determined in our laboratory[1-4] and Gilmartin's out-of-doors data.[6] Our measurements were made at water vapor pressures from 100 to 300 torr and at a temperature of 150°C. The experiments were performed for 20 of the CO laser lines using an intracavity absorption cell and a technique described in detail in previous reports.[1-4] The conclusion from the results of these experiments was that at water vapor pressures of 100 torr (150°C), the losses introduced for the CO emission lines agreed

49

reasonably well with those predicted using the theoretical model. For water vapor pressures larger than 100 torr, the measured losses were greater than predicted. Since, at least theoretically, the absorption coefficient is not an extreme function of temperature, it was presumed from our results that if the water vapor absorption losses at pressures of 100 torr agreed with the theoretical predictions then the transmission for atmospheric type pressures (~10 torr) would be better than (or at least equal to) the theoretical estimations.

(U)   The results reported by Long[5] contradicted this conclusion. He made measurements for water vapor pressures up to 15 torr for 11 of the CO laser lines and for all of the lines measured, the loss was greater than theoretically predicted.

(U)   In order to resolve the apparent inconsistency between our results and Long's, during the period of investigation we modified our experimental setup to measure the atmospheric attenuation for several of the CO emission lines. The primary modification of the setup was to transfer the CaF_2 Brewster plate loss measuring device into the resonator containing the water vapor cell. The calibration mode consisted of filling the cell with ambient air. With ambient air in the cell, the pulses from both resonators are identical. When the cell is evacuated (0.01 torr), the pulse from the corresponding resonator becomes larger than the other as a result of the removal of 71 cm path of water vapor in the air. The Brewster plate was then rotated to introduce a reflective loss equivalent to the absorptive loss removed so that pulse 2 has the same energy content as pulse 1. The amount of loss is determined from the calibrated loss curve of the Brewster plate as a function of its angle. Since the path length was so short, the measurements were limited to 5 CO laser lines exhibiting a detectable loss over this distance. The water vapor content was determined using a fixed psychrometer with forced air flowing past the wet and dry bulb thermometers.

50

(U)   The results of the measurements are shown in Figures 4. 10-4. 14.
The data for all 5 lines is very consistent. In each case, the experimentally
measured absorption coefficient is less than that calculated using the standard
theoretical model. Again there appears to be a contradiction between our
results and Long's. However, the CO spectral lines of Figures 4. 10-4. 14
are located very near the line center of strong water vapor lines while Long's
measurements involved laser emissions in the wings of strong water vapor
lines.[7] Thus, the inconsistency appears to be in the theoretical model and
not the experiments. The model commonly used is not adequate in predicting
the water vapor attenuation for the CO laser lines. The model could be
modified to provide calculated losses which agree with measured results for
a particular set of conditions for particular laser wavelengths but the same
modification could not be expected to be sufficient for another laser frequency
and/or set of conditions. In other words, extrapolation is unreliable. For
example, the absorption coefficients for two of the CO laser lines having
predicted high atmospheric transmittance [5-4 P(16) and 5-4 P(15)] have been
measured[5] and the results indicate that the atmospheric attenuation for these
lines is higher than predicted. However, it would be unwise to extrapolate
the values for these lines to other predicted high transmission laser lines.
Until measurements are made on these other lines, their value for atmospheric
propagation is uncertain.

4.2.2 (U) Comparison of CO and CO_2 . The atmospheric transmittance
(calculated or measured) of the CO emission lines is continually referenced
to the 10 km e-folding distance of the CO_2 P(20) laser line. Of course, this
10 km distance is for a unique set of conditions, i.e., a particular atmospheric
model. The Midlatitude Winter Model with a horizontal path at sea level
specified the conditions for this 10 km distance and thus most comparisons
of CO transmission to CO_2 transmission to date have been for these same
conditions. There are actually ten model atmospheres[8] given by the winter
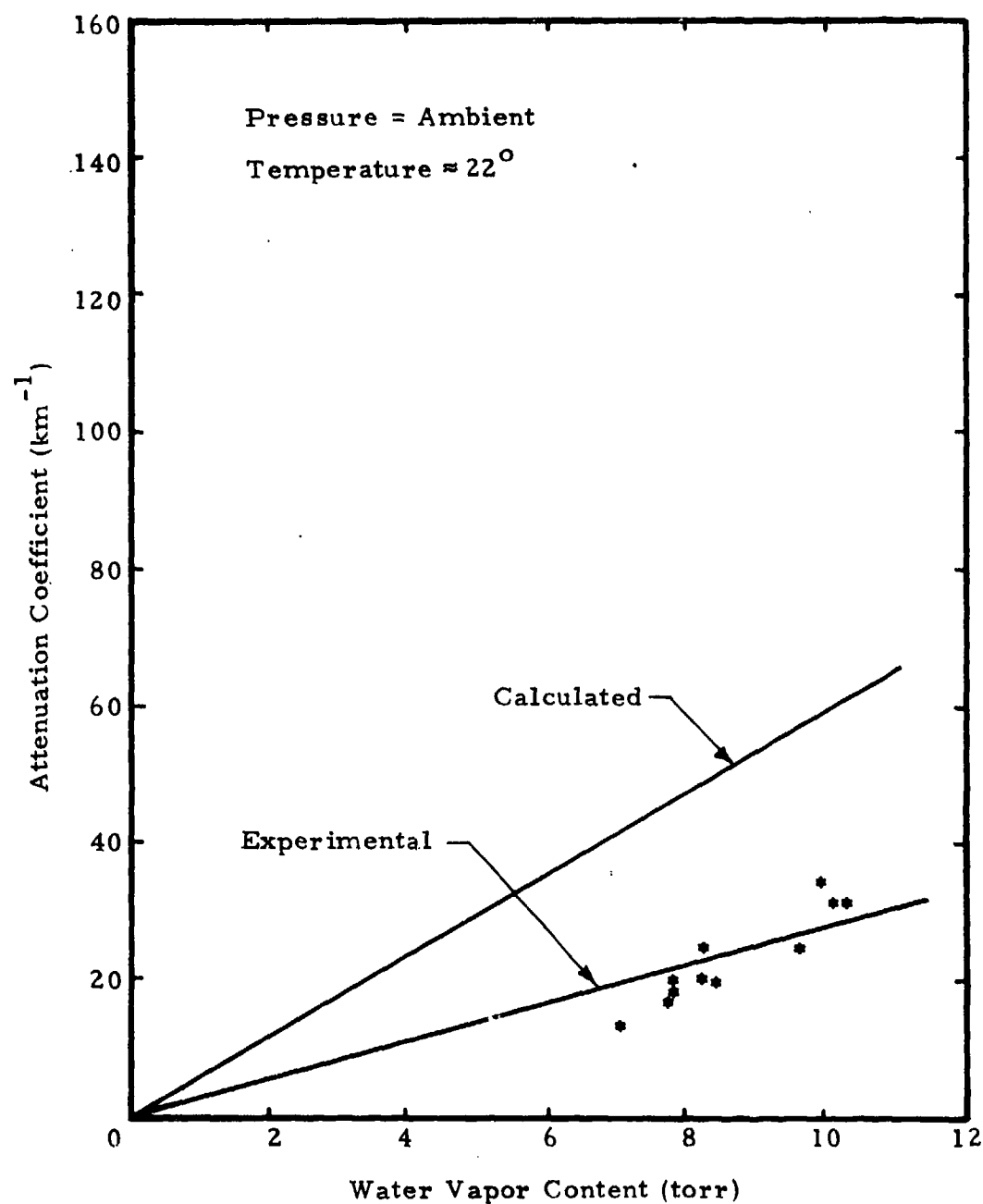(January) and summer (July) variations of the Tropical, Subtropical,

51
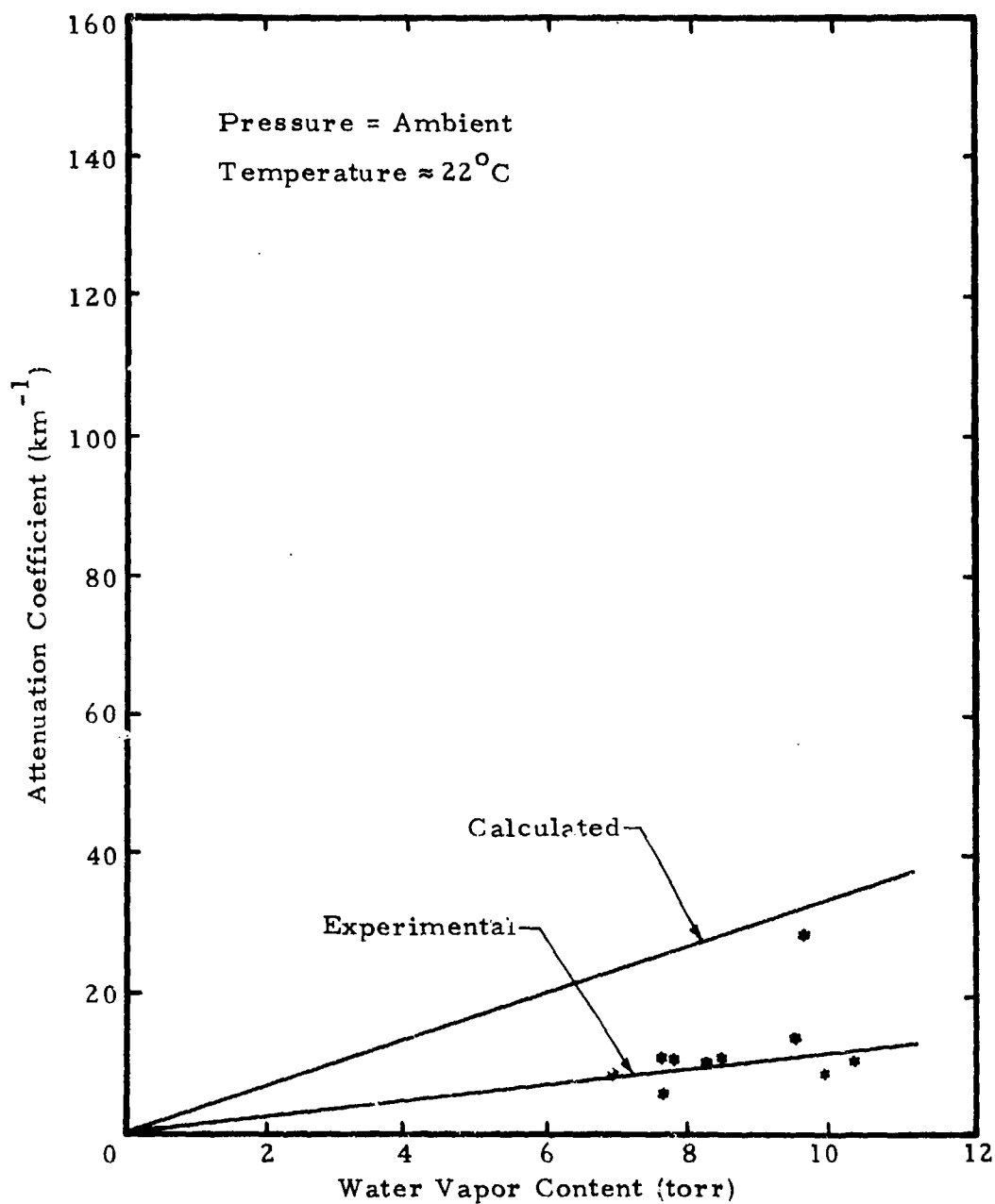
(U)   Figure 4.10. Atmospheric Attenuation Coefficient of
9-8P(13) $[1884.342 \text{ cm}^{-1}]$ CO Laser Line vs Water Vapor Content (U)

Pressure = Ambient

Temperature ≈ 22°

Calculated

Experimental

Water Vapor Content (torr)
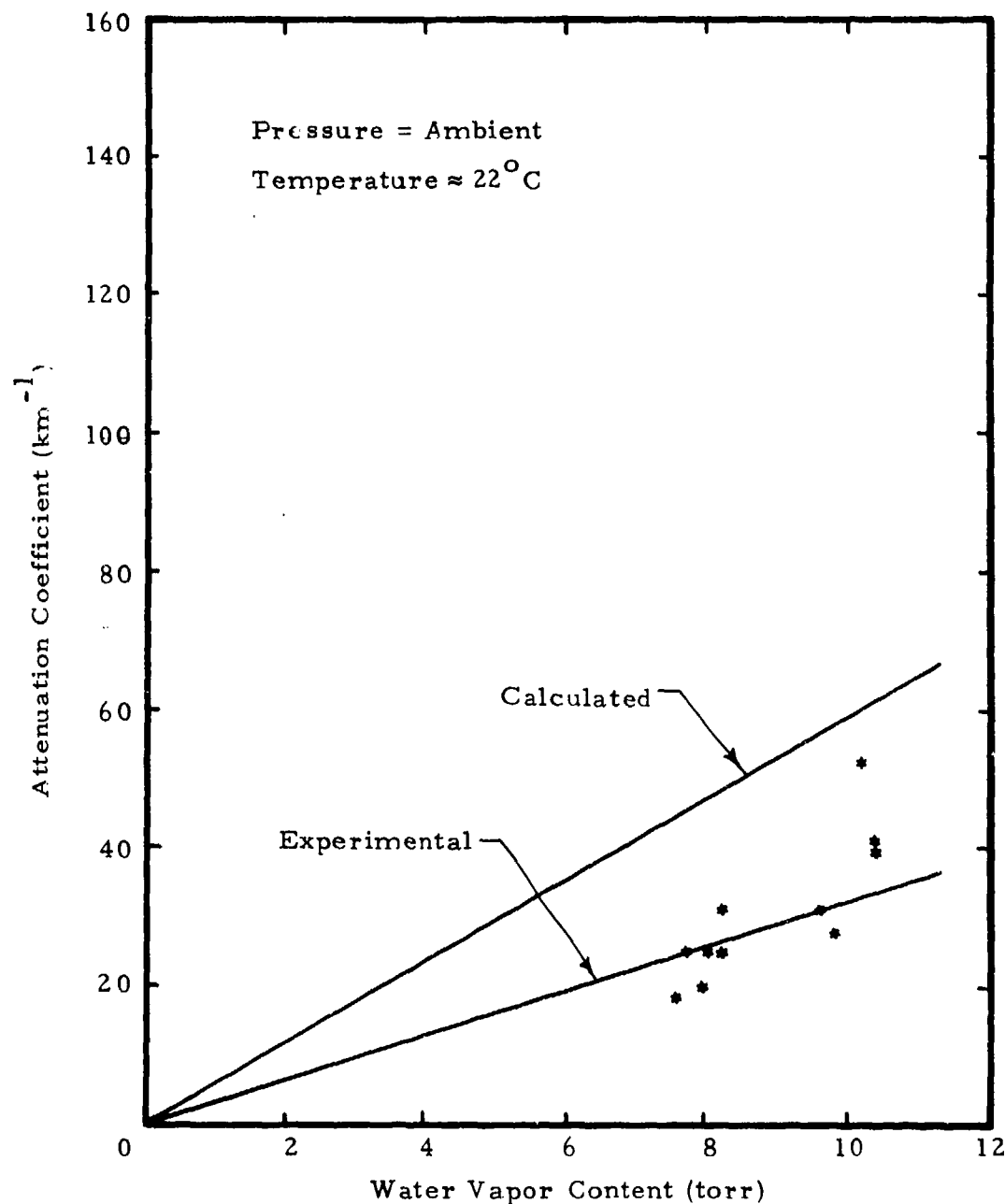
(U)   Figure 4.11. Atmospheric Attenuation Coefficient of
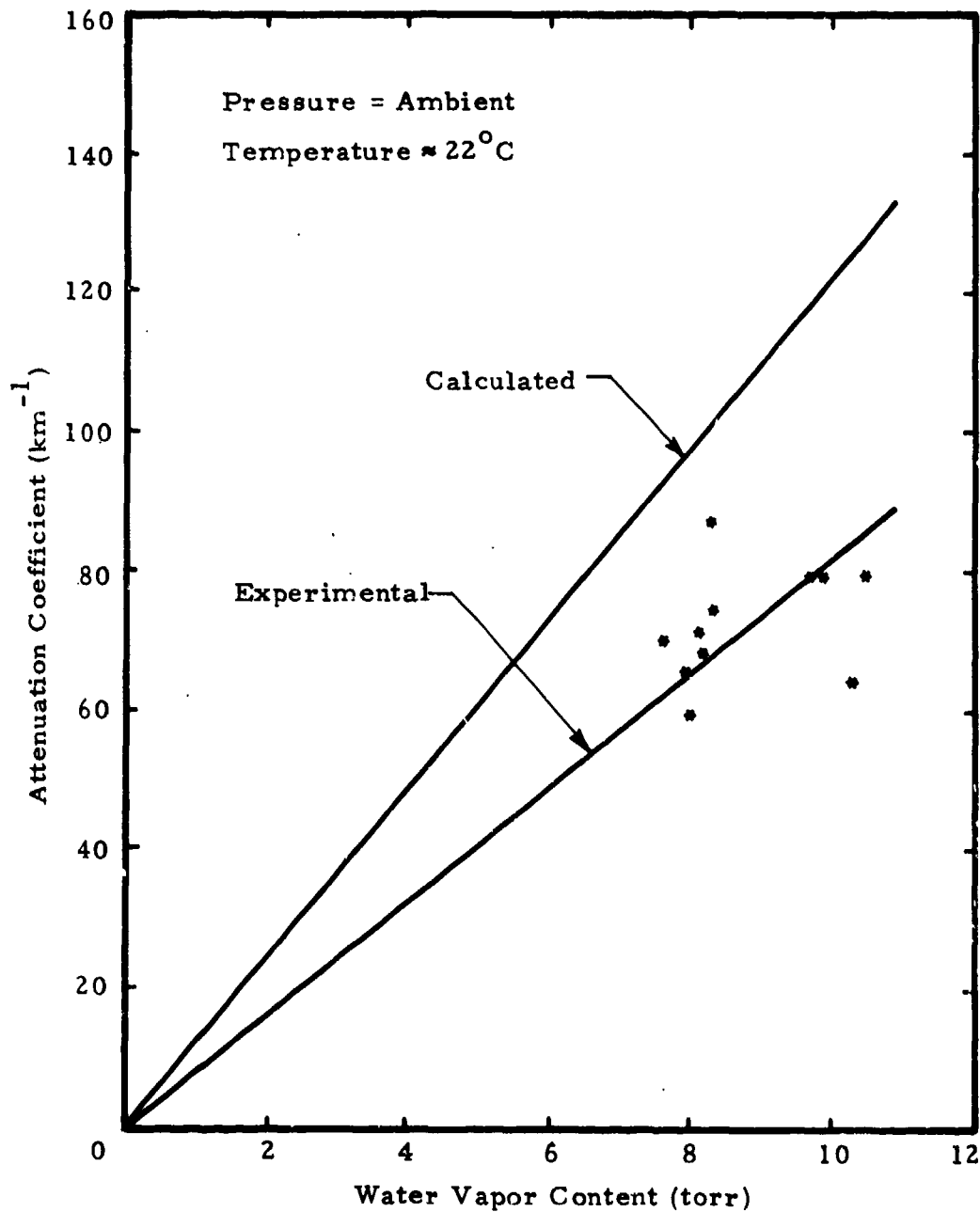10-9P(10) $[1870.607 \text{ cm}^{-1}]$ CO Laser Line vs Water Vapor Content (U)

53

(U)   Figure 4.12.   Atmospheric Attenuation Coefficient of
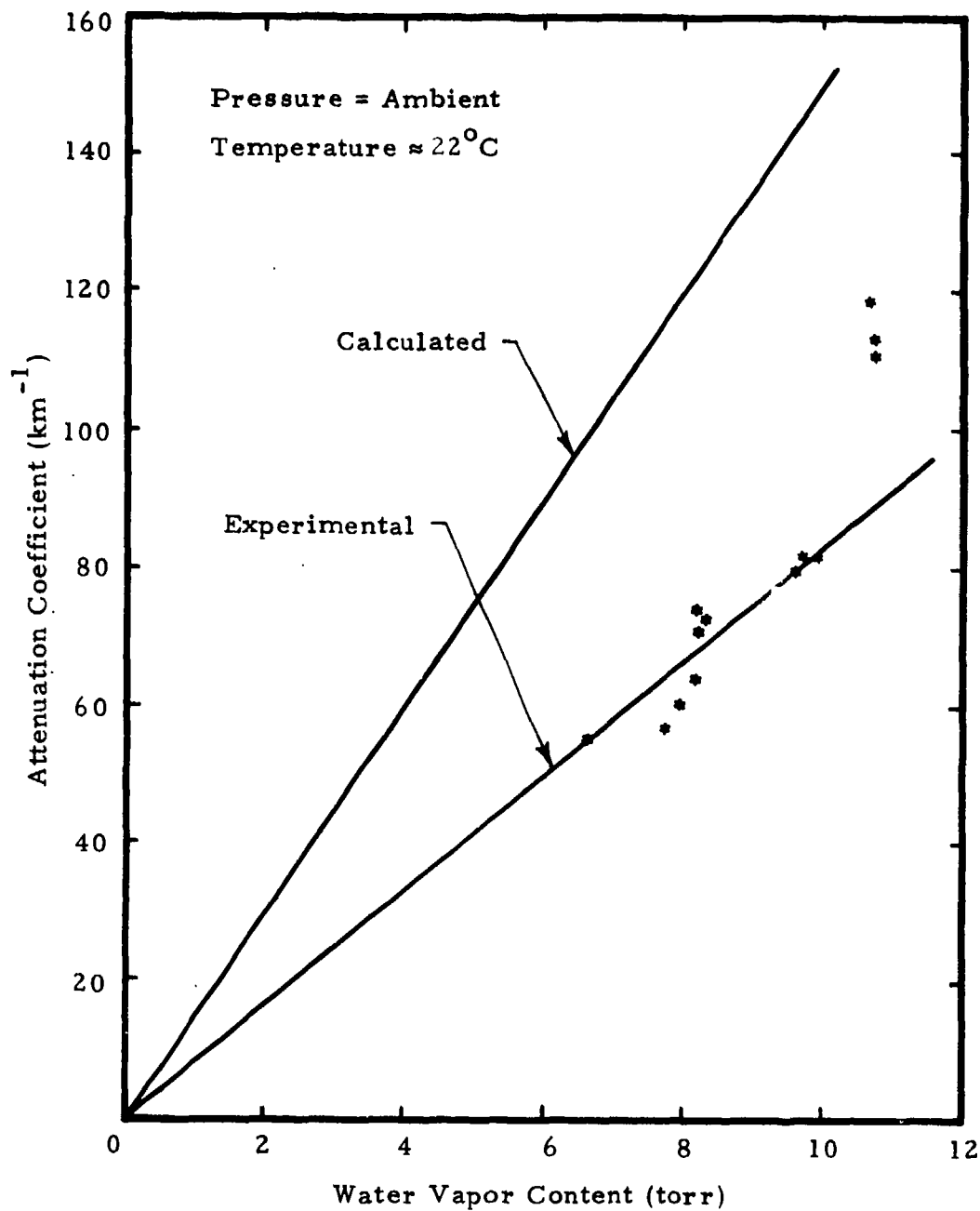10-9P(11) $[1866.735 \text{ cm}^{-1}]$ CO Laser Line vs Water Vapor Content (U)

(U)   Figure 4.13. Atmospheric Attenuation Coefficient of
11-10P(10) $[1845.130 \text{ cm}^{-1}]$ CO Laser Line vs Water Vapor Content (U)

(U)　Figure 4.14. Atmospheric Attenuation Coefficient of
11-10P(12) $[1837.423 \text{ cm}^{-1}]$ CO Laser Line vs Water Vapor Content (U)

56

Midlatitude, Subarctic, and Arctic models. A more significant approach is to consider the atmospheric attenuation as a function of absorber concentration. For CO laser radiation the only significant absorber is water vapor. CO_2 laser radiation is absorbed by water vapor and CO_2. Figure 4.15 gives the absorption coefficients for the P(20) CO_2 laser line and the 5-4 P(15) and P(16) CO laser lines as a function of water vapor content (760 torr of N_2). The two CO lines were the only "good" lines measured by Long.[5] The curves (measured) for these lines are obtained from a quadratic fit to Long's experimental data. The dotted lines are the predicted values using the theoretical model (Long's, McClatchey's, and our calculations give identical results). The shape of the CO_2 curves results from a quadratic fit to experimental data.[9] The three curves for the P(20) CO_2 line represent different concentrations of CO_2 in the atmosphere. The effect of CO_2 absorption results from theoretical calculations[10] and confirmed by experimental results.[9] The concentration of CO_2 in a standard atmosphere at sea level is 330 ppm.[9] The upper CO_2 curve of the figure illustrates a worst case situation corresponding to nocturnal concentrations of CO_2 near vegetation.[9]

(U)   The scales at the bottom of Figure 4.15 correspond to four of the atmospheric models giving the correlation of altitude to water vapor content.[11] This illustrates the unrealistic use of the sea level Midlatitude Winter Model in atmospheric transmittance discussions.[*] As can be seen from the figure, this model corresponds to a water vapor content of ~3.3 torr. At this point the attenuations of the P(20) CO_2 line and the 5-4 P(15) and (16) CO lines are the same[**] while at higher water vapor pressures, the two CO laser lines are more highly absorbed than the CO_2 line. This indicates that for most

---

(U) [*] Note for example that the data for Figures 4.10 and 4.14 taken over a period of a week shows an average water vapor content of the atmosphere in Hawthorne, California, of ~9 torr.

(U) [**] The actual measured values for the CO lines fall below the fitted curve at this water vapor content giving them an approximate factor of two advantage over CO_2 -- but only at this point.
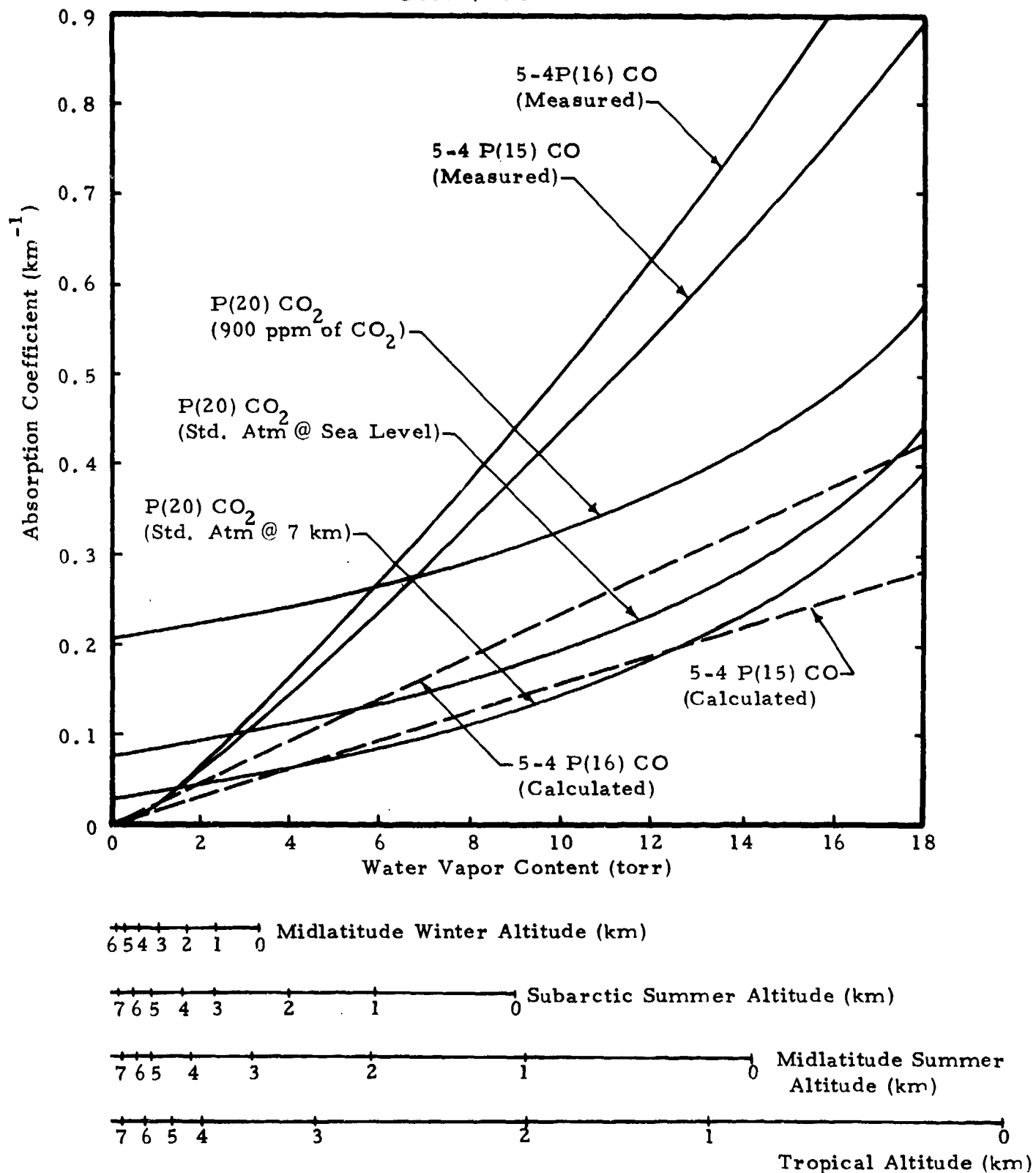
(U) Figure 4.15. Atmospheric Absorption Coefficient for
CO_2 P(20) and CO 5-4P(15) and P(16) Laser Lines. (U)

58

low altitude situations, the P(20) CO_2 laser radiation appears to have less atmospheric absorptive loss than the 5-4 P(15) and (16) CO laser lines. However, at altitudes of 5 km or higher (regardless of the Model atmosphere), the CO lines would have less attenuation than the CO_2 line. The water vapor content of the atmosphere decreases much more rapidly with altitude than does the CO_2 content.

(U)   The results for the 5-4 P(15) and P(16) lines cannot simply be extrapolated to the other "good" lines and thus, until actual measurements are made for these other lines, the theoretical predictions should be used -- but with caution. Figure 4.16 shows a comparison of the theoretical absorption coefficients for these lines and the CO_2 P(20) line.

4.3   (U) <u>Empirical Model for High Pressure Water Vapor Loss</u>. As indicated in Section 4.2, the theoretical model is not adequate for predicting the monochromatic loss due to water vapor absorption. It is desirable to have the capability for reasonable prediction of the intracavity losses introduced by various water vapor and additive broadening gas pressures for use in the CO laser kinetic code. Therefore during this period an empirical model was constructed using the experimental data taken to date.

(U)   Since most of the absorption data has been for a vapor cell temperature of $150^{\circ}C$, the primary variable has been pressure, either water vapor or additive gas pressure. The experimental absorption coefficient for approximately ten CO laser lines from various vibrational bands was plotted versus water vapor pressure (no additive gases) on a log-log scale. In addition the absorption coefficient as calculated using the currently accepted theoretical model was plotted on the same figure. The average slope for the experimental data was 2.5 while the average slope for the calculated values was 2.0. The value of 2.0 is obvious from the theoretical model. Since most of the CO laser frequencies used lie in the wings of water vapor absorption lines, the

59
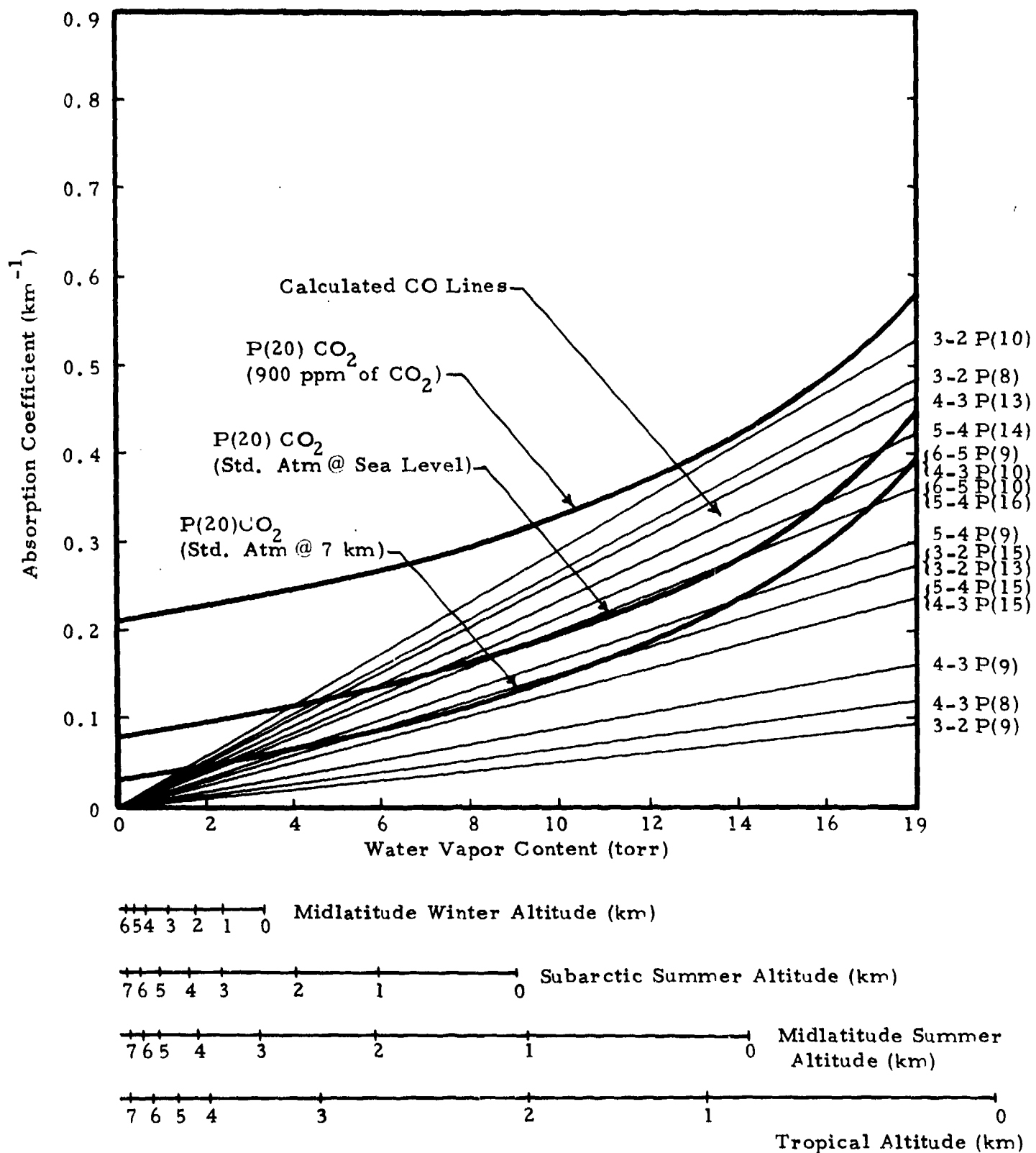
(U) Figure 4.16. Atmospheric Absorption Coefficient
for CO_2 P(20) and Selected CO Laser Lines (U)

60

absorption coefficient is directly proportional to the half-width of the water vapor line which, according to the model, varies directly with the pressure. In addition the absorber thickness also varies directly with the water vapor pressure, and thus, according to the theoretical model, the absorption coefficient should vary as the square of the water vapor pressure. The experimental data indicates otherwise. Although a physical explanation is not apparent, it appears prudent to modify the theoretical model to obtain an empirical one which will reasonably fit the experimental results. It may be that at the pressures involved in this investigation, ordinary two-body type collision theory may not apply which may explain the anomolous pressure dependence.

(U)   The details of the theoretical model may be found in an earlier report.[2] However, the pressure dependence of the half-width of the water vapor lines was seen to be given by

$$\alpha \sim 5.49P \ (H_2O) \tag{4.1}$$

where 5.49 is the self-broadening coefficient of H_2O. Since the relationship of absorber thickness to water vapor content should not change, the pressure dependence of the half-width for the empirical model is altered to the 1.5 power. The self-broadening coefficient of 5.49 is therefore no longer applicable and through several iterative steps a self-broadening coefficient of 0.56 was found to give the best fit to the experimental data. Thus the half-width of the water vapor lines of the empirical model varies as

$$\alpha \sim 0.56P^{1.5} \ (H_2O) \tag{4.2}$$

Figure 4.17 shows the results of this effort for one of the typical CO laser lines. The absorption coefficient for the 10-9 P(8) line is shown as a function of water vapor pressure. The more reasonable agreement of calculated values by the empirical model with the experimental data is obvious.

61
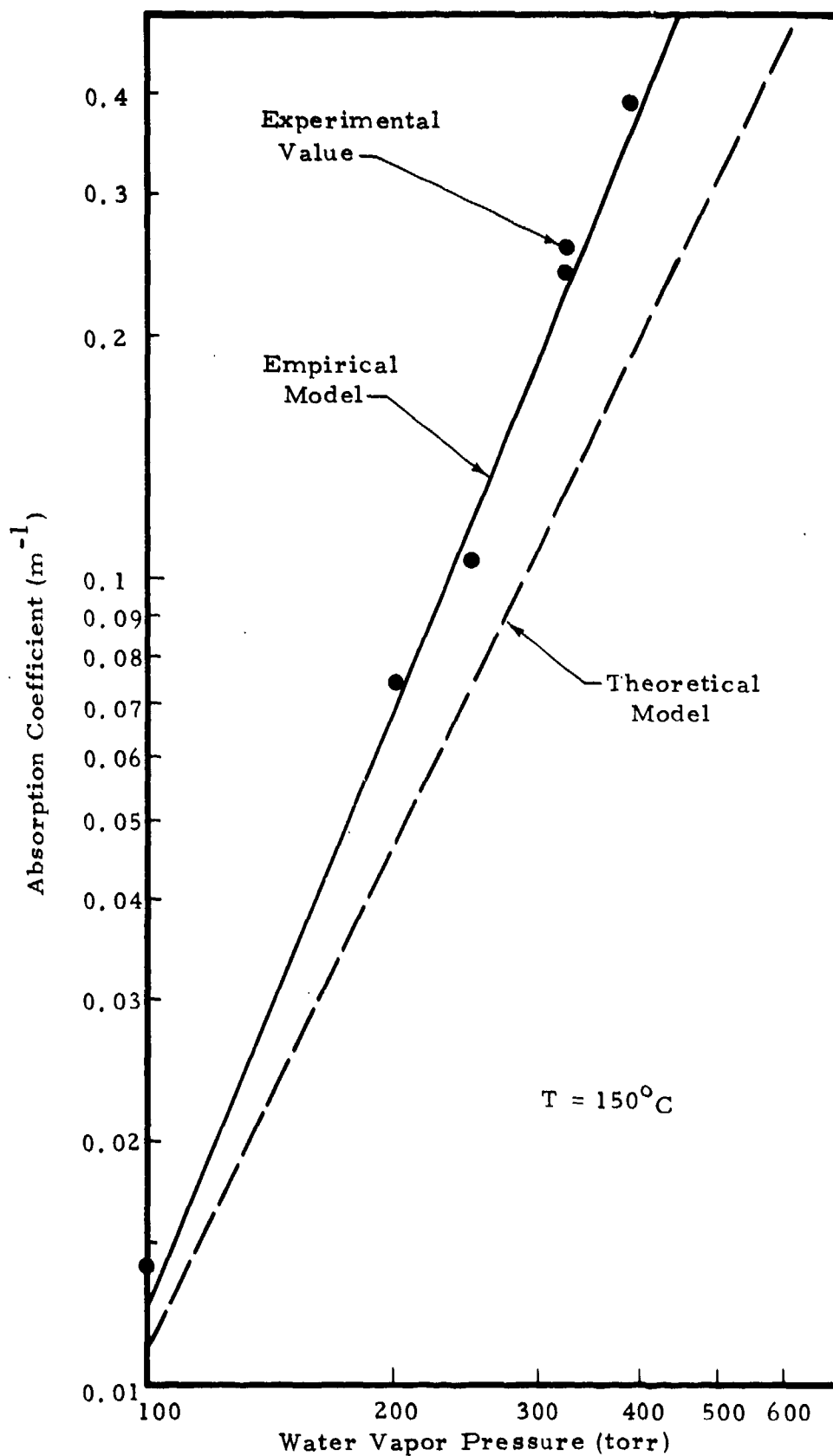
(U) Figure 4.17. Absorption Coefficient of 10-9P(8)
CO Laser Line vs Water Vapor Pressure (U)

UNCLASSIFIED

(U)   A similar procedure was followed to establish an empirical relation-
ship for the broadening effect of N_2 and CO_2. For these gases the water
vapor half-width dependence on pressure could be defined as linear. However,
the broadening coefficients had to be modified from the existing theory. The
theoretical values of these coefficients were 1.0 for N_2 and 1.5 for CO_2; the
modified values for the current empirical model are now 1.6 for N_2 and 3.0
for CO_2. Figures 4.18 and 4.19 show the results of these modifications for
the 10-9 P(7) laser line for a water vapor content of 200 torr and a temperature
of $150^{\circ}C$.
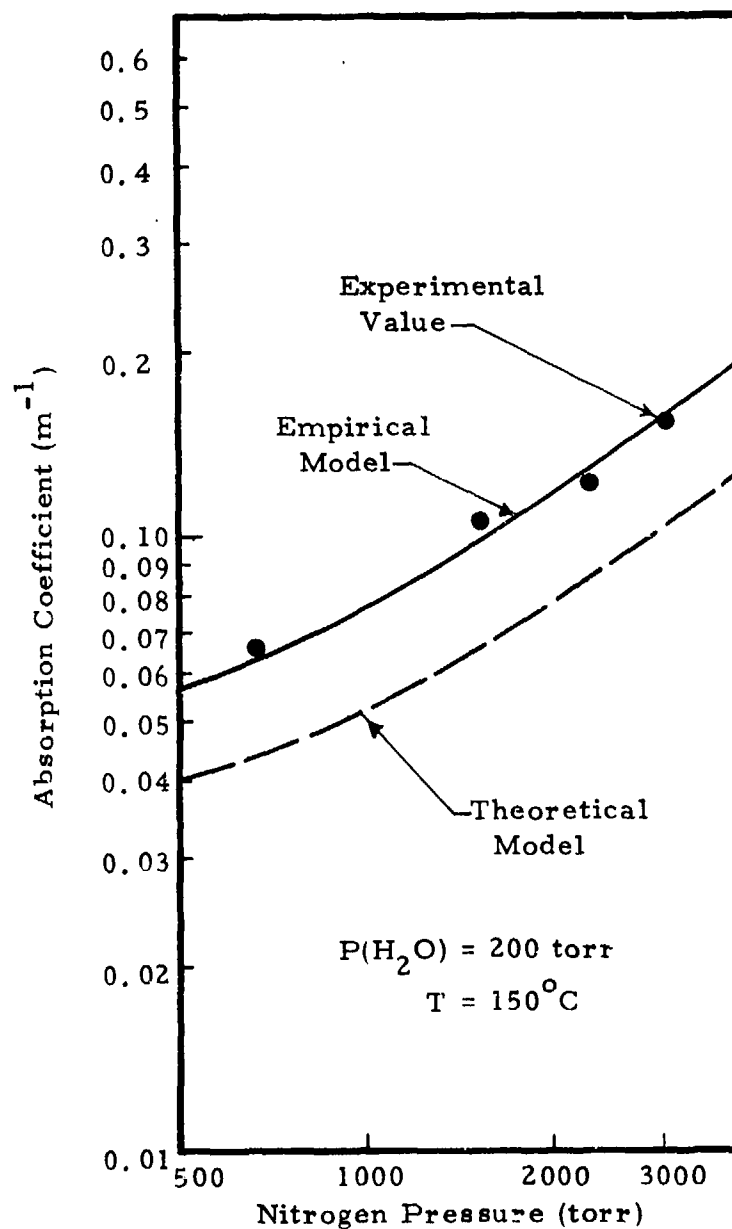
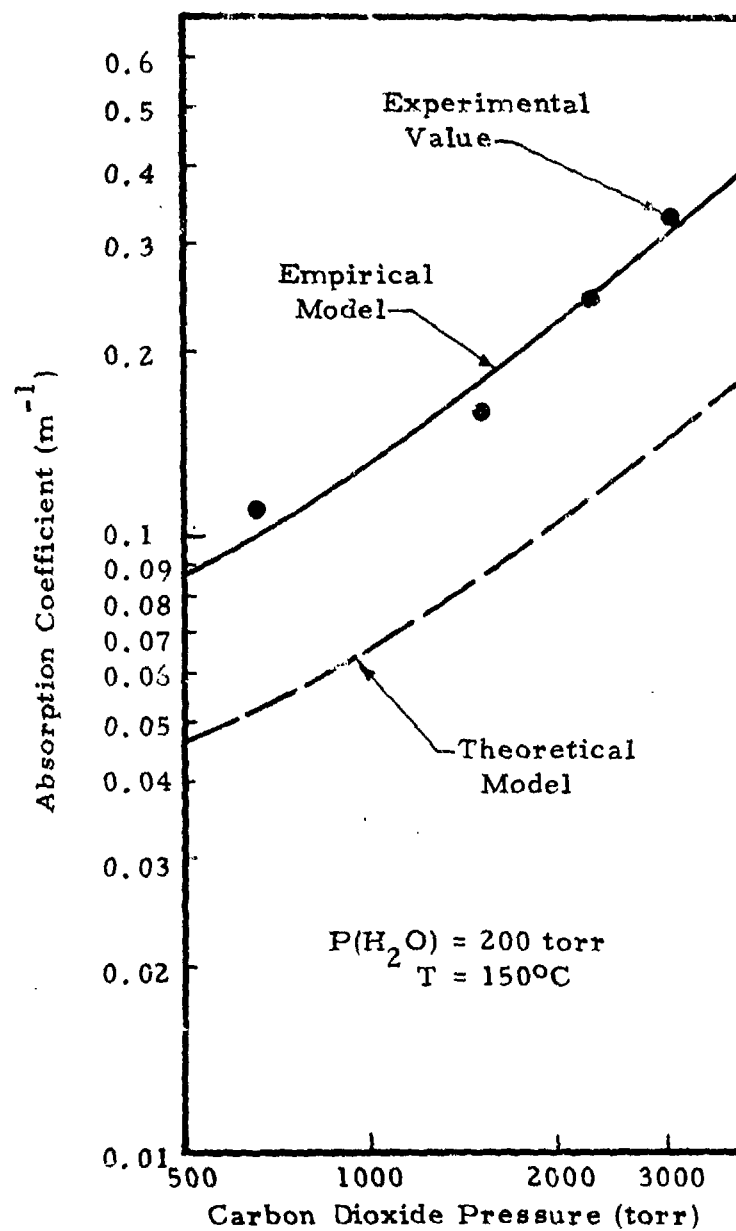(U) Figure 4.18. Absorption Coefficient of 10-9P(7)
CO Laser Line vs Nitrogen Pressure (U)

(J) Figure 4.19. Absorption Coefficient of 10-9P(7)
CO Laser Line vs Carbon Dioxide Pressure (U)

5.0   PARAMETRIC DEPENDENCE OF THERMAL BLOOMING

(U)   Empirical expressions for thermal blooming calculations have been derived by Lincoln Laboratories[12, 13] from computer calculations carried out there. These expressions provide a convenient analytical tool to predict relative target intensities for various laser system parameters and atmospheric attenuation coefficients. Using these expressions, the dependence of intensity on target to laser power was investigated for various wavelengths, atmospheric attenuation coefficients and aperture diameters. An attempt was also made to approximate the effects of atmospheric turbulence on target intensity.

(U)   The investigation is limited to three wavelengths in the infrared ($\lambda_1 = 10\,\mu m$, $\lambda_2 = 5\,\mu m$, $\lambda_3 = 3.3\,\mu m$), with the parameters normalized to the $10\,\mu m$ wavelength laser.

5.1   (U) The Empirical Expressions for Thermal Blooming. The results of numerical analyses at Lincoln Laboratories[12] yield the following empirical relationships.

(U)   The intensity on target is approximated by

$$I \cong (P/A_o) \exp(-P/P_c) \qquad\qquad (5.1)$$

where P is the laser power, A_o is the area of the focal spot at range R, and P_c is the power at which the beam intensity at the target saturates. The latter is empirically shown to be

$$P_c = \left[(15\omega D)/(\alpha k C)\right] \, f(s, \, \omega R/v_o). \qquad (5.2)$$

In this expression, D is the aperture diameter, α is the absorption coefficient in the propagation path, k is the wave number, C is an

atmospheric constant related to specific heat and density, and f is a function depending on the beam shape s, the slewing rate ω, and the wind velocity v_o.

(U)   Substituting (5.2) into (5.1) and solving for peak intensity, with $A_o \cong (R\lambda/D)^2$, one obtains

$$I_{pmax} = [(\omega D^3)/(\alpha C \lambda R^2)] \, f(s, \omega R/v_o) \qquad (5.3)$$

If αR is not $\ll 1$, one should multiply (1) and (3) by the factor $\exp(-\alpha R/2)$. The above expressions hold for aperture diameters very much smaller than the coherence diameter.

5.2   (U) <u>Wavelength and Attenuation Coefficient Dependence.</u> It is well known that for a given aperture, the beam intensity at the focal region is inversely proportional to the square of the wavelength (λ^{-2}) if absorption and turbulence is negligible. Or, for a required intensity at the target, the required laser power is directly proportional to λ^2. Using the empirical expressions for thermal blooming, it can be shown that for a given intensity on target the proportionality of the laser power could have a wavelength dependence as high as λ^3. This characteristic is depicted in Figure 5.1 by the normalized plots of Equation 5.1. In these plots all parameters have been kept constant for the three wavelengths with the 10 μm laser used for the normalization. The effects of turbulence and pointing jitter have not been taken into account.

(U) It can be seen from this figure that the intensity peak for the longest wavelength requires the highest laser power. The shorter wavelength peak intensities are higher and are inversely proportional to λ (note that α is assumed the same for all three cases). A more significant point of this plot, for applications where size and weight of devices are critical, is the decrease in the required laser power by an order of magnitude for the shorter wavelengths. For these cases, the curves are approximately

linear in the regions of interest where small variations in absorption coefficients from the assumed value are not significant.

(U) Figure 5.2 shows the effect of variations in absorption coefficient where the range of the required laser power is still λ^2 to λ^3 dependent. The available peak intensity increases with decreasing α and the corresponding laser power varies in proportion to λ^2.

(U) The above comparisons are not adequate when scattering, atmospheric turbulence, beam wander and pointing jitter are taken into account. They are all factors that are wavelength dependent and, while generally considered linear effects, could influence the beam spread due to thermal blooming. In the next section an approximation is used as an attempt to include the effects of atmospheric turbulence in the calculation of intensity with the thermal blooming expressions referred to above.

5.3   (U) <u>Effects of Atmospheric Turbulence.</u>   Analytical calculations of the spread of a focused laser beam in a turbulent atmosphere have been made by several authors.[14, 15] These calculations are made for low intensities and are statistical averages based on statistical models of the atmosphere. Assuming that these analyses are adequate for a linear calculation and the statistical averages are acceptable for estimates of intensity bounds, we can introduce the effects of turbulence in the expression of Equation 5.1 as an approximation for comparison between the three wavelength lasers.

(U) The results of the referenced analyses show that the average   focal spot area may be expressed by

$$A_o^* \cong (\lambda R/D)^2 \left[1 + (\beta D/\lambda)^2\right] \qquad (5.4)$$
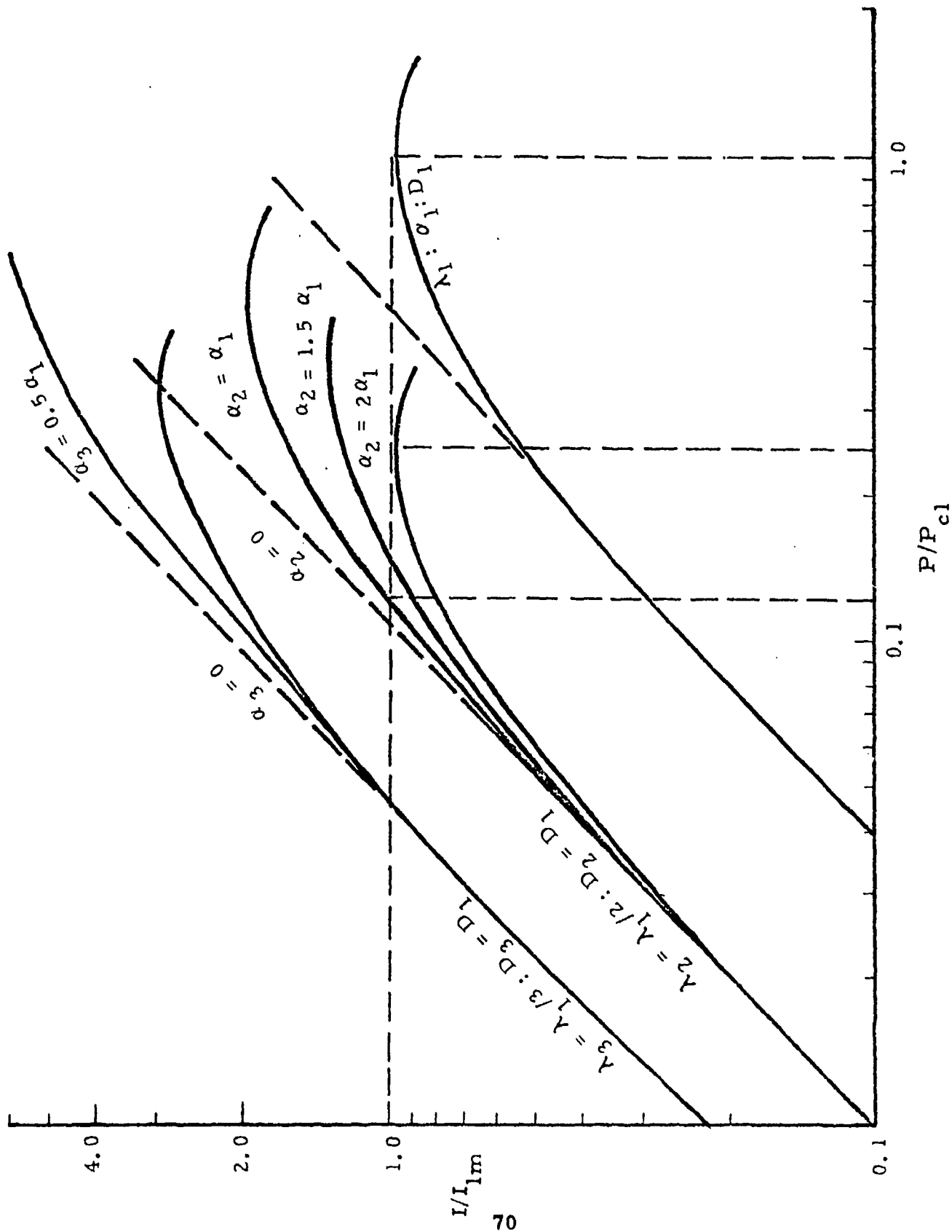
(U) Figure 5.2. Normalized Intensity vs Laser Power Absorption Coefficient Dependence of Thermal Blooming (U)

where $\beta^2 = 52 \, R \, \kappa_m^{1/3} \, C_n^2$, with C_n^2 the atmospheric-turbulence strength parameter and κ_m the wave number of the turbulence microscale.

(U) The coherence diameter, D_c, is defined by

$$\beta D_c / \lambda = 1. \tag{5.5}$$

This means that for a given wavelength, increasing the aperture diameter above D_c will not increase the intensity on the target, and that the coherence diameter scales linearly with wavelength.

(U) The first comparison that may be made of wavelength dependence of thermal blooming with turbulence is for cases where D/λ is kept constant. The intensity on target may be calculated from Equation 5.1 by using A_o^* instead of A_o. (It is not clear how the corrections for turbulence should be made in the exponent of Equation 5.1.) The normalized plots of Figure 5.3 show this comparison with the previous long wavelength case as reference for the normalization. For these cases, the required laser power for a given intensity on target is independent of wavelength in the linear region. In the nonlinear region, however, the deviation of required laser power favors the longer wavelength by a maximum of 2.3, which is not wavelength dependent (D/λ is kept constant). In addition, the achievable peak intensity is λ^2 dependent provided the laser power is increased in proportion (α is kept constant). The peak intensities will increase with decreasing α approaching the dotted line which is the diffraction limit.

(U) Another method of scaling this case would be to allow the aperture sizes to be equal by increasing the number of apertures inversely with λ^2. For example, the $10\,\mu m$ wavelength case would have one aperture with diameter $2D_1$, the $5\,\mu m$ wavelength would have four apertures with diameters D_1, and the $3.3\,\mu m$ wavelength would have nine apertures with diameters $0.7D_1$.

71
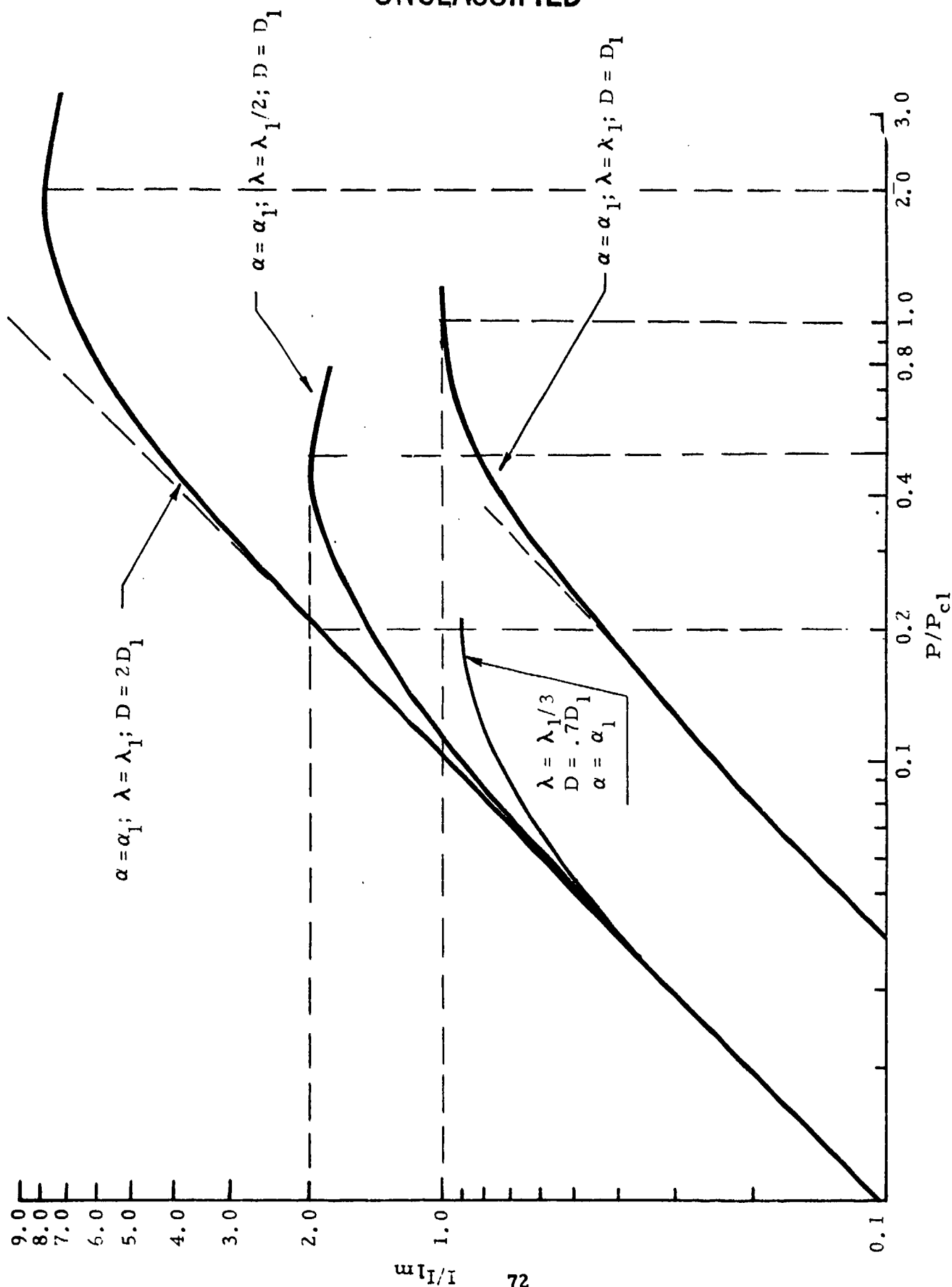
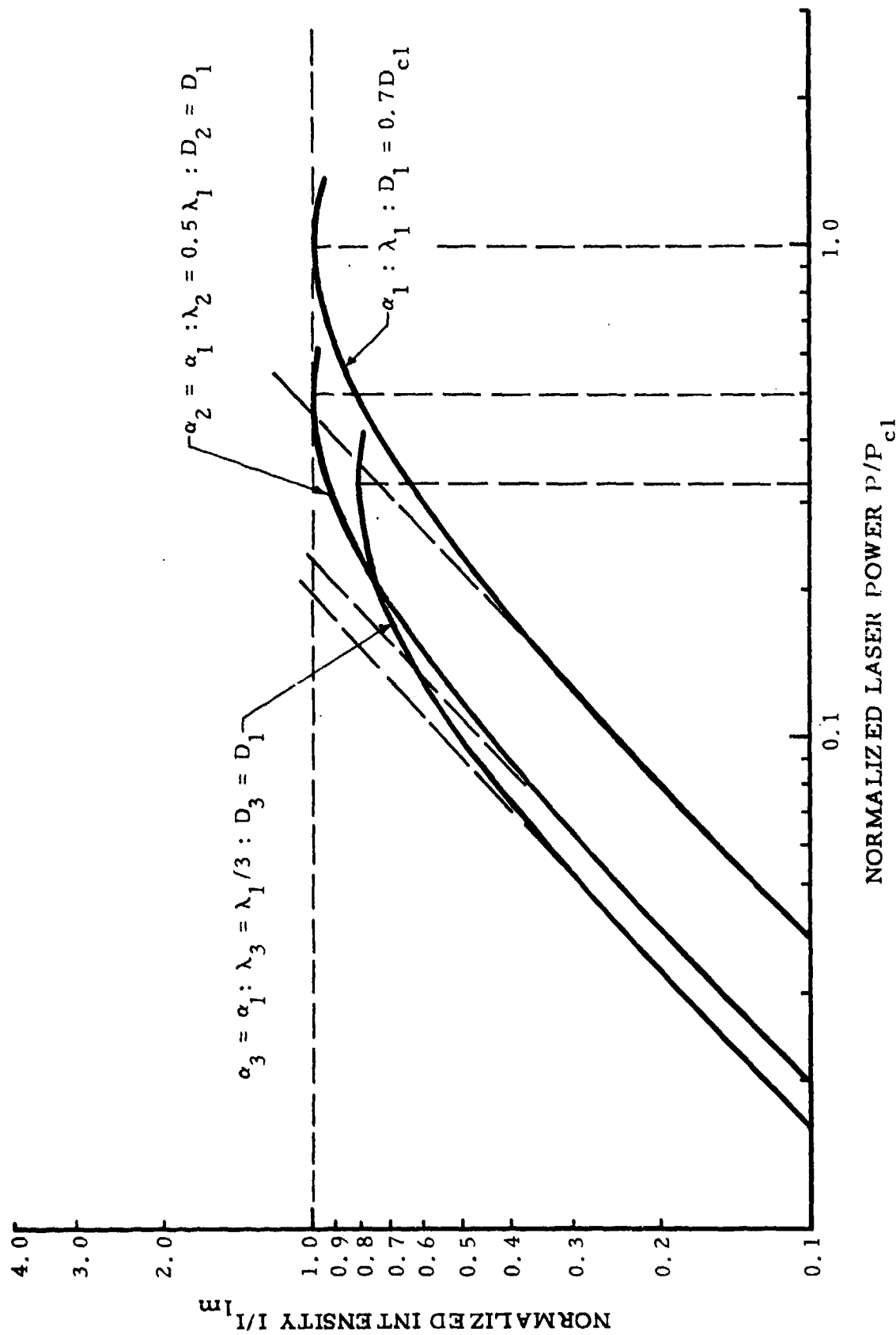(U) *Figure 5.3.* *Normalized Intensity vs Laser Power Aperture and Wavelength Dependence of Thermal Blooming (U)*

For each wavelength, the total transmitted laser power would be equal with the transmitted beams adding incoherently at the target. In this limit the three wavelength curves will be coincident in the entire range of intensity vs laser power. We suggest that this should be the worst case for a calculation of thermal blooming with turbulence when the apertures are large and have the same physical diameter.

(U) A more realistic comparison for fixed apertures may be made by assuming again that A_o in the expression of Equation 5.1 can be replaced by A_o^*. We take a fixed physical diameter for the three wavelengths to be $0.7 D_{c1}$, where D_{c1} is the coherence diameter of the longest wavelength λ_1. This yields the plots of Figure 5.4, where the normalization is again based on the parameters of the longest wavelength laser. These results show that, for a given intensity on target, the required laser power is directly proportional to λ in the linear region and the same relationship holds in the nonlinear region as well; provided the α's are approximately the same. The shortest wavelength has a slightly lower intensity peak (~0.8) at the normalized laser power of 0.33. The peak intensities will increase with decreasing α (it scales with λ/α), approaching the linear limit shown by the dotted lines. Calculations with larger diameters will tend to approach the results of Figure 5.3. However, as discussed in the previous paragraph, the worst limiting case appears to be coincident curves.

(U) In the above comparisons, the effects of thermal blooming were approximated from the linear analysis and statistical averages of intensity due to turbulence and the empirical results of Equation 5.1. In reality, it is necessary to consider time dependent scattering of turbulence and its effect on the nonlinear phenomenon of blooming, which is certainly a difficult task to perform analytically. Realistic conclusions can only be made after

73

NORMALIZED LASER POWER P/P_{cl}

NORMALIZED INTENSITY I/I_{lm}

$\alpha_2 = \alpha_1 : \lambda_2 = 0.5\lambda_1 : D_2 = D_1$

$\alpha_1 : \lambda_1 : D_1 = 0.7D_{cl}$

$\alpha_3 = \alpha_1 : \lambda_3 = \lambda_1/3 : D_3 = D_1$

(U) Figure 5.4. Normalized Intensity vs Laser Power Approximated Effects of Turbulence and Blooming (U)

74

experimental measurements of atmospheric propagation, at high intensity levels, with high power lasers at various wavelengths and atmospheric conditions. However, the conclusions of the approximations made here indicate that a given intensity on target may be achieved with less laser power at shorter wavelengths. The proportionality of this laser power to wavelength appears to be in the range between λ to λ^3, assuming all other parameters to be constant.

6.0 MODE CONTROL AND RESONATOR DESIGN

(U)   During the last period the theoretical mode program described in previous reports has been extended to investigate the modes of resonators with mirrors having reflectivities which are functions of the radius. It has been found that the mode structure can be greatly improved by eliminating the diffractive wave which results from the sharp edges of the mirrors in a typical unstable resonator. A theory has been derived and the results enable one to design a resonator system to accomplish this. A new computer code based on the Prony method described by Siegman and Miller[16] has been written and utilized to investigate the behavior of all the dominant modes for variable reflectivity mirrors.

(U)   The radiated wave from an aperture (or a mirror) can be written as the sum of a geometrical optics wave plus a diffracted wave which can be described by a line integral around the aperture boundary.[17] If the diffracted wave scattered from a resonator mirror edge back into the resonator axis can be minimized or eliminated then the mode structure will become similar to the geometrical optics mode. This is extremely desirable because the intensity profile is flat (which minimizes the mirror loading), the phase profile is smooth (which minimizes the divergence angle) and the mode discrimination ratio is large (which aides single-mode operation). Figures 6.1 and 6.2 respectively, are the intensity and phase profiles for three symmetric unstable resonators and illustrate the effects which can be accomplished by tapering the mirror reflectivity. The intensity profile of a sharp-edge resonator has an intense spike at the center then falls to a low value toward the edge. The second case illustrated is for a resonator with mirror reflectivities which are tapered linearly from a value of unity at $r/a = 0.8$ to zero at $r/a = 1$. This case is not expected to be optimum, but it can be seen that the relative intensity of the central spike has been reduced and the mode shape improved. The optimum case was expected
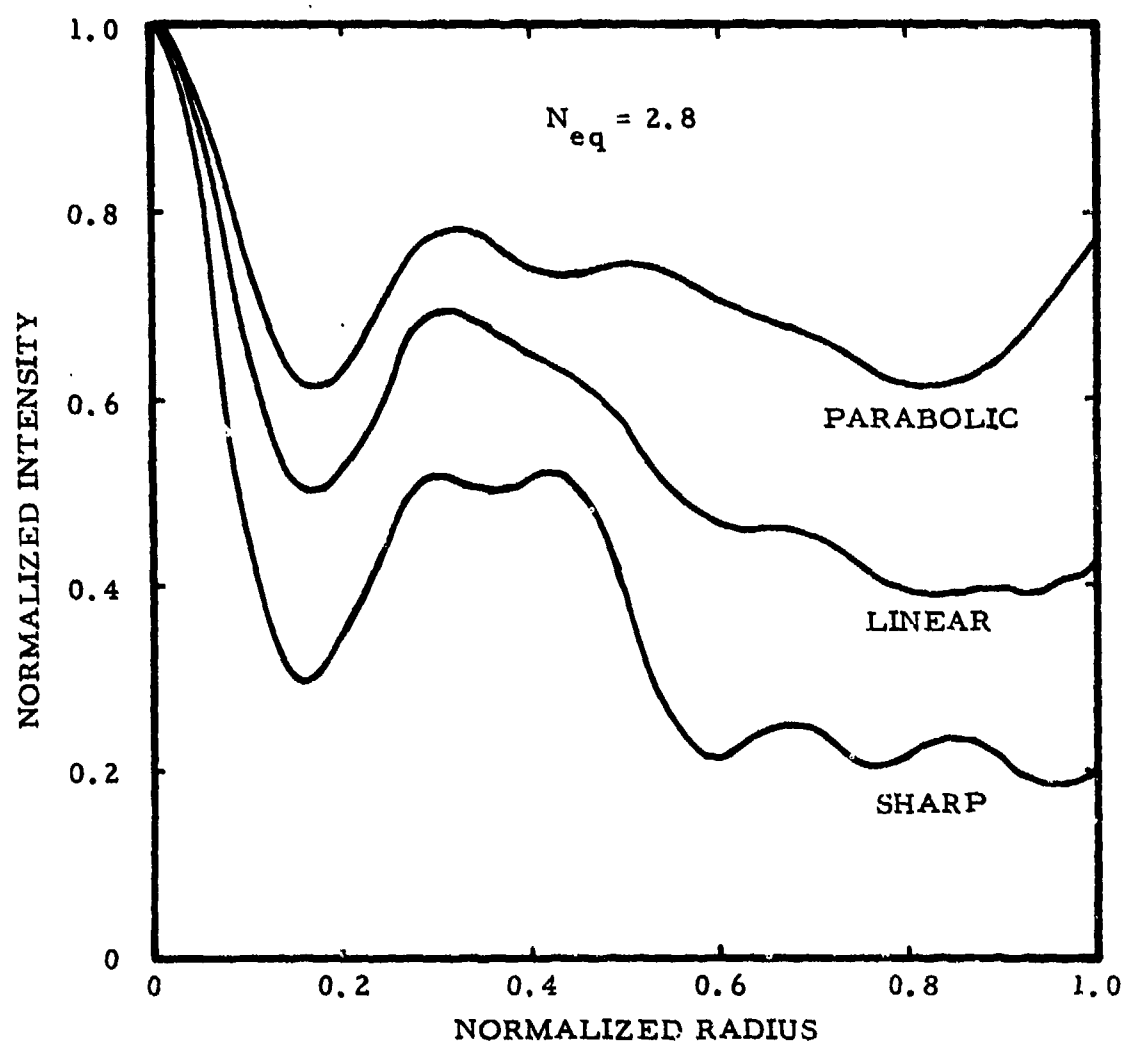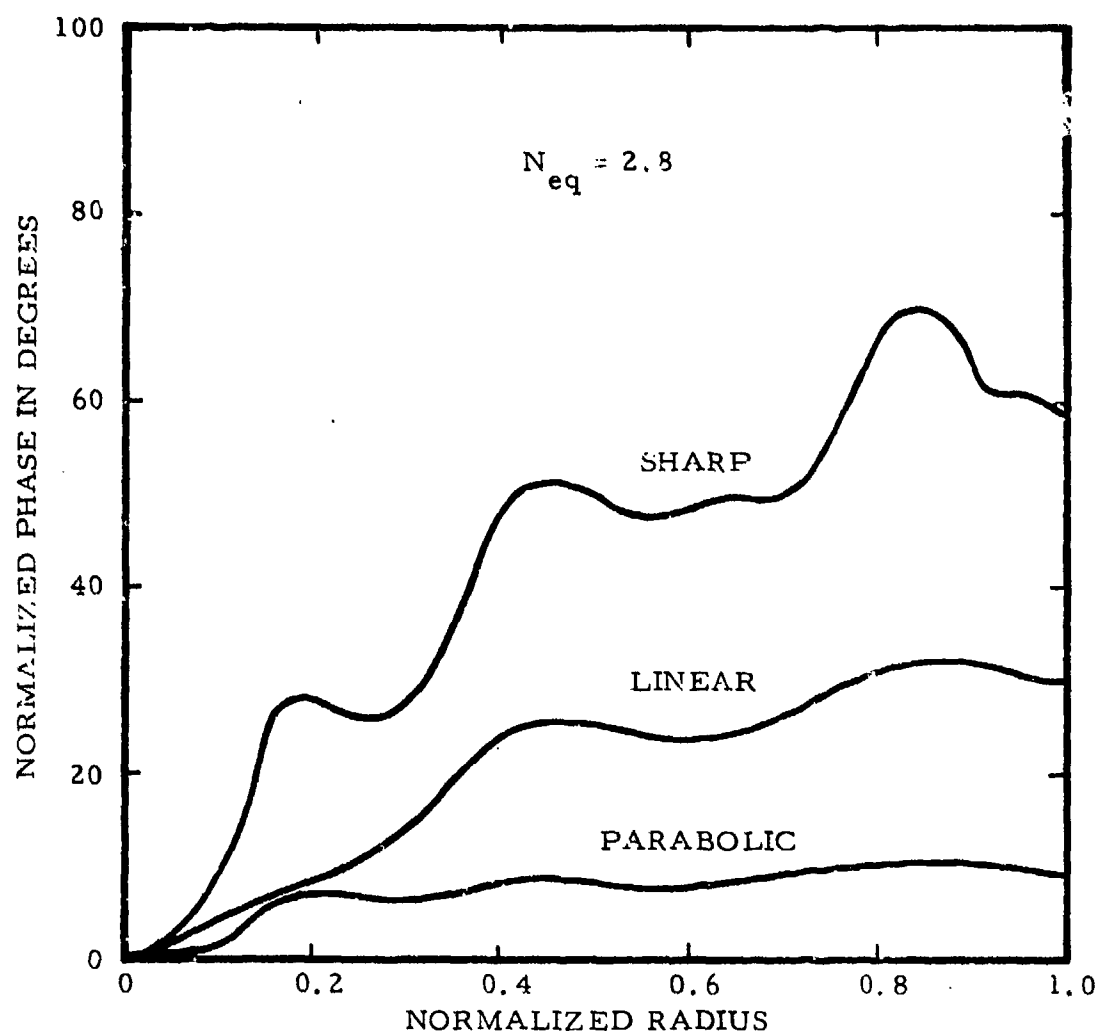
(U) Figure 6.1. Normalized Intensity Profiles for Three
Symmetric Unstable Resonators having
Different Edge Conditions. (U)

(U) Figure 6.2. Phase Profiles (Normalized to the Geometrical
Optics Phase) for Three Symmetric Unstable
Resonators having Different Edge Conditions (U)

78

to be a parabolic taper from $r/a = 0.8$ to $r/a = 1$ and this results in a nearly flat profile. The phase profiles (normalized to the geometrical optics phase) shown in Figure 6.2 are even more striking. The sharp-edge resonator displays nearly $\lambda/4$ variation across the mirror while the variation for the parabolic taper is negligible beyond $r/a = 0.1$.

(U)   The diffraction contribution at the resonator focus can be expressed as the following integral,

$$I = K \int_{o}^{1} (dU/dR) \exp(-i\, 2\pi N_{eq} R^2)\, dR,$$

where

$$K \quad = \quad \text{constant}$$
$$U \quad = \quad \text{field amplitude}$$
$$N_{eq} = \quad \text{equivalent Fresnel number}$$
$$R \quad = \quad \text{normalized radius}$$

This integral expression is important for two reasons. Firstly, the equivalent Fresnel number comes in naturally in the phase factor and the rather curious dependence of the modes on this parameter becomes more clear. Secondly, we have an analytical expression for evaluating the quality of the mode expected for a given reflectivity. For example, if we choose an amplitude reflectivity which varies as R^2 and we assume that U follows this variation, then the integral will go identically to zero each time the phase factor changes by 2π. Thus the point where the taper is initiated can be chosen so that this integral is zero and the diffractive effects in the mode profile are minimized. This is the case illustrated by the parabolic taper in Figures 6.1 and 6.2.

(U)   Numerous calculations have verified that the fundamental mode losses do indeed approach the geometrical optics value with a periodicity

described by the integral. Similar results have been achieved where dU/dR has been varied by introducing a phase shift which is a function of position. This would correspond to the physical case where the mirror edges are rolled off. The same results should be obtainable by properly designing the shape of a sharp-edge mirror so that the diffractive contributions from the edge suffer destructive interference. In fact, this would seem to be the most practical method of obtaining the desired results, because the tolerances are less critical and it is mechanically easy to do.

7.0   AREA CATHODE E-GUN DEVELOPMENT

(U)   The area cathode E-gun system has been completely assembled for performance testing and evacuation. Included in the entire E-gun system are the vacuum tank, which contain the cathode, control grid and electron window components, the bias power supplies, the control electronics, and the shielded test facility.

7.1 (U) Component Description. These various components of the E-gun are illustrated in Figure 7.1, 7.2 and 7.3. Figure 7.1 is a photograph of the vacuum envelope which is of all stainless steel fabrication with copper gasketed flanges, except for the window which is sealed with a Viton "O"-ring. The view of the E-gun in Figure 7.1 illustrates the 14" i.d. service flanges at each end of the gun, the support ceramic penetrations along the top, the SF_6-filled high voltage cable termination chamber, and the 500 ℓ/sec vac ion pump.

(U)   Figure 7.2 is a photograph of the interior of the E-gun. In the center is the heat shielded area cathode which is electrically isolated from the control grid-shroud structure by alumina insulators. The high voltage shroud, containing the control grids and the cathode, is isolated from the vacuum envelope, or anode, by the support ceramics coming in diagonally at the top of Figure 7.2. The ladder which supports the 1 mil titanium foil window can be seen at the bottom of Figure 7.2.

(U)   Figure 7.3 is a photograph of the charging power supply and the tank containing the capacitive energy storage, the crow bar, the isolation transformers, and the grid bias control electronics. The smaller of the two tanks in the photograph is the 250 kV 2mA charging power supply which supplies the E-gun bias. Within the larger tank on the right is the 10kJ of
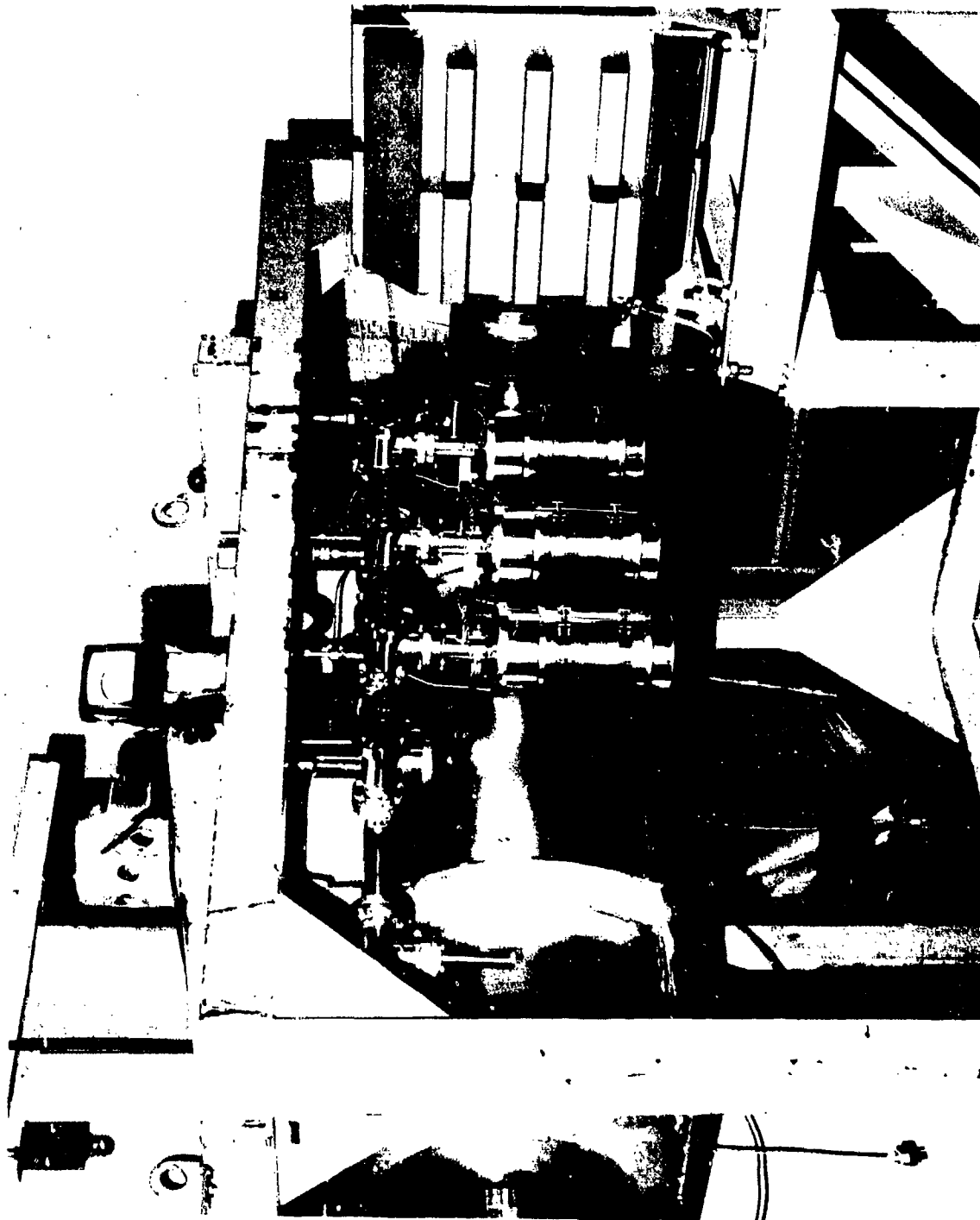
(U) Figure 7.1 10 cm x 100 cm Electron Gun (U)

82
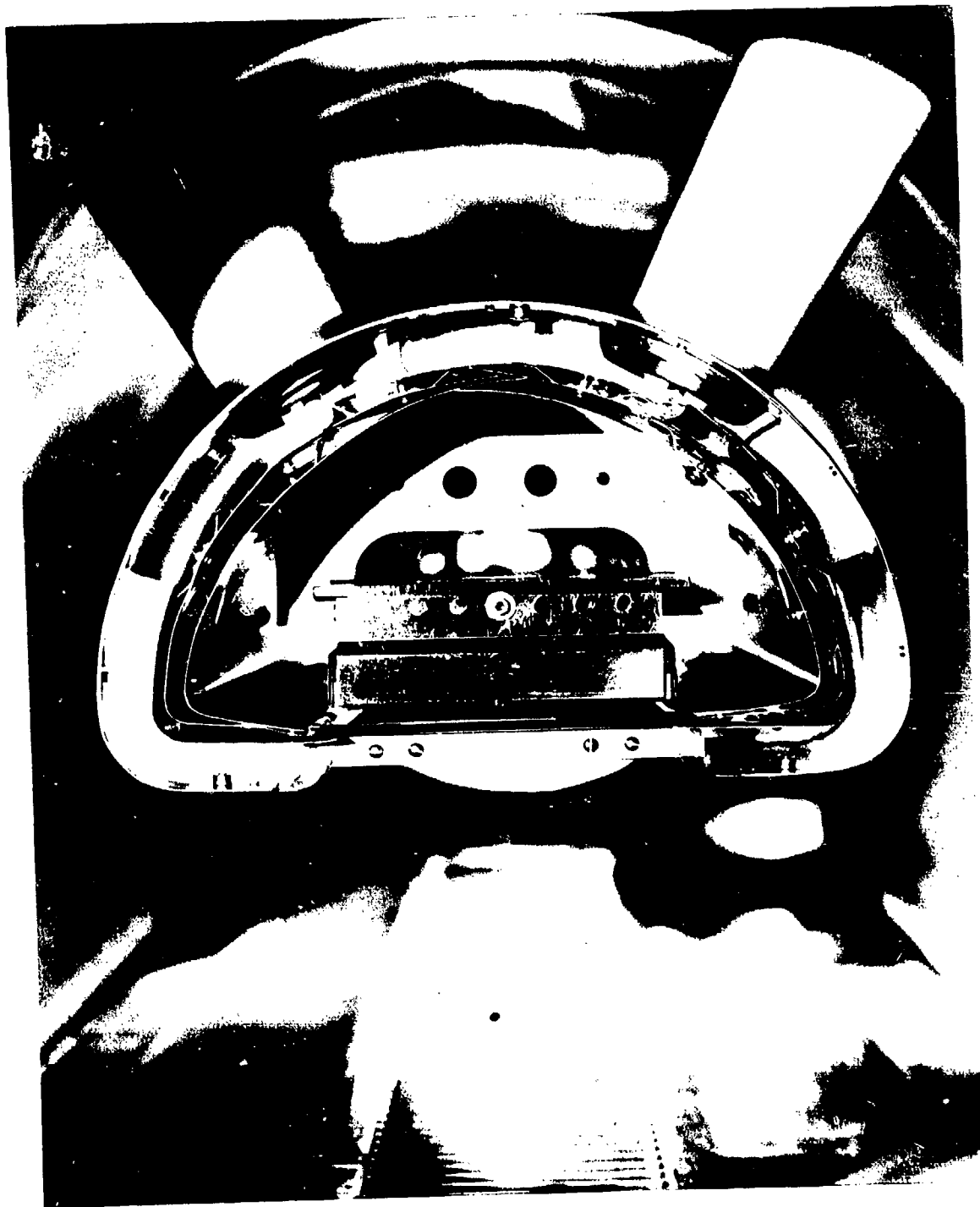
(U) Figure 7.2 Interior of 10 cm x 100 cm Electron Gun (U)

83
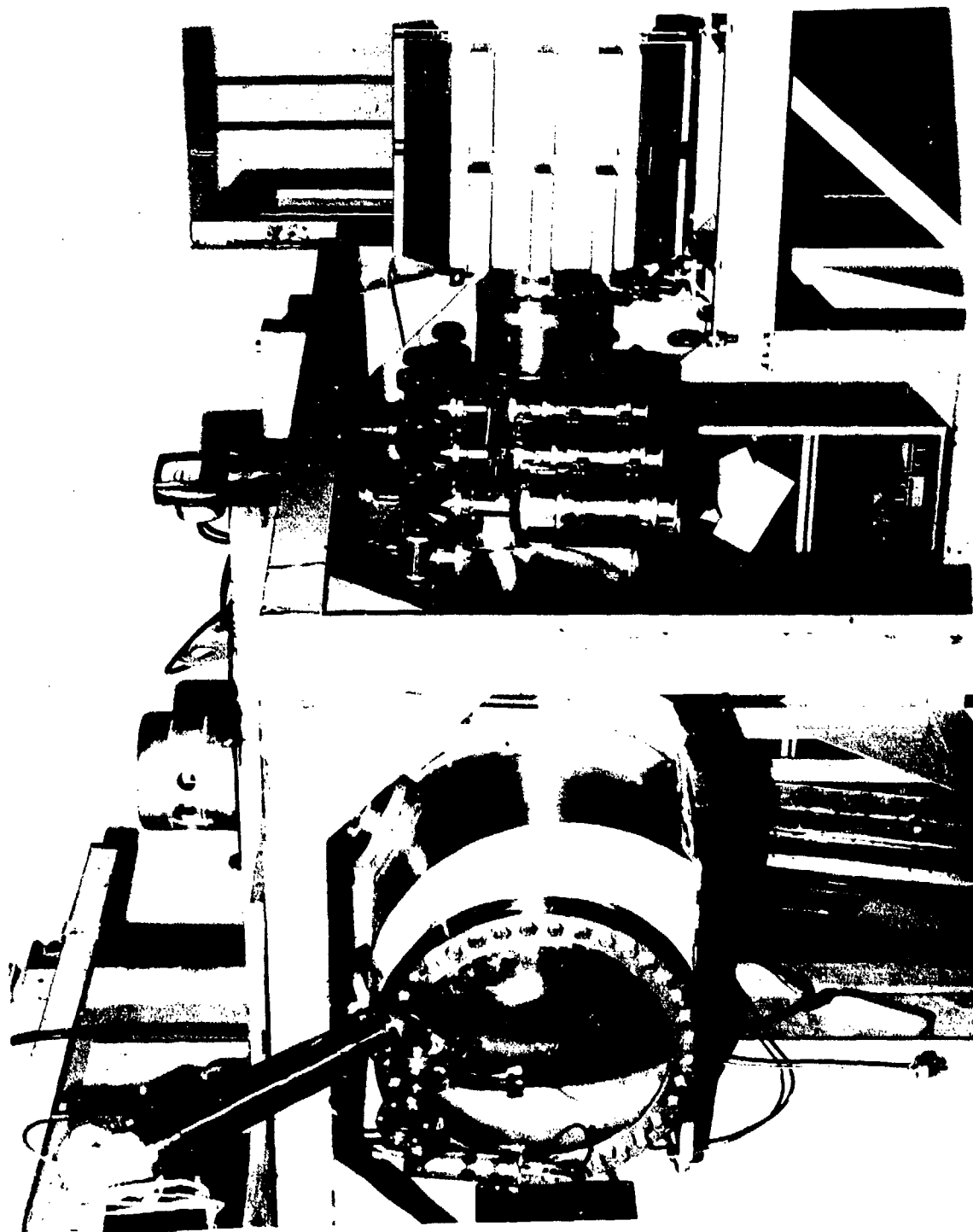
(U) Figure 7.3   10 cm x 100 cm Electron Gun   (U)

84

capacitive energy storage, the crow bar protection circuit which diverts
the stored energy in the event of a fault within the gun, the isolation trans-
formers which provide electrical power at the gun voltage, and the grid
control electronics. The E-gun bias voltage and the pulsed current density
and duration are controlled from rack mounted controls not seen in the
photograph.

7.2 (U) Vacuum Performance. The sorption and ion pumped E-gun vacuum
envelope has proven to be a clean, fast system. Sorption pumping the
system with a preliminary bakeout brings the pressure into the mid 10^{-4} torr
region where starting of the ion pump is easy. The ion pump readily pulls
the system into the 10^{-7} torr region without bakeout, and after bakeout via
cathode operation, the system base pressure is 1×10^{-8} torr.

(U)   The quality of the vacuum is not appreciably affected by the operation
of the cathode. For the current densities required, the cathode is operated
at a temperature of approximately 900°C which corresponds to a cathode
power input of approximately 4500W. The system pressure increased
from the low 10^{-8} torr region with the cathode cold to the mid 10^{-7} torr
region with the cathode hot. This performance assures a clean environ-
ment which does not poison the emission characteristics of the dispenser
cathode.

7.3 (U) E-Gun Performance. The E-gun has been tested for high voltage
standoff capability and pulsed current density. Before activation of the
cathode, the completely assembled E-gun was high voltage tested to
235 kV, at which voltage the high voltage feedthrough experienced tracking
over the surface of the ceramic on the SF_6 side.

(U)   Modifications have been made to the bushing which include removal of an unshielded ceramic skirt and the addition of a corona ring to shield the vacuum gasket joint. Tests by the component supplier have demonstrated a 300 kV capability, but conservative operation for the present design should not exceed approximately 200 kV. A more conservative 300 kV design is being evaluated at the present.

(U)   Following the high voltage tests, the cathode was activated and emission tests were performed at reduced voltage (50kV) and with the cathode at operating temperature (~900°C). Figure 7.4 illustrates typical pulsed currents as measured by a Pearson probe in the ground-return leg of the energy storage capacitors.

(U)   The maximum pulsed current measured was 80 A (Figure 7.4a) which corresponds to a current density of $80mA/cm^2$. This was temperature limited so that additional current was readily available by increasing the cathode temperature. Grid control of the pulsed current is illustrated in Figure 7.4b, where the pulsed current is varied by changing the amplitude of the grid pulsed voltage.

(U)   The shape of the pulsed current is a square wave with a rise time of less than 1μsec and a fall time on the order of a few μsec. The oscilloscope traces are distorted after approximately 50μsec because of the saturation of the Pearson probe. Figure 7.4c shows the trace of a low current pulse, which does not appreciably saturate the Pearson probe and illustrates the square wave pulsed current.

(U)   Operation of the area cathode E-gun at full rated voltage has experienced difficulty because of grid emission from the barium coated control
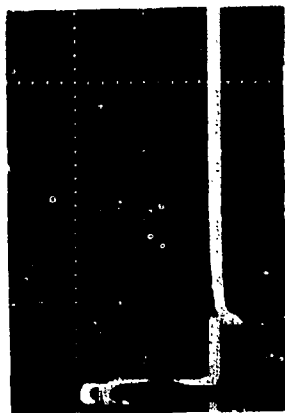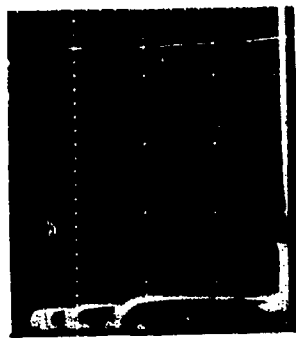
(U) Figure 7.4. Area Cathode Pulsed Current Performance (U)

87

grid wires. The grid wires were fabricated from tungsten because of its mechanical and thermal stability at the expected operating temperatures. For barium coated wires, this is not a suitable choice of material, so the grid wires are being coated with titanium to help reduce the grid emission problem.

(U)   In order not to delay laser tests, the area cathode assembly was replaced by a filamentary cathode assembly. The latter was constructed for the 10 x 100 cm gun for more than 100 mA/cm^2 output current operation. Tests of this gun are anticipated to be completed within two weeks.

8.0 (U) REFERENCES

1. D. K. Rice, "Absorption Measurements of Carbon Monoxide Laser Radiation by Water Vapor," AD 746-170 (July 1972).

2. D. K. Rice, "Carbon Monoxide Spectral Line Selection Studies," AD 749-823 (August 1972)

3. D. K. Rice, "Absorption Measurements of Carbon Monoxide Laser Radiation by Water Vapor," presented at Autumn Meeting of Optical Society Association, 17-20 October 1972, San Francisco, California.

4. D. K. Rice, "Absorption Measurements of Carbon Monoxide Laser Radiation by Water Vapor," Appl. Opt., Vol. 12, No. 2, pp 218-225, (February 1973).

5. R. K. Long, "Water Vapor Absorption Measurements Using a Single Frequency CO Laser," presented at Autumn Meeting of Optical Society Association, 17-20 October 1972, San Francisco, California.

6. "Semiannual Technical Summary, ARPA/STO Program (U)," Lincoln Laboratory, MIT, Lexington, Mass., AD 517-645L (Secret/FRD) (20 June 1971).

7. R. A. McClatchey, AFCRL Optics Physics Laboratory, Bedford, Mass., Private Communication.

8. S. L. Valley (ed.), Handbook of Geophysics and Space Environments, p. 2.10, AFCRL, Office of Aerospace Research (1965).

9. J. H. McCoy, D. B. Rensch, and R. K. Long, "Water Vapor Continuum Absorption of Carbon Dioxide Laser Radiation Near 10μ," Appl. Opt., Vol. 8, No. 7, pp 1471-1478 (July 1969).

10. P. K. L. Yin and R. K. Long, "Atmospheric Absorption at the Line Center of P(20) CO_2 Laser Radiation," Appl. Opt., Vol. 7, No. 8, pp 1551-1553 (August 1968).

11. R. A. McClatchey, R. W. Fenn, J. E. A. Selby, F. E. Volz, and J. S. Garing, "Optical Properties of the Atmosphere (Revised)," AD 726 116 (10 May 1971).

12. S. Edelberg, L. C. Bradley, and J. Herrman, "Nonlinear Laser Propagation - A Review," Proceedings Fifth Conference on Laser Technology, Vol. I, 25-27, April 1972, p. 715.

13. S. Edelberg, "Theoretical Calculations of Thermal Blooming for Different Lasers," (private communication to G. Hasserjian, 12 January 1973).

14. A. D. Varvatsis and M. I. Sancer, "Expansion of a Focused Laser Beam in the Turbulent Atmosphere," Northrop Corporate Laboratories, Report No. 70-36R, May 1970.

15. D. A. de Wolf, "Effects of Turbulence Instabilities on Laser Propagation," RCA Laboratories, RADC-TR-71-249, October 1971.

16. A. E. Siegman and H. Y. Miller, "Unstable Optical Resonator Loss Calculations Using the Prony Method," Appl. Opt. 9, 2729 (1970).

17. M. Born and E. Wolf, Principles of Optics, (Permagon Press, Inc., Oxford, 1965), p. 452.

DOCUMENT CONTROL DATA - R & D

(Security classification of title, body of abstract and indexing annotation must be entered when the overall report is classified)

1. ORIGINATING ACTIVITY (Corporate author)	2a. REPORT SECURITY CLASSIFICATION
Northrop Corporation, Northrop Research and Technology Center, Laser Technology Laboratories	SECRET - NO FORN
	2b. GROUP

3. REPORT TITLE

Semiannual Technical Report, High Power CO Laser (U)

4. DESCRIPTIVE NOTES *(Type of report and inclusive dates)*

Semiannual Technical Report, September 1972 through February 1973

5. AUTHOR(S) *(First name, middle initial, last name)*

Laser Technology Laboratories

6. REPORT DATE	7a. TOTAL NO. OF PAGES	7b. NO. OF REFS
March 1973	56	17

8a. CONTRACT OR GRANT NO.	9a. ORIGINATOR'S REPORT NUMBER(S)
N00014-72-C-0043	
b. PROJECT NO.	NRTC 73-10R
c.	9b. OTHER REPORT NO(S) *(Any other numbers that may be assigned this report)*
d.	None

10. DISTRIBUTION STATEMENT In addition to security requirements which must be met, this document is subject to special export controls and each transmittal to foreign governments or foreign nationals may be made only with prior approval of Office of Naval Research (Code 421), Arlington, Virginia 22217

11. SUPPLEMENTARY NOTES	12. SPONSORING MILITARY ACTIVITY
None	Advanced Research Projects Agency, Arpa Order No. 1807

13. ABSTRACT

(U) Effort on the High Power CO Laser Program is reviewed. The program is directed toward the development of the required CO laser technology, the required component technology, and the design and construction of intermediate power laser devices. The results of analytical and experimental investigation of the basic characteristics of the laser and data from a high pressure electrically excited CO laser device are discussed.

DD FORM 1473 (1 NOV 65)

14. KEY WORDS	LINK A		LINK B		LINK C	
	ROLE	WT	ROLE	WT	ROLE	WT
CO Laser						
Molecular Lasers						
Electrical Discharge Lasers						
High Power Lasers						

END-5- 73

From: Chief of Naval Research
To: Administrator
     Defense Technical Information Center
     ATTN: William Bush, DTIC-OCQ
     8725 John J. Kingman Road Suite 0944
     Ft. Belvoir, VA 22060-6218

Subj: CHANGE OF DISTRIBUTION STATEMENT

1. Permission is granted to change the distribution statement for the following documents to Distribution Statement A: Approved for Public Release; Distribution is Unlimited:

     AD 525 354
     AD 529 106
     AD 922 294

2. Questions may be directed to the undersigned on (703) 696-4619.

PEGGY LAMBERT
By direction